NUCLEAR MAGNETIC RESONANCE SPECTROSCOPY OF SILICON NANOPARTICLES

by

Brayden Glockzin

A thesis submitted in partial fulfillment of the requirements for the degree of

Master of Science

Department of Chemistry
University of Alberta

Abstract

Despite the widespread use of hydrofluoric acid (HF) in the preparation of silicon surfaces, the true nature of fluorinated surface species remains unclear. Here, an array of characterization techniques led by solid-state nuclear magnetic resonance spectroscopy is employed to uncover the nature of fluorinated moieties on the surface of hydride-terminated silicon nanoparticles. A structural model that explains the observed trends in ^{19}F and ^{29}Si magnetic shielding is proposed and further supported by quantum chemical computations. Fluorine is incorporated into local oxidation domains on the surface and clustered at the interface of the oxide and surrounding hydride-terminated surface. Silicon sites capped by a single fluorine are also identified by their distinct ^{19}F and ^{29}Si chemical shifts, providing insight into how fluorine termination influences the electronic structure. Finally, challenges associated with Teflon® contamination are highlighted that future explorations of nanomaterials may have to contend with.

Preface

The work in this thesis is an original contribution by Brayden Glockzin. As the lead investigator, I collected the majority of experimental and theoretical data presented herein. Shihong Xu (University of Alberta Nanofab) and Chuyi Ni performed X-ray photoelectron spectroscopy and energy-dispersive X-ray spectroscopy, respectively. The sample of functionalized silicon nanoparticles in this thesis was prepared by Kevin O’Connor who also collected the transmission electron microscopy images of these particles. Profs. V.K. Michaelis and J.G.C. Veinot were the supervisory authors and provided me with guidance for experimentation and writing. Parts of this thesis will be published in the coming months.

“He must increase, but I must decrease.” (John 3:30 ESV)

Acknowledgments

First, I would like to express my gratitude to Professors Vladimir K. Michaelis and Jonathan G.C. Veinot. Their guidance has been pivotal for my development as a scientist, and I am very grateful for how they have advocated for me during my time at the University of Alberta.

I also extend thanks to many current and former members of the Michaelis and Veinot groups. From the Michaelis lab, I thank Abhoy Karmakar, Riley Hooper, Diganta Sarkar, Arkadii Pominov, Madhu Chaudhary, and Brittney Klein for their mentorship and assistance. My master's also would not have been possible without Dr. Guy Bernard, who was always willing to help and told me many entertaining stories. From the Veinot lab, I extend special thanks to I Teng (Emily) Cheong, Kevin O'Connor, Cole Butler, Madison Chevalier, and Chuyi (Martin) Ni.

I also thank my third committee member Prof. Mariusz Klobukowski for his introduction to computational chemistry in CHEM 593 and helpful direction during my research. I am also very grateful for Leah Veinot and Sergei Vagin, who worked extremely hard to organize the ATUMS meetings.

Finally, my gratitude is extended to my family and friends for their unconditional love and support. I am very blessed to have so many amazing people in my life.

Table of Contents

Chapter 1. Introduction 1

1.1 Nuclear Magnetic Resonance Spectroscopy 1

1.2 Quantum Mechanics of NMR Spectroscopy 1

1.2.1 The Time-Dependent Schrödinger Equation 1

1.2.2 The NMR Spin Hamiltonian 2

1.2.3 The Zeeman Interaction and Larmor Precession 3

1.2.4 Magnetic Shielding 7

1.2.5 Spin-Spin Coupling 10

1.3 Theoretical Computations of NMR Parameters 11

1.4 NMR Spectroscopy of Silicon Nanoparticles 12

1.4.1 Cross-Polarization 12

1.4.2 Quantum Confinement and Chemical Shift Trends 13

Chapter 2. Unmasking Fluorinated Moieties on the Surface of Hydride-Terminated Silicon Nanoparticles Using Solid-state NMR Spectroscopy 15

2.1 Introduction 15

2.2 Results 18

2.2.1 The Structure and Elemental Composition of H-SiNPs 18

2.2.2 Solid-state ^{29}Si NMR of HF-Etched SiNPs 21

2.2.3 Solid-state ^{19}F NMR of HF-Etched SiNPs 24

2.3 Discussion 28

2.3.1 Electronic Effects of Fluorine Termination 28

2.3.2 Challenges With Fluorine Surface Chemistry 33

2.4 Conclusions 36

2.5 Materials & Methods 37
2.5.1 Starting Materials 37
2.5.2 Synthesis of Hydrogen Silsesquioxane (HSQ) 37
2.5.3 Preparation of 6 and 21 nm H-SiNPs 38
2.5.4 Air-Sensitive X-ray Photoelectron Spectroscopy (XPS) 39
2.5.5 Transmission Electron Microscopy (TEM) 39
2.5.6 Energy Dispersive X-ray Spectroscopy (EDX) 39
2.5.7 Powder X-ray Diffraction (XRD) 39
2.5.8 Fourier Transformed Infrared Spectroscopy (FTIR) 40
2.5.9 Solid-state Nuclear Magnetic Resonance (NMR) Spectroscopy 40
2.5.10 Quantum Chemical Computations 41
Chapter 3. Future Work 43
3.1 Heteronuclear Correlation (HETCOR) Spectroscopy and ^{19}F-Detected Methods 43
3.2 SiNPs as Multimodal Medical Imaging Agents 43
References 45
Appendix A: Supplementary Data for Chapter 2 59

List of Tables

Table 1.1. Properties of NMR-Active Nuclei in Hydride-Terminated Silicon Nanoparticles.[36] .. 12

Table 2.1. Comparison of the ^{29}Si Chemical Shifts of Groups Observed in Fluorine-Doped and Fluorinated Silicas to the DFT-Computed Chemical Shifts for Analogous Groups. 23

Table 2.2. Comparison of the ^{19}F Chemical Shifts of Groups Observed in Fluorine-Doped and Fluorinated Silicas to the DFT-Computed Chemical Shifts for Analogous Groups. 27

Table 2.3. ^{29}Si Magnetic Shielding Tensors for Si_3SiH and Si_3SiF Groups in Models With C_{3v} Symmetry. 30

List of Figures

Figure 1.1 Zeeman splitting of the nuclear spin state energies (E) in the presence of an external magnetic field (B_0) for a nucleus with I = ½ and a positive γ. 4

Figure 1.2. Vector representation of the states (a) α and (b) $+x$. (c) Precession about the z-axis of a nuclear spin with a positive γ 5

Figure 1.3. Simulated solid-state ^{19}F NMR spectra (I = ½) under non-spinning conditions at a magnetic field strength of 9.39 T ($\omega 19F/2\pi = 376.498$ MHz) with $\Omega = 50$ ppm and $\kappa = -1, 0, 1$. Note that the principal axes of the chemical shift tensor coincide with the principal axes of the shielding tensor (e.g., δ_{11} coincides with σ_{11}). 9

Figure 1.4. Cross-polarization pulse sequence with ^{1}H and ^{29}Si as the example nuclei. 13

Figure 2.1. (a) IR spectra of 6 nm H-SiNPs collected before and after NMR analysis (post seven months). (b) Graded structure of H-SiNPs comprising a disordered surface (SiH_x species), quasi-ordered subsurface, and a crystalline core. (c) Comparison of the calculated ^{29}Si chemical shifts for the hydride-terminated models to the experimental ^{29}Si MAS and ^{29}Si{^{1}H} CPMAS NMR spectra of 6 nm H-SiNPs ($\nu rot = 10$ kHz). In (b) the orientation of the Si_3SiH groups reflects that of the specified crystal face. The colored atoms in (c) are those for which the chemical shifts are plotted. 19

Figure 2.2. (a) ^{29}Si{^{19}F} CPMAS NMR spectra of 6 nm H-SiNPs showing five distinct sites labelled i-v ($\nu rot = 10$ kHz). (b) Comparison of the calculated ^{29}Si chemical shifts to an experimental ^{29}Si{^{19}F} (top trace) and ^{29}Si{^{1}H} CPMAS (bottom trace) spectra. The theoretical ^{29}Si chemical shifts are separated into models containing groups with both oxygen and fluorine (O/F)−Si(111) or fluorine alone (F)−Si(111). (c) Examples of (O/F)−Si groups. 22

Figure 2.3. (a) Enlarged view of ^{19}F MAS NMR spectra of 21 nm and 6 nm H-SiNPs ($\nu rot = 20$ kHz). (b) Comparison of the calculated ^{19}F chemical shifts to the experimental ^{19}F MAS spectra of 6 nm H-SiNPs. Asterisks (*) indicate spinning sidebands and the tilde (~) in (b) indicates that the peak corresponding to $[SiF_6]^{2-}$ has been truncated. 26

Figure 2.4. (a) Paramagnetic shielding contribution to Si_3SiH arising from HOMO-1↔LUMO mixing. (b) Paramagnetic shielding contribution to Si_3SiF arising from HOMO↔LUMO mixing. The spacing between MOs in both panels is not an exact representation of the energy difference between MOs. 32

Figure 2.5. (a) ^{19}F MAS NMR spectra of Teflon (green) and 6 nm H-SiNPs prepared using a Teflon (black) or Pyrex (grey) stir bar (νrot = 18-20 kHz). (b) Variation of ^{19}F spectra including the disappearance of the peak at −161 ppm (νrot = 10 kHz). The tilde (~) in panel (a) indicates that the upper half of the peak corresponding to $[SiF_6]^{2-}$ has been truncated. 35

List of Schemes

Scheme 2.1. (a) Proposed mechanism for the etching of SiO_2 in aqueous HF-based solutions. (b) Formation of a terminal Si−F group. (c) Mechanism of hydride termination of the underlying silicon substrate. Figure adapted from refs. 78 and 80. 16

List of symbols

B_0	Applied magnetic field
k_B	Boltzmann constant
γ	Gyromagnetic ratio
σ_{iso}	Isotropic magnetic shielding
σ_{ij}	Element of the shielding tensor
δ_{iso}	Isotropic chemical shift
Ω	Span of the chemical shift anisotropy
κ	Skew of the chemical shift anisotropy
ψ	Wavefunction
μ	Nuclear magnetic moment
μ_0	Permeability constant
ω_L	Larmor frequency (rad/s)
h	Planck's constant
$\hbar$	Reduced Planck's constant
I	Nuclear spin quantum number
E	Energy
T	Temperature
R_{DD}	Dipolar coupling constant
ADF	Amsterdam Density Functional
BO	Born-Oppenheimer
CSA	Chemical shift anisotropy

CPMAS	Cross-polarization magic angle spinning
DFT	Density functional theory
EDX	Energy dispersive X-ray spectroscopy
FID	Free induction decay
FT	Fourier transform
GIAOs	Gauge-including atomic orbitals
HETCOR	Heteronuclear correlation spectroscopy
HF	Hydrofluoric acid
HFX	Hartree-Fock exchange
H-SiNPs	Hydride-terminated silicon nanoparticles
HSQ	Hydrogen silsesquioxane
HOMO	Highest occupied molecular orbital
IR	Infrared
LUMO	Lowest unoccupied molecular orbital
MAS	Magic angle spinning
MS	Magnetic shielding
MRI	Magnetic resonance imaging
NMR	Nuclear magnetic resonance
PAS	Principal axis system
QC	Quantum confinement
SiNPs	Silicon nanoparticles
SOC	Spin-orbit coupling

TEM	Transmission electron microscopy
TPPM	Two-pulse phase-modulated
TZP	Triple-zeta with a polarization function
TZ2P	Triple-zeta with two polarization functions
XPS	X-ray photoelectron spectroscopy
XRD	X-ray diffraction

Chapter 1. Introduction

1.1 Nuclear Magnetic Resonance Spectroscopy

The 1944 Nobel Prize in Physics was awarded to Isidor Rabi for his measurement and description of the Nuclear Magnetic Resonance (NMR) phenomenon.[1] Since then, NMR has been exploited for technologies including pulsed NMR spectroscopy and magnetic resonance imaging (MRI), which won the 2003 Nobel Prize in Physiology. Healthcare has been pushed to new frontiers because MRI non-invasively probes injury and disease. Similarly, NMR spectroscopy provides insight into the atomic-level structure of chemical systems that is inaccessible with other characterization techniques.[2] With this, it is now fitting to explore the theoretical foundation of NMR.

1.2 Quantum Mechanics of NMR Spectroscopy

There are many useful analogies from classical physics that provide a straightforward understanding of the principles of NMR; these analogies are ineffective once more advanced concepts like superposition are introduced. This chapter will provide a proper quantum mechanical description of NMR spectroscopy.

Nuclei possess intrinsic angular momentum known as spin. When the spin quantum number I of a nucleus is greater than zero, it also has a magnetic moment that is proportional to the spin angular momentum:[3,4]

$$\hat{\boldsymbol{\mu}} = \gamma \hbar \hat{\boldsymbol{I}} \tag{1.1}$$

In Equation 1.1, $\hat{\boldsymbol{I}}$ and $\hat{\boldsymbol{\mu}}$ and are the nuclear spin angular momentum and magnetic moment operators, respectively, γ is the gyromagnetic ratio of the nucleus of interest, and $\hbar$ is the reduced Planck's constant. (Note: vectors and matrices are denoted in boldface). The proportionality between spin and magnetic moment will appear in many subsequent expressions.

1.2.1 The Time-Dependent Schrödinger Equation

A quantum mechanical description of NMR begins with the time-dependent Schrödinger equation.

$$i\hbar \frac{\partial \psi(t)}{\partial t} = \hat{H} \psi(t) \tag{1.2}$$

The general solution to Equation 1.2 in the case of a time-independent Hamiltonian is

$$\psi(t) = \exp\left(-i\hbar^{-1} \hat{H} t\right) \psi(0) \tag{1.3}$$

where the exponential term is called the *propagator*.[4] The solution in Dirac notation is

$$|\psi(t)\rangle = \exp\left(-i\hbar^{-1}\widehat{\boldsymbol{H}}t\right)|\psi(0)\rangle \tag{1.4}$$

where $\widehat{\boldsymbol{H}}$ is the matrix representation of the Hamiltonian and $|\psi(0)\rangle$ and $|\psi(t)\rangle$ are vectors.

1.2.2 The NMR Spin Hamiltonian

The Hamiltonians of NMR spectroscopy can be constructed beginning with the Born-Oppenheimer (BO) approximation.[5] The BO approximation assumes that the electrons in molecules are in the ground state for any instantaneous set of nuclear coordinates. For a molecule in the presence of an external magnetic field, the nuclear positions, nuclear magnetic moments ($\boldsymbol{\mu}_k$), and the applied magnetic field ($\boldsymbol{B}_0$) are then external parameters in the BO Hamiltonian.[6] Consider the Taylor expansion of the total molecular energy for a fixed set of nuclear coordinates about the zero-field values of $\boldsymbol{B}_0$ and a classical nuclear magnetic moment $\boldsymbol{\mu}$:[6–13]

$$\begin{aligned} E(\boldsymbol{\mu},\boldsymbol{B}_0) = E^0 + \sum_r \frac{\partial E}{\partial \mu_r}\mu_r + \sum_r \frac{\partial E}{\partial B_{0,r}}B_{0,r} + \frac{1}{2}\sum_{rs}\mu_r \frac{\partial^2 E}{\partial \mu_r\,\partial \mu_s}\mu_s \\ + \frac{1}{2}\sum_{rs} B_{0,r}\frac{\partial^2 E}{\partial B_{0,r}\,\partial B_{0,s}}B_{0,s} + \sum_{rs}\mu_r \frac{\partial^2 E}{\partial \mu_r\,\partial B_{0,s}}B_{0,s} \cdots \end{aligned} \tag{1.5}$$

E^0 is the part of the molecular energy that does not depend on $\boldsymbol{\mu}$ and $\boldsymbol{B}_0$, while $\{\mu_r\}$ and $\{B_r\}$ are cartesian components of $\boldsymbol{\mu}$ and $\boldsymbol{B}_0$, respectively. The energy derivatives in Equation 1.5 are related to several molecular properties including magnetic shielding and spin-spin coupling which will be discussed in ***Sections 1.2.4*** and ***1.2.5***. It is the terms in Equation 1.5 involving the interaction of spins with the magnetic field and between themselves (if it is extended to include multiple spins) that are of interest. The energy operator corresponding to these terms is the NMR spin Hamiltonian ($\widehat{H}_{NMR}$). Since $\widehat{\boldsymbol{\mu}}_k = \gamma_k\hbar\widehat{\boldsymbol{I}}_k$, the general form of $\widehat{H}_{NMR}$ for a multi-spin system is[4]

$$\widehat{H}_{NMR} = \hbar\sum_k \gamma_k\widehat{\boldsymbol{I}}_k\cdot\boldsymbol{Z}_k\cdot\boldsymbol{B}_0 + \hbar^2\sum_{k>l}\gamma_k\gamma_l\widehat{\boldsymbol{I}}_k\cdot\boldsymbol{A}_{kl}\cdot\widehat{\boldsymbol{I}}_l + \frac{\hbar^2}{2}\sum_k \gamma_k^2\widehat{\boldsymbol{I}}_k\cdot\boldsymbol{Q}_k\cdot\widehat{\boldsymbol{I}}_k \tag{1.6}$$

where $\boldsymbol{Z}_k$, $\boldsymbol{A}_{kl}$, and $\boldsymbol{Q}_k$ are 3×3 matrices involving the derivatives of the molecular energy from Equation 1.5. Note that the electronic structure does not explicitly appear in $\widehat{H}_{NMR}$; its effects are implicit in the derivatives. The tensor elements can be obtained with the Hellman-Feynman theorem: For a Hamiltonian that depends continuously on real variables α and β,[4,14]

$$\frac{\partial E_0}{\partial \alpha} = \frac{\partial}{\partial \alpha}\langle\psi_0|\widehat{H}|\psi_0\rangle = \left\langle\psi_0\middle|\frac{\partial \widehat{H}}{\partial \alpha}\middle|\psi_0\right\rangle \tag{1.7}$$

$$\frac{\partial^2 E_0}{\partial\alpha\,\partial\beta} = \left\langle\psi_0\left|\frac{\partial^2\hat{H}}{\partial\alpha\,\partial\beta}\right|\psi_0\right\rangle + \sum_{n\neq 0}\frac{\left\langle\psi_0\left|\frac{\partial\hat{H}}{\partial\beta}\right|\psi_n\right\rangle\left\langle\psi_n\left|\frac{\partial\hat{H}}{\partial\alpha}\right|\psi_0\right\rangle + \left\langle\psi_0\left|\frac{\partial\hat{H}}{\partial\alpha}\right|\psi_n\right\rangle\left\langle\psi_n\left|\frac{\partial\hat{H}}{\partial\beta}\right|\psi_0\right\rangle}{E_0 - E_n} \tag{1.8}$$

where α and β could be components of a classical (i.e., continuous) nuclear magnetic moment(s) or $\boldsymbol{B}_0$. Equation 1.6 shows that spin interactions may be linear, bilinear, or quadratic in spin operators.[4] Interactions that are quadratic in spin operators, such as the nuclear quadrupolar interaction, will not be covered in this chapter.

1.2.3 The Zeeman Interaction and Larmor Precession

The classical interaction energy of a magnetic moment with an external magnetic field is:

$$E = -\boldsymbol{\mu}\cdot\boldsymbol{B}_0 \tag{1.9}$$

Substituting $\hat{\boldsymbol{\mu}} = \gamma\hbar\hat{\boldsymbol{I}}$,

$$\hat{H}_Z = -\gamma\hbar\begin{pmatrix}\hat{I}_x & \hat{I}_y & \hat{I}_z\end{pmatrix}\cdot\begin{pmatrix}B_{0,x}\\ B_{0,y}\\ B_{0,z}\end{pmatrix} = -\gamma\hbar\begin{pmatrix}\hat{I}_x & \hat{I}_y & \hat{I}_z\end{pmatrix}\cdot\begin{pmatrix}1 & 0 & 0\\ 0 & 1 & 0\\ 0 & 0 & 1\end{pmatrix}\cdot\begin{pmatrix}B_{0,x}\\ B_{0,y}\\ B_{0,z}\end{pmatrix} \tag{1.10}$$

gives an expression that has the form of the first term on the right-hand side of Equation 1.6. For a multi-spin system, Equation 1.10 would contain a sum over all spins. If the magnetic field is applied along the z-axis of the lab frame, then Equation 1.10 reduces to

$$\hat{H}_Z = -\hbar\gamma B_{0,z}\hat{I}_z = \hbar\omega_L\hat{I}_z \tag{1.11}$$

where $\omega_L = -\gamma B_{0,z}$ (Larmor frequency). Equation 1.11 shows that the Zeeman Hamiltonian shares the same eigenfunctions as $\hat{I}_z$. For a nucleus with $I = ½$, there are $2(½)+1 = 2$ sublevels that are degenerate in the absence of an external magnetic field. These states are denoted as $|\alpha\rangle$ and $|\beta\rangle$ or colloquially as “spin up” and “spin down.” The degeneracy is lifted when an external magnetic field is applied:

$$\hat{H}_Z|\alpha\rangle = -\hbar\gamma B_{0,z}\hat{\boldsymbol{I}}_z|\alpha\rangle = -\frac{1}{2}\gamma\hbar B_{0,z}|\alpha\rangle, \qquad |\alpha\rangle = \begin{pmatrix}1\\0\end{pmatrix} \tag{1.12}$$

$$\hat{H}_Z|\beta\rangle = -\hbar\gamma B_{0,z}\hat{\boldsymbol{I}}_z|\beta\rangle = \frac{1}{2}\gamma\hbar B_{0,z}|\beta\rangle, \qquad |\beta\rangle = \begin{pmatrix}0\\1\end{pmatrix} \tag{1.13}$$

The negative eigenvalue in Equation 1.12 indicates that $|\alpha\rangle$ is lower in energy than $|\beta\rangle$ if γ is positive. Taking the energy difference

$$\Delta E = \frac{1}{2}\hbar\gamma B_{0,z} - \left(-\frac{1}{2}\hbar\gamma B_{0,z}\right) = \hbar\gamma B_{0,z} \tag{1.14}$$

shows that the splitting is proportional to the strength of the applied magnetic field (**Figure 1.1**).

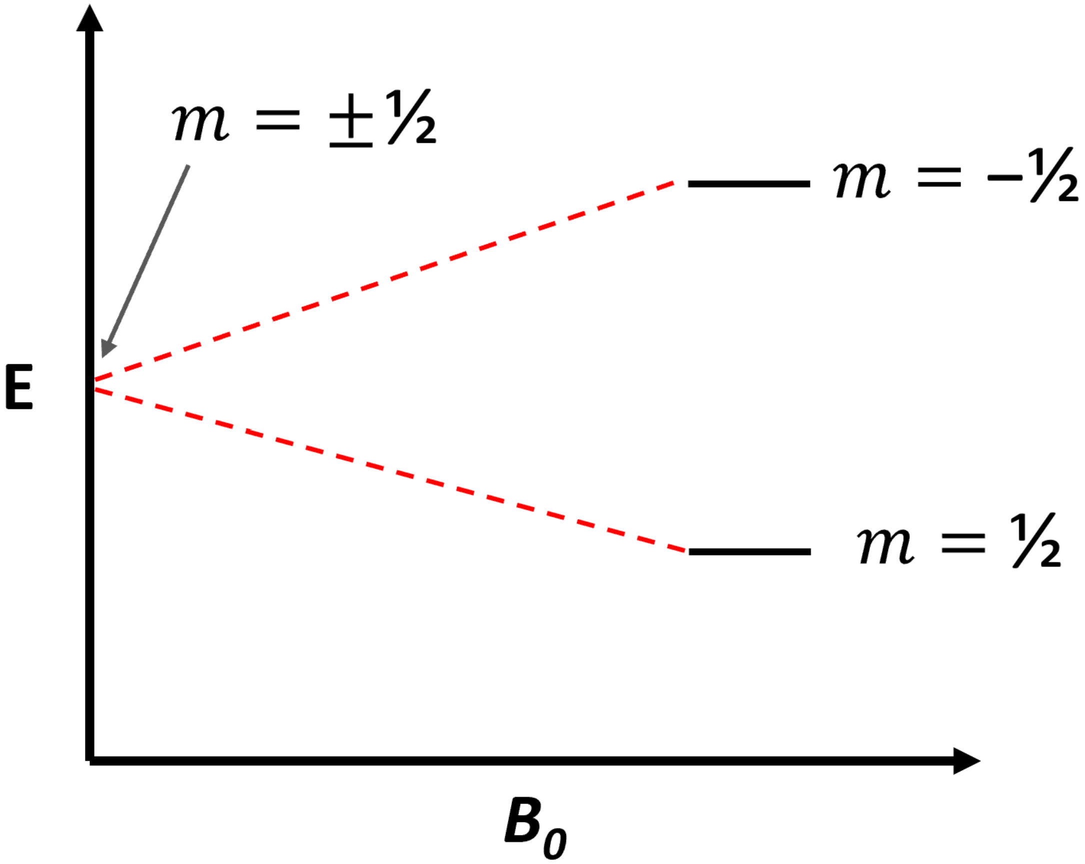

Figure 1.1 Zeeman splitting of the nuclear spin state energies (E) in the presence of an external magnetic field (B_0) for a nucleus with $I = ½$ and a positive γ.

The Zeeman interaction leads to Larmor precession, which is the phenomenon that underpins magnetic resonance. However, Larmor precession only occurs for spins in superpositions. This is evident from inserting the Zeeman Hamiltonian into the solution to the Schrödinger equation (Equation 1.4). For an isolated spin ½ nucleus, the solution is,

$$|\psi(t)\rangle = \exp\left(-i\omega_L \hat{\boldsymbol{I}}_z t\right)|\psi(0)\rangle, \qquad \hat{\boldsymbol{I}}_z = \begin{pmatrix} 1/2 & 0 \\ 0 & -1/2 \end{pmatrix} \tag{1.15}$$

where the Hamiltonian has been expressed in natural units ($\widehat{\boldsymbol{\mathcal{H}}} = \hbar^{-1}\widehat{\boldsymbol{H}}$). Equation 1.15 is rewritten using the Taylor expansion of the operator exponential:[3,4]

$$|\psi(t)\rangle = \left[\sum_{n=0}^{\infty} \frac{(-i\omega_L t)^n}{n!} \begin{pmatrix} (1/2)^n & 0 \\ 0 & (-1/2)^n \end{pmatrix}\right]|\psi(0)\rangle = \begin{pmatrix} e^{-i\omega_L t/2} & 0 \\ 0 & e^{i\omega_L t/2} \end{pmatrix}|\psi(0)\rangle \tag{1.16}$$

If $|\psi(0)\rangle = |\alpha\rangle$, corresponding to the spin-polarized along the z-axis (**Figure 1.2**a), the expectation values of the angular momentum are[4]

$$\begin{aligned} \langle\psi(t)|\hat{\boldsymbol{I}}_x|\psi(t)\rangle &= 0 \\ \langle\psi(t)|\hat{\boldsymbol{I}}_y|\psi(t)\rangle &= 0 \\ \langle\psi(t)|\hat{\boldsymbol{I}}_z|\psi(t)\rangle &= 1/2 \end{aligned} \tag{1.17}$$

which are constant in time if the Hamiltonian is unchanged ($|\alpha\rangle$ and $|\beta\rangle$ are stationary states). If the spin is initially in a superposition such as,

$$|\psi(0)\rangle = \frac{1}{\sqrt{2}}(|\alpha\rangle + |\beta\rangle) = \frac{1}{\sqrt{2}}\begin{pmatrix}1\\1\end{pmatrix} = |{+x}\rangle \tag{1.18}$$

corresponding to polarization along the x-axis (**Figure 1.2**b), then the expectation values are:[4]

$$\begin{aligned} \langle\psi(t)|\hat{\boldsymbol{I}}_x|\psi(t)\rangle &= \frac{1}{2}\cos(\omega_L t) \\ \langle\psi(t)|\hat{\boldsymbol{I}}_y|\psi(t)\rangle &= -\frac{1}{2}\sin(\omega_L t) \\ \langle\psi(t)|\hat{\boldsymbol{I}}_z|\psi(t)\rangle &= 0 \end{aligned} \tag{1.19}$$

This shows that the spin undergoes precession about the z-axis of the lab frame at the Larmor frequency if it is in a superposition at $t = 0$. This may be interpreted as in **Figure 1.2**c. (Note the negative sense of the precession in **Figure 1.2**c which is the case for spins with a positive γ).

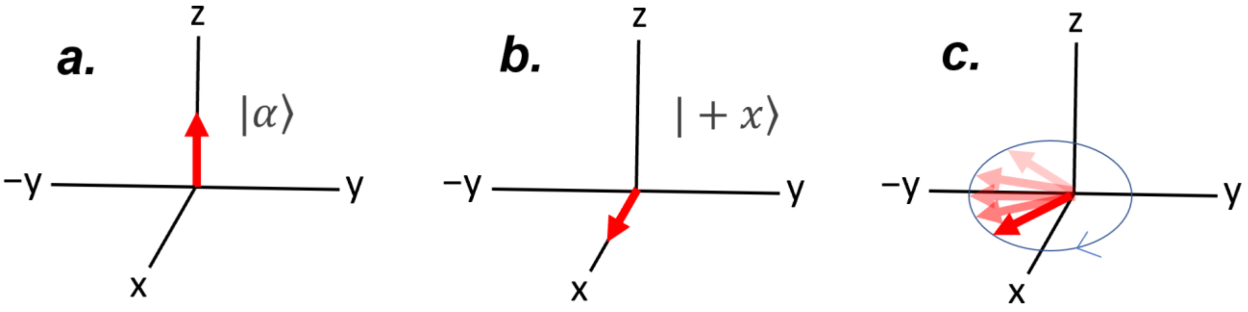

Figure 1.2. Vector representation of the states (a) $|\alpha\rangle$ and (b) $|+x\rangle$. (c) Precession about the z-axis of a nuclear spin with a positive γ.

The precession of nuclear spins induces an oscillating current in the receiver coil of an NMR probe. This is a time domain signal that is Fourier transformed to give an NMR spectrum in the frequency domain. For a real sample containing many nuclear spins (e.g., 10^{22}), virtually all spins are in a superposition and undergo precession.[3] However, their polarization vectors are uniformly distributed so there is no net transverse polarization at thermal equilibrium. There is, however, longitudinal polarization.[3] Polarization is best explained by introducing the *density operator* or *density matrix*. The density operator for a single spin with wavefunction $|\psi\rangle$ is:[3,4]

$$\hat{\boldsymbol{\rho}} = |\psi\rangle\langle\psi| \tag{1.20}$$

The diagonal elements of the density matrix are,

$$\langle n|\hat{\boldsymbol{\rho}}|n\rangle = c_n c_n^* = p_n \tag{1.21}$$

which corresponds to the probability of finding the spin in the state $|n\rangle$. For a spin ½ nucleus, $|n\rangle$ would correspond to $|\alpha\rangle$ or $|\beta\rangle$. Therefore, the diagonal elements of the density matrix are known as *populations*.[4,15,16] If there is a difference in the probabilities of finding a spin in $|\alpha\rangle$ or $|\beta\rangle$, the spin possesses longitudinal polarization. For an ensemble of spins, the populations at thermal equilibrium can be readily calculated. If the energy levels of a spin system are

$$\hat{\boldsymbol{H}}|\psi_n\rangle = E_n|\psi_n\rangle \tag{1.22}$$

the probability of finding a spin in the state $|n\rangle$ is given by a Boltzmann distribution,[3,4]

$$\rho_{nn}^{eq} = \frac{\exp\left(-\frac{E_n}{k_B T}\right)}{\sum_m \exp\left(-\frac{E_m}{k_B T}\right)} \tag{1.23}$$

where k_B is the Boltzmann constant and T is the temperature. For a spin ½ ensemble,

$$\exp\left(-\frac{E_\alpha}{k_B T}\right) = \exp\left(-\frac{\left(-\frac{1}{2}\hbar\gamma B_{0,z}\right)}{k_B T}\right) = \exp\left(\frac{1}{2}\frac{\hbar\gamma B_{0,z}}{k_B T}\right) \tag{1.24}$$

$$\exp\left(-\frac{E_\beta}{k_B T}\right) = \exp\left(-\frac{(\frac{1}{2}\hbar\gamma B_{0,z})}{k_B T}\right) = \exp\left(-\frac{1}{2}\frac{\hbar\gamma B_{0,z}}{k_B T}\right)$$

and the Boltzmann factor $\boldsymbol{\mathcal{B}}$ can be defined:

$$\boldsymbol{\mathcal{B}} = \frac{\hbar\gamma B_{0,z}}{k_B T} \tag{1.25}$$

In the high-temperature approximation, the exponential terms in Equation 1.24 are expanded in a Taylor series in $\boldsymbol{\mathcal{B}}$ and truncated at the first order:[3]

$$\exp\left(\frac{1}{2}\frac{\hbar\gamma B_{0,z}}{k_B T}\right) \approx 1 + \frac{1}{2}\boldsymbol{\mathcal{B}} \tag{1.26}$$

$$\exp\left(-\frac{1}{2}\frac{\hbar\gamma B_{0,z}}{k_B T}\right) \approx 1 - \frac{1}{2}\boldsymbol{\mathcal{B}}$$

The denominator in Equation 1.23 is then

$$\exp\left(\frac{1}{2}\frac{\hbar\gamma B_{0,z}}{k_B T}\right) + \exp\left(-\frac{1}{2}\frac{\hbar\gamma B_{0,z}}{k_B T}\right) \approx 2 \tag{1.27}$$

and the populations are approximately:

$$\begin{aligned} \rho_{\alpha\alpha}^{eq} &\approx \frac{1}{2}\left(1 + \frac{1}{2}\boldsymbol{\mathcal{B}}\right) \\ \rho_{\beta\beta}^{eq} &\approx \frac{1}{2}\left(1 - \frac{1}{2}\boldsymbol{\mathcal{B}}\right) \\ \rho_{\alpha\alpha}^{eq} - \rho_{\beta\beta}^{eq} &\approx \frac{1}{2}\frac{\hbar\gamma B_{0,z}}{k_B T} \end{aligned} \tag{1.28}$$

Thus, at room temperature, there is virtually no difference between the equilibrium populations. For example, the difference in the probability of finding a spin in $|\alpha\rangle$ or $|\beta\rangle$ for an ensemble of ^{19}F nuclei ($\gamma = 25.18148 \times 10^7\ rad\ T^{-1}\ s^{-1}$) at 9.39 T and 298 K is about 3.03×10^{-5}.

The off-diagonal elements of the density matrix are known as *coherences*. For a single spin, coherence indicates a superposition in the wavefunction (transverse polarization).[3,4,15,16]

$$\langle n|\widehat{\boldsymbol{\rho}}|k\rangle = c_n c_k^* \tag{1.29}$$

Since there is no net polarization in the transverse plane for an ensemble of spins at thermal equilibrium, the off-diagonal elements of the density matrix for the whole spin system are zero. However, a pulse converts the population difference into coherences. Since the population difference is so small at room temperature, the coherences generated by a pulse (i.e., transverse polarization) are also small which is why NMR is insensitive.

1.2.4 Magnetic Shielding

Electrons in molecules interact with the applied magnetic field to produce an induced magnetic field. The effective field ($\boldsymbol{B}$) experienced by a nucleus is[17,18]

$$\boldsymbol{B} = \boldsymbol{B}_0 - \boldsymbol{\sigma}\boldsymbol{B}_0 \tag{1.30}$$

where $\boldsymbol{\sigma}$ is a 3×3 matrix known as the magnetic shielding tensor. The classical interaction energy is then

$$E = -\boldsymbol{\mu} \cdot (\mathbf{1} - \boldsymbol{\sigma})\boldsymbol{B}_0 = (-\boldsymbol{\mu} \cdot \boldsymbol{B}_0) + (\boldsymbol{\mu} \cdot \boldsymbol{\sigma} \cdot \boldsymbol{B}_0) \tag{1.31}$$

which is the sum of the energy arising from the Zeeman and the magnetic shielding interactions. Substituting the magnetic moment operators into the last term of the right-hand side of Equation 1.31 gives the magnetic shielding (MS) Hamiltonian.

$$\hat{H}_{MS} = \gamma\hbar\begin{pmatrix}\hat{I}_x & \hat{I}_y & \hat{I}_z\end{pmatrix}\cdot\begin{pmatrix}\sigma_{xx} & \sigma_{xy} & \sigma_{xz}\\ \sigma_{yx} & \sigma_{yy} & \sigma_{yz}\\ \sigma_{zx} & \sigma_{zy} & \sigma_{zz}\end{pmatrix}\cdot\begin{pmatrix}B_x\\ B_y\\ B_z\end{pmatrix} \tag{1.32}$$

From Equation 1.5, the shielding tensor is,[9,10,19]

$$\boldsymbol{\sigma} = \left.\frac{\partial^2 E}{\partial\boldsymbol{\mu}\,\partial\boldsymbol{B}_0}\right|_{\boldsymbol{\mu}=0,\boldsymbol{B}_0=0} \tag{1.33}$$

which is typically decomposed into diamagnetic ($\boldsymbol{\sigma}^d$) and paramagnetic ($\boldsymbol{\sigma}^p$) terms.[20] The general form of the expressions for the elements for $\boldsymbol{\sigma}^d$ and $\boldsymbol{\sigma}^p$ are identified with the first and second terms on the right-hand side of Equation 1.8, respectively.[4,10] For the paramagnetic term, the matrix elements in the numerator are three-center integrals that can be subject to group theory analysis as is common in spectroscopy.[21] This will be important in **Chapter 2**. For systems containing heavy atoms, spin-orbit effects can also make sizeable contributions.[8,22–24]

Some properties of the shielding tensor are directly observed in the powder patterns of solid-state NMR spectroscopy. In the principal axis system (PAS), the symmetric part of the shielding tensor is diagonal.[17]

$$\boldsymbol{\sigma}^{PAS} = \begin{pmatrix}\sigma_{11} & 0 & 0\\ 0 & \sigma_{22} & 0\\ 0 & 0 & \sigma_{33}\end{pmatrix} \tag{1.34}$$

The magnitudes of the principal components are:

$$\sigma_{11} \leq \sigma_{22} \leq \sigma_{33} \tag{1.35}$$

The shielding tensor represents the anisotropy of nuclear shielding. In the Herzfeld-Berger (Maryland) convention,[25] the anisotropy is characterized by its breadth (span; Ω) and shape (skew; κ),

$$\Omega = \sigma_{33} - \sigma_{11} \tag{1.36}$$

$$\kappa = \frac{3(\sigma_{iso} - \sigma_{22})}{\Omega} \tag{1.37}$$

where σ_{iso} is the shielding that is independent of the molecular orientation.

$$\sigma_{iso} = \frac{\sigma_{11} + \sigma_{22} + \sigma_{33}}{3} = \frac{1}{3}Tr[\boldsymbol{\sigma}^{PAS}] \tag{1.38}$$

Figure 1.3 shows three simulated powder patterns for ^{19}F.

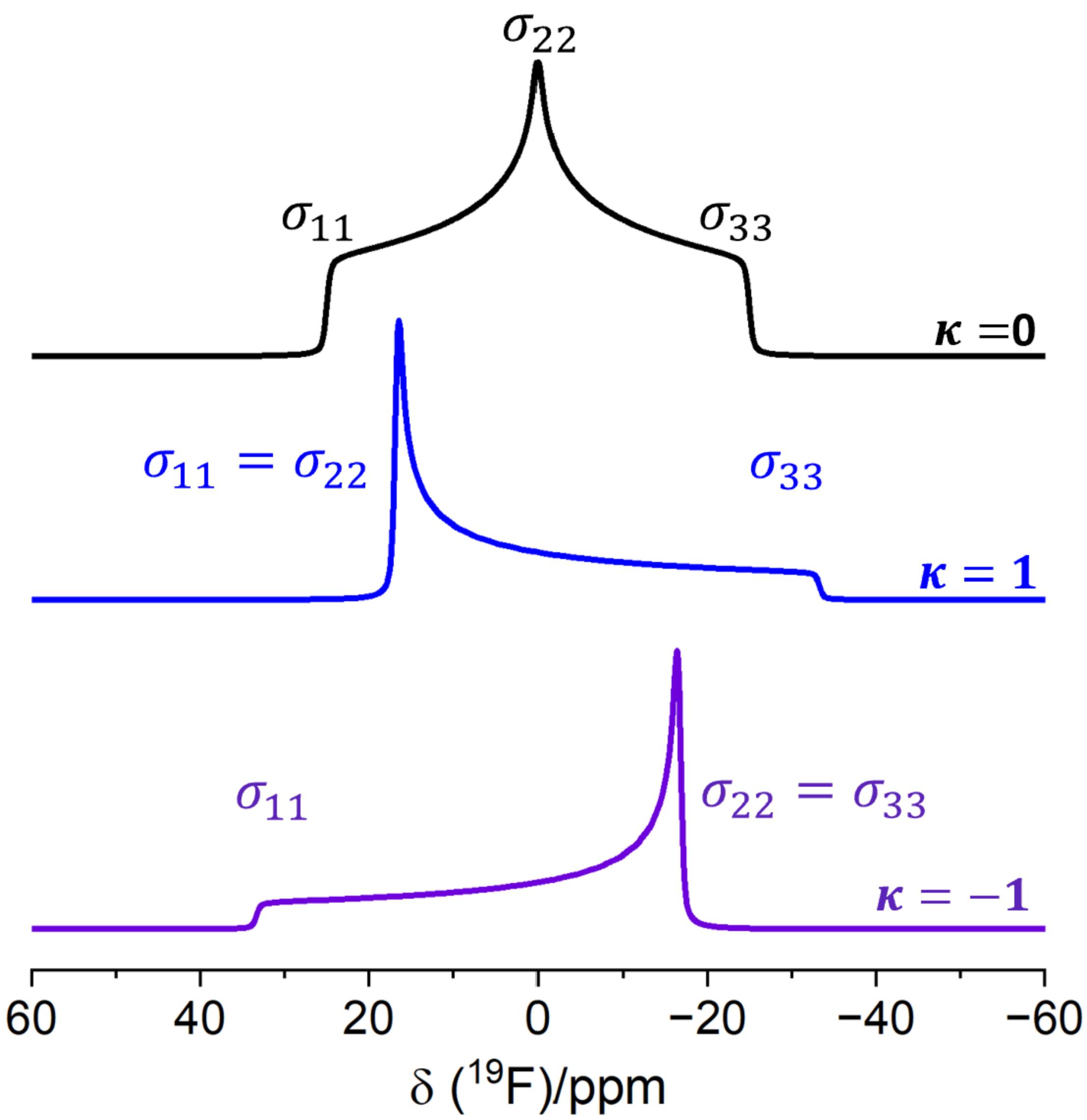

Figure 1.3. Simulated solid-state ^{19}F NMR spectra (I = ½) under non-spinning conditions at a magnetic field strength of 9.39 T ($\omega_{19F}/2\pi$ = 376.498 MHz) with Ω = 50 ppm and $\kappa = -1, 0, 1$. Note that the principal axes of the chemical shift tensor coincide with the principal axes of the shielding tensor (e.g., δ_{11} coincides with σ_{11}).

In practice, it is usually the isotropic *chemical shift* (δ_{iso}) that is measured and not the isotropic *magnetic shielding* (σ_{iso}). The relationship between the two variables is straightforward,

$$\delta_{iso} = \frac{\sigma_{ref} - \sigma_{iso}}{1 - \sigma_{ref}} \cdot 10^6 \tag{1.39}$$

where σ_{ref} is the shielding constant for a reference compound. The numerator in Equation 1.39 is multiplied by 10^6 so that the chemical shift is reported in parts per million (ppm).

1.2.5 Spin-Spin Coupling

From Equation 1.6, the Hamiltonian for the interaction between two spins is

$$\hat{H} = \hbar^2 \gamma_k \gamma_l \hat{\boldsymbol{I}}_k \cdot \boldsymbol{A}_{kl} \cdot \hat{\boldsymbol{I}}_l \tag{1.40}$$

where $\boldsymbol{A}_{kl}$ is the sum of two tensors:

$$\boldsymbol{A}_{kl} = \boldsymbol{K}_{kl} + \boldsymbol{D}_{kl} \tag{1.41}$$

$\boldsymbol{K}_{kl}$ is the *reduced indirect spin-spin coupling tensor* and $\boldsymbol{D}_{kl}$ is the *dipolar coupling tensor*.[4,10,26] The dipolar coupling tensor represents the through-space interaction of two nuclear spins and is obtained without knowledge of the electronic structure. Consider the classical interaction energy between two point magnetic dipoles $\boldsymbol{\mu}_k$ and $\boldsymbol{\mu}_l$ separated by an internuclear distance $\boldsymbol{r}_{kl}$:

$$E = \frac{\mu_0}{4\pi}\left[\frac{\boldsymbol{\mu}_k \cdot \boldsymbol{\mu}_l}{r^3} - \frac{3(\boldsymbol{\mu}_k \cdot \boldsymbol{r}_{kl})(\boldsymbol{\mu}_l \cdot \boldsymbol{r}_{kl})}{r^5}\right] \tag{1.42}$$

Substituting in the magnetic moment operators, expanding the scalar products, and putting the resulting expression in matrix form gives the dipolar Hamiltonian in cartesian coordinates:[4,27,28]

$$\hat{H}_{DD} = hR_{DD}\begin{pmatrix}\hat{I}_{k,x}\\ \hat{I}_{k,y}\\ \hat{I}_{k,z}\end{pmatrix}^T \cdot \begin{pmatrix}\frac{r^2-3x^2}{r^2} & -\frac{3xy}{r^2} & -\frac{3xz}{r^2}\\ -\frac{3xy}{r^2} & \frac{r^2-3y^2}{r^2} & -\frac{3xy}{r^2}\\ -\frac{3xz}{r^2} & -\frac{3yz}{r^2} & \frac{r^2-3z^2}{r^2}\end{pmatrix} \cdot \begin{pmatrix}\hat{I}_{l,x}\\ \hat{I}_{l,y}\\ \hat{I}_{l,z}\end{pmatrix} \tag{1.43}$$

The dipolar coupling constant is

$$R_{DD} = \frac{\mu_0 \gamma_k \gamma_l \hbar}{8\pi^2 r^3} \tag{1.44}$$

which shows that this interaction is relatively “short-sighted” due to the r^{-3} factor in R_{DD}. This is important for NMR techniques that depend on dipolar coupling such as cross-polarization (CP). In CP experiments, only spins that are close to each other (i.e., dipolar coupled) will appear in spectra if the contact time is kept short enough.

The reduced indirect spin-spin coupling tensor $\boldsymbol{K}_{kl}$ describes the coupling between spins that is mediated by the electronic structure.[4,9,10,26]

$$\boldsymbol{K}_{kl} = \left.\frac{\partial^2 E}{\partial \boldsymbol{\mu}_k\, \partial \boldsymbol{\mu}_l}\right|_{\boldsymbol{\mu}_k=0,\boldsymbol{\mu}_l=0} \tag{1.45}$$

The *J-coupling tensor* is related to $\boldsymbol{K}_{kl}$ by the following:[4]

$$\boldsymbol{J}_{kl} = \frac{h\gamma_k\gamma_l}{4\pi^2}\boldsymbol{K}_{kl} \tag{1.46}$$

1.3 Theoretical Computations of NMR Parameters

A brief theoretical description of NMR has been given. This provides a conceptual framework for thinking about the quantum chemical computation of NMR parameters: For a given set of nuclear coordinates (i.e., geometry), the total energy is calculated and then MS and spin-spin coupling tensors can be obtained by differentiation of the total energy.[7] In practice, this is challenging because these tasks can be computationally expensive. While there are many computational methodologies (e.g., Hartree-Fock, Coupled Cluster theory), the method of choice for large systems is Density Functional Theory (DFT).[29,30] DFT expresses the total energy of a system in its non-degenerate ground state in terms of the electron density. This reduces the number of spatial variables from 3N (where N is the number of electrons) to only three (i.e., the electron density in three dimensions).

For the computation of NMR parameters, there is a complication associated with the incorporation of magnetic fields when atomic-centered basis functions are used. This is the so-called gauge problem.[19] Briefly, the gauge problem is that with a finite basis set, the results of NMR calculations depend on the choice of gauge for the magnetic vector potential. One solution is to use gauge-including atomic orbitals (GIAOs), which removes the gauge dependence by introducing a field-dependent phase factor in the basis functions.[12] Regardless, the conceptual framework remains the same; the total energy is calculated and then differentiated to obtain the desired properties. Amsterdam Density Functional (ADF), the quantum chemistry program used in this thesis, uses GIAOs for NMR calculations. This method similarly decomposes the shielding tensor into diamagnetic and paramagnetic contributions.[31,32] Relativistic effects including spin-orbit coupling are also readily accounted for in NMR computations with ADF.[33,34]

1.4 NMR Spectroscopy of Silicon Nanoparticles

1.4.1 Cross-Polarization

As shown in ***Section 1.2.3***, NMR spectroscopy is inherently insensitive. However, hydride-terminated silicon nanoparticles (H-SiNPs) have the advantage of their surfaces being passivated with one of the most sensitive nuclei, namely, ^{1}H. Chapter 2 is also concerned with ^{19}F on the surface of H-SiNPs, which is another highly sensitive nucleus (**Table 1.1**). However, H-SiNPs are largely comprised of ^{29}Si, which has poor sensitivity and relatively low natural abundance. Therefore, cross-polarization (CP)[35] is typically used in NMR investigations of SiNPs to enhance the signal-to-noise (S/N) ratio of ^{29}Si experiments.

Table 1.1. Properties of NMR-Active Nuclei in Hydride-Terminated Silicon Nanoparticles.[36]

Isotope	**Spin quantum number, *I***	**Natural abundance (%)**	**Gyromagnetic ratio, γ (10^7 rad s^{-1} T^{-1})**
^{1}H	1/2	99.9885	26.7522128
^{19}F	1/2	100	25.18148
^{29}Si	1/2	4.6832	−5.3190

The most basic CP pulse sequence is shown in **Figure 1.4**. A full description of CP requires average Hamiltonian theory, which is beyond the scope of this chapter. A straightforward conceptual description will be given instead. The basic idea of CP is to transfer polarization from an abundant and sensitive nucleus like ^{1}H to an insensitive and dilute nuclear spin like ^{29}Si. For example, in a ^{29}Si{^{1}H} CP experiment, a π/2 pulse is applied to ^{1}H to generate transverse magnetization. Then, a spin-lock pulse is applied to ^{1}H with concurrent application of a contact pulse on ^{29}Si. Polarization transfer occurs when the Hartmann-Hahn match condition is satisfied,

$$\gamma^{1H} B_1^{1H} = \gamma^{29Si} B_1^{29Si} \tag{1.47}$$

where B_1^{1H} and B_1^{29Si} are the amplitudes of the spin-locking and contact pulses applied to ^{1}H and ^{29}Si, respectively. After the contact time, the free induction decay (FID) of ^{29}Si is acquired with ^{1}H decoupling. CP can provide a signal enhancement of up to $\gamma^{1H}/\gamma^{29Si}$ and has the advantage of depending on the relaxation of ^{1}H (typically fast relaxing) and not ^{29}Si (slow relaxing). Although ^{1}H and ^{29}Si have been used as an example, the same principles apply to other heteronuclear spin pairs. In the case of ^{29}Si{^{19}F} CP experiments for H-SiNPs, sensitivity is still a prominent challenge because fluorine is present in only trace quantities (**Chapter 2**).

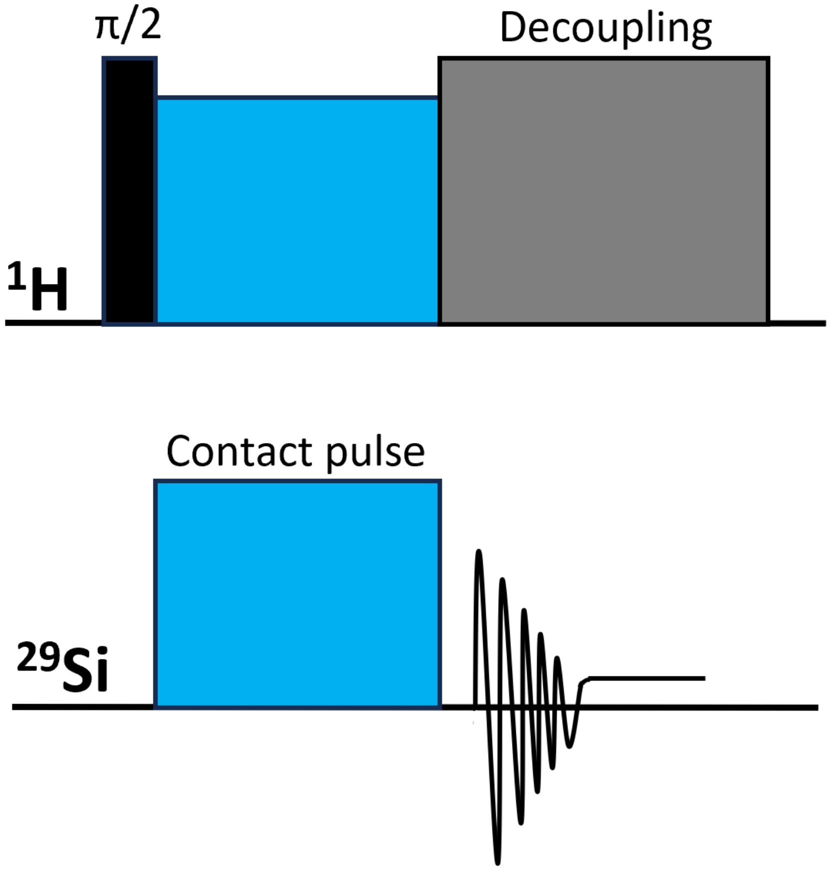

Figure 1.4. Cross-polarization pulse sequence with ^{1}H and ^{29}Si as the example nuclei.

1.4.2 Quantum Confinement and Chemical Shift Trends

Quantum confinement (QC) leads to many of the interesting properties of SiNPs; however, they can also be related to the trends observed in previous NMR studies of H-SiNPs.[37,38] As the size of H-SiNPs decreases, their bandgaps widen and their ^{29}Si chemical shift moves to a lower frequency. It is easiest to interpret this result in the context of the one-dimensional (1D) particle in a box, which is frequently used to provide a basic understanding of QC. Consider the Schrödinger equation for a subatomic particle of mass m (e.g., electron) in an infinite square potential well that is free to move along the x-axis in the interval $0 \leq x \leq L$:

$$-\frac{\hbar^2}{2m}\frac{d^2}{dx^2}\psi(x) = E\psi(x) \tag{1.48}$$

The normalized solutions are

$$\psi_n(x) = \sqrt{\frac{2}{\mathrm{L}}}\sin\left(\frac{n\pi x}{L}\right), \qquad n = 1,2,3\ldots \tag{1.49}$$

with the following energies:

$$E_n = \frac{\hbar^2 \pi^2 n^2}{2mL^2}, \qquad n = 1,2,3 \ldots \tag{1.50}$$

The spacing between two consecutive energy levels is,

$$\Delta E_{n+1,n} = \frac{\hbar^2 \pi^2}{2mL^2}\left[(n+1)^2 - n^2\right] \tag{1.51}$$

which shows that the gap grows larger as L decreases. This is a basic illustration of how shrinking the diameter of a quantum dot can increase its bandgap: as the particle dimensions shrink (like shrinking L), the spacing between energy levels grows larger. This is not an exact analogy since quantum dots are far more complex systems. However, the 1D particle in a box provides a straightforward framework to think about QC.

What is the connection between QC and the ^{29}Si chemical shift trend observed for H-SiNPs? Recall from ***Section 1.2.2***. that the expression for the elements of the paramagnetic shielding tensor has the form of Equation 1.8. The actual expression as formulated by Ramsey is,[20]

$$\sigma_{uv}^{p} = -\frac{e^2 \mu_0}{8\pi m_e^2} \sum_{n \neq 0} \left[\frac{\langle \psi_0 | \sum_i r_{iN}^{-3} \hat{L}_{Ni,u} | \psi_n \rangle \langle \psi_n | \sum_i \hat{L}_{i,v} | \psi_0 \rangle + \langle \psi_0 | \sum_i \hat{L}_{i,v} | \psi_n \rangle \langle \psi_n | \sum_i r_{iN}^{-3} \hat{L}_{Ni,u} | \psi_0 \rangle}{E_n - E_0} \right] \tag{1.52}$$

where ψ_0 and ψ_n are the ground and n^{th} excited state wavefunctions, respectively, with energies E_0 and E_n. r_{iN} is the distance of electron i from the nucleus N, while $\hat{L}_{Ni,u}$ and $\hat{L}_{i,v}$ are the angular momentum operators with respect to the nuclear and gauge origins, respectively (which are the same in the above expression). Equation 1.52 is inversely proportional to the energy gap between the ground and excited states that are being mixed. Therefore, a lower resonance frequency (i.e., a more shielded nucleus) is often related to an increasing HOMO-LUMO/bandgap due to the "less negative" paramagnetic contributions. Within the context of SiNPs, shrinking their diameter can increase the spacing between energy levels as shown above, yielding smaller paramagnetic deshielding contributions. While this is a general trend, there are several other factors (e.g., symmetry) that must be considered.

Chapter 2. Unmasking Fluorinated Moieties on the Surface of Hydride-Terminated Silicon Nanoparticles Using Solid-state NMR Spectroscopy

2.1 Introduction

Silicon nanoparticles (SiNPs) are pivotal nanomaterials due to their photoluminescence (PL),[39–48] biocompatibility,[49–51] tunable size,[39,52–54] and tailorable surface chemistry.[43,55–58] These factors have placed them at the frontier for applications in light-emitting diodes (LEDs),[59,60] photovoltaics,[61,62] sensors,[63] and as medical imaging agents.[51,64–66] Synthetic control of size and surface functionality enables researchers to govern the properties of SiNPs with fine precision.[43] The community's knowledge surrounding the influence of synthetic reaction parameters has expanded substantially. Using theory and experimentation, information ranging from fundamental structural insights[37,38] to the nature of crystal momentum conservation laws have been uncovered.[67] Still, an elusive question remains unanswered: what is the nature of fluorine on the SiNP surfaces?

Aqueous solutions of HF are widely used in the preparation of SiNPs, making the existence of fluorinated surface species probable.[50,53,60,61,68–72] However, the nature of these moieties remains unexplored, leaving a gap in our understanding of the surface structure of H-SiNPs. The presence of fluorinated moieties is of broad significance. It is well-established that halogens influence SiNP optical properties,[45] meaning that an understanding of the surface fluorine groups could be invaluable. Furthermore, the ubiquitous use of HF in preparing these nanomaterials makes a nuanced understanding of the resulting surfaces crucial. Fluorine is also relevant in the biological domain of SiNP applications, where there is growing interest in developing nanomaterial-based medical imaging agents.[73] A particularly attractive imaging modality is ^{19}F MRI,[74–76] for which SiNPs are excellent candidate contrast agents. Clues seen in X-ray photoelectron spectroscopy (XPS) analyses suggest fluorine is present in trace quantities;[37] however, detection limits challenge our ability to study these species further. This is one reason why ambiguity remains surrounding the analogous question about silicon wafers; despite years of study, the nature of fluorine on wafer surfaces cleaned with HF is still poorly understood.[77]

To better understand what fluorinated moieties may be present on the surface of H-SiNPs, it is helpful first to consider how HF etching of the SiO_2 matrix may lead to partial fluorination of the oxide-embedded silicon nanodomains. The currently accepted mechanism for HF etching of SiO_2 as described by Knotter is summarized as follows.[78] The first step is suggested to be the formation of an "O_3SiF" unit via a substitution reaction assisted by HF_2^- that replaces a surface silanol (O_3SiOH) with a terminal fluorine (**Scheme 2.1**a). Direct nucleophilic substitution reactions (i.e., S_N2) with O_3SiOH are improbable since nucleophiles cannot approach from the rear of the electrophilic center. After the formation of O_3SiF, a rear approach is possible, and three subsequent substitution reactions remove the O_3SiF unit as SiF_4 (**Scheme 2.1**a). These steps regenerate the surface silanol and enable the etching to proceed further, while SiF_4 reacts further with HF to form H_2SiF_6.[79]

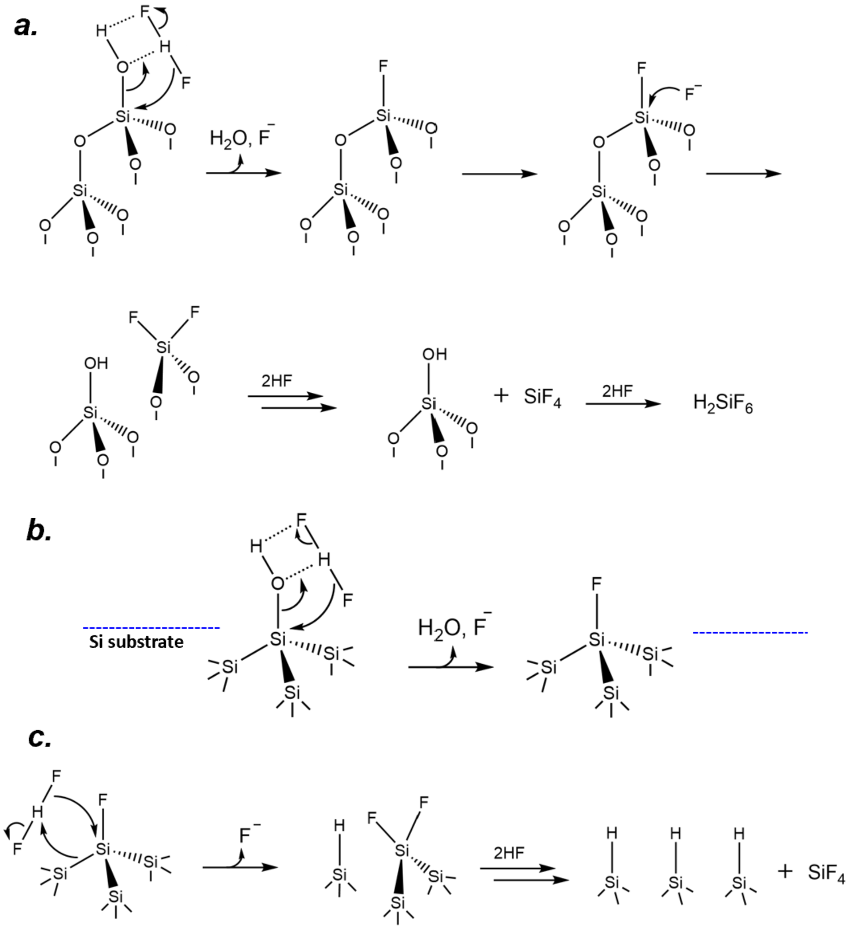

Scheme 2.1. (a) Proposed mechanism for the etching of SiO_2 in aqueous HF-based solutions. (b) Formation of a terminal Si−F group. (c) Mechanism of hydride termination of the underlying silicon substrate. Figure adapted from refs. 78 and 80.

HF etching leads to hydride passivation of the underlying silicon substrate. However, prior to two critical studies,[81,82] it was broadly accepted that the silicon surface generated by HF etching was terminated by fluorine. This conclusion was founded upon the hydrophobicity of the resulting surface, the strength of Si−F bonds, and the use of surface characterization techniques that are sensitive to fluorine and not hydrogen (e.g., XPS).[77] Furthermore, before hydride passivation takes place, the mechanism of HF etching does, in fact, contain transient fluorine termination.[77,80,81] This is evident when extrapolating the mechanism outlined in **Scheme 2.1**a to the point where the underlying silicon substrate is reached: elimination of a silanol group will form a terminal Si−F (**Scheme 2.1**b). However, fluorine termination is unstable due to the strong polarization induced at the silicon center.[77,81] This leads to subsequent reaction with nucleophiles and hydride-termination of the surface as shown in **Scheme 2.1**c. Limited polarization is induced by hydride passivation which makes the hydride-terminated surface remarkably stable.

Terminal Si−F groups can be stabilized via immersion of hydride-terminated Si(111) wafers in HF or by functionalization with methanol and subsequent treatment with HF.[83,84] The stability of terminal Si−F groups was attributed to the steric isolation of silicon sites on the atomically smooth Si(111) surface.[83] In other words, if Si−F is formed on Si(111), the configuration of the surface is such that nucleophiles are sterically prevented from further reaction. Although caution must be exercised when comparing the flat surfaces of Si wafers to the disordered surfaces of H-SiNPs, it is well established that local surface arrangements resembling Si(111) are possible on H-SiNPs as indicated by the infrared (IR) band corresponding to single Si−H bonds.[41,60] This suggests that it is possible to stabilize Si−F groups on the surface of H-SiNPs prepared by aqueous HF etching of an Si/SiO_2 composite. As the etching reaches the embedded silicon nanodomains, silanol groups may be exchanged for fluorine resulting in partial fluorination (**Scheme 2.1**b).

With this mechanism as a basis, a suite of characterization techniques and theoretical computations is presented to identify the fluorinated moieties on the surface of H-SiNPs prepared by thermal processing of hydrogen silsesquioxane (HSQ). The size and composition of H-SiNPs are assessed using powder X-ray diffraction (XRD), transmission electron microscopy (TEM), XPS, and energy dispersive X-ray spectroscopy (EDX). Solid-state nuclear magnetic resonance (NMR) spectroscopy, a robust analytical method to determine the atomic-level structure of semiconductors,[37,38,57,85–90] is also employed. Fluorinated surface moieties are selectively probed using ^{19}F and ^{29}Si NMR spectroscopy in combination with extensive quantum chemical computations to formulate a structural model of the surface of H-SiNPs.

2.2 Results

2.2.1 The Structure and Elemental Composition of H-SiNPs

The H-SiNPs studied here were prepared by thermal processing of HSQ. This method provides H-SiNPs with readily tuned sizes by altering the annealing temperature and dwell time.[37–39,41,42,52–54,56] Scherrer analysis of a powder XRD pattern for a sample of H-SiNPs (**Figure A1**) yields a mean crystallite size of 2.9 ± 0.1 nm which is consistent with the 6 nm H-SiNPs studied previously.[37] As Scherrer analysis gives the mean diameter of the crystalline domains, it does not reflect the total size of H-SiNPs which also contain a disordered surface and quasi-ordered subsurface (see below).[37] To further assess the particle dimensions, a batch of H-SiNPs was functionalized with 1-dodecene to render them solution processable and was imaged by TEM (**Figure A2**), giving a diameter of 5.19 ± 0.99 nm. The particles will now only be referred to by their nominal size (e.g., 6 nm). Elemental analysis was also performed before NMR measurements to determine the composition of the H-SiNPs. EDX spectroscopy (**Table A1**) confirms the presence of C (adventitious carbon), O, and Si, along with trace amounts of F (0.05 at%). Similarly, XPS analysis (**Figures A3** and **A4**) shows C, O, and Si. No F could be detected in the survey or high-resolution XPS spectra which is consistent with the EDX analysis that indicated that the quantities present were below the XPS detection limit.

Figure 2.1a shows the IR spectra of a sample pre- and post-NMR analysis. Both spectra exhibit a strong absorption feature at ~2100 cm^{-1} corresponding to the SiH$_x$ (X = 1, 2, 3) groups of the hydride-terminated surface. Alkyl stretching from 2800-2900 cm^{-1} is present in both spectra which is attributed to residual toluene from the drop-casting procedure used to prepare samples for IR spectroscopy. High-resolution Si 2p XPS spectra prior to NMR analysis (**Figure A4**) show that the particles are composed primarily of Si(0). The IR spectrum collected after NMR analysis (**Figure 2.1**a; seven months post-synthesis) contains comparatively weak absorption at *ca.* 1080 cm^{-1} (Si−O−Si stretching). This indicates that a very small amount of sample oxidation can take place over a period of months when they are stored in sealed zirconia NMR rotors under ambient conditions. There is also weak absorption around 3400 cm^{-1} corresponding to O−H stretching that is attributed to surface silanol groups and adsorbed water.[91]

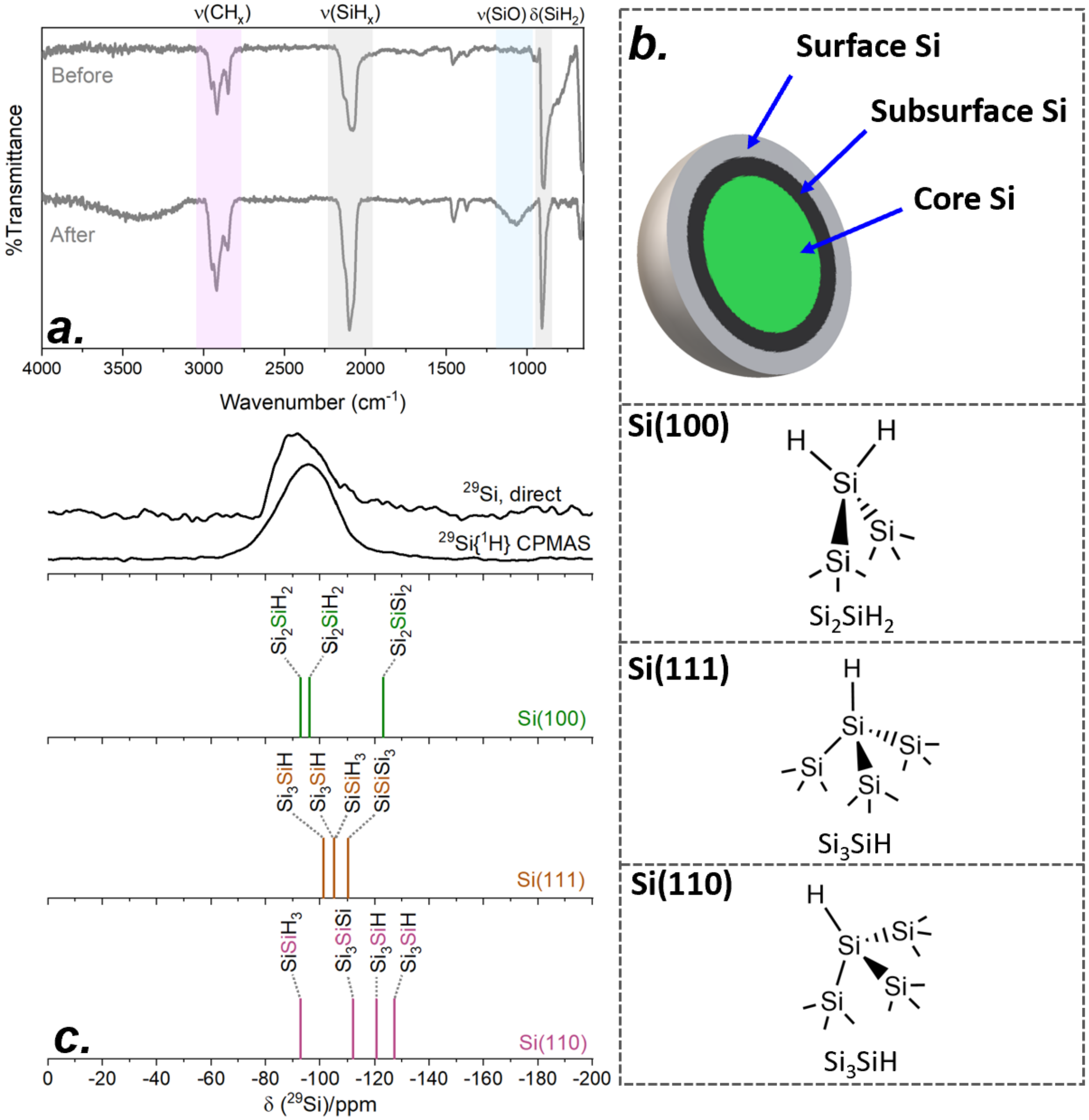

Figure 2.1. (a) IR spectra of 6 nm H-SiNPs collected before and after NMR analysis (post seven months). (b) Graded structure of H-SiNPs comprising a disordered surface (SiH$_x$ species), quasi-ordered subsurface, and a crystalline core. (c) Comparison of the calculated ^{29}Si chemical shifts for the hydride-terminated models to the experimental ^{29}Si MAS and ^{29}Si{^{1}H} CPMAS NMR spectra of 6 nm H-SiNPs ($\nu_{rot} = 10$ kHz). In (b) the orientation of the Si$_3$SiH groups reflects that of the specified crystal face. The colored atoms in (c) are those for which the chemical shifts are plotted.

It has been demonstrated that the structure of H-SiNPs comprises three domains: a disordered surface, a quasi-ordered subsurface, and a crystalline core (**Figure 2.1**b).[37,38] The contribution of each of these domains is dependent on the particle size. These conclusions were drawn from a suite of characterization techniques including XRD, IR, XPS, and NMR, with the three structural regimes being especially evident in the ^{29}Si NMR results. Since long-range order is not possible within the smallest particles, disordered SiH_x species ($X = 1, 2, 3$; **Figure 2.1**b) on the surface dominate for 3 and 6 nm H-SiNPs and are characterized by a broad peak spanning from −80 to −120 ppm. The disordered surface sites are similar for all particle sizes and have been identified in other NMR studies of SiNPs.[57,88] For larger particles (21 and 64 nm), the diamond cubic crystalline core is evident from the ^{29}Si MAS NMR by a single sharp resonance centered at −81 ppm. Between these two structural domains, there exists a subsurface of quasi-ordered silicon environments that are most salient in ^{29}Si{^{1}H} CPMAS NMR experiments for the 64 nm particles. A final NMR signature identified by these past studies is the presence of SiO_2 in partially oxidized particles. Oxidation manifests as a broadened peak at *ca.* −110 ppm, corresponding to silicon oxides with the primary species being Q^4 sites (silicon atoms involved in four siloxane bridges).[92–97] Building further, these structural motifs will serve as a point of reference for the identification of fluorinated surface species.

The ^{29}Si MAS and ^{29}Si{^{1}H} CPMAS NMR spectra for 6 nm H-SiNPs are shown in **Figure 2.1**c. These NMR spectra are virtually identical to those observed previously[37] and highlight the dominant contribution from SiH_x surface species. Furthermore, the absence of a distinct peak at −110 ppm in the ^{29}Si MAS and ^{29}Si{^{1}H} CPMAS spectra confirms that the particles are largely oxide-free. In **Figure 2.1**c, the bottom three theoretical spectra contain the computed ^{29}Si chemical shifts for the hydride-terminated models and are compared to the experimental ^{29}Si NMR spectra. The models were constructed by terminating slabs of the silicon crystal structure with the desired surface orientation in hydrogen, optimizing the geometry, and then computing the theoretical magnetic shielding values (see **Section 2.5**). The predicted values range from −90 to −130 ppm and strongly overlap with the experimental chemical shift range of the surface (−80 to −120 ppm). This indicates that the models formed here provide a high-quality approximation to the surface of H-SiNPs.

Attention should be given to how the nature of the surface hydrides in the models depends on the surface orientation in a fashion analogous to silicon wafers (**Figure 2.1**b). Si(100)-oriented models have a surface configuration of Si_2SiH_2, where the central silicon is involved in two Si−Si back bonds to the underlying silicon network and is terminated by two surface hydrides.[98] The Si(111) and (110) models have the configuration Si_3SiH, indicating three Si−Si back bonds and a single terminal hydride.[98] The difference between Si(111) and Si(110) lies in the fact that the Si−H bond is normal to the surface for Si(111) and at an angle for Si(110) (**Figure 2.1**b). In **Figure 2.1**c, groups such as $SiSiSi_3$, which correspond to silicon atoms that link adjacent hydride-capped silicon sites, are listed. $SiSiH_3$ groups grafted onto the (111) and (110) models are also plotted in **Figure 2.1**c since $SiSiH_3$ is known to exist on the surface of H-SiNPs.[41,60] In the remainder of this study, only the data for models based on Si(111) will be presented in the main text, while the others can be found in **Appendix A**. The general trends in the theoretical magnetic shielding values are consistent regardless of the silicon face on which the models are based.

2.2.2 Solid-state ^{29}Si NMR of HF-Etched SiNPs

Figure 2.2a shows the $^{29}Si\{^{19}F\}$ CPMAS NMR spectra for three replicate samples of H-SiNPs. In each spectrum, there are five distinct peaks labeled from ***i*** to ***v***, indicating that the fluorinated species present in H-SiNPs are reproducible. Peak ***iii*** is attributed to surface SiH_x species due to its overlap with the surface-selective $^{29}Si\{^{1}H\}$ CPMAS NMR spectrum (**Figure 2.2**b). Since only ^{29}Si sites proximate to ^{19}F are detected with $^{29}Si\{^{19}F\}$ CPMAS NMR spectroscopy, the detection of SiH_x species with this technique confirms the presence of fluorine on the surface of H-SiNPs. Furthermore, the computed ^{29}Si chemical shifts for SiH_x adjacent to fluorinated sites are invariant to the presence of a nearby fluorine as shown in **Figure 2.2**b (e.g., the chemical shift of an Si_3SiH moiety is unaltered by a nearby Si_3SiF). It is proposed that peak ***iii*** also contains contributions from O_3SiF groups (**Figure 2.2**c) based on two lines of evidence. First, previous NMR studies of fluorine-doped amorphous silica (*a*-SiO_2),[94,95,99] silica fluorinated with F_2 gas,[97] and silica nanoparticles fluorinated with NH_4F[93] suggest O_3SiF groups have chemical shifts in the range of peak ***iii***. It was hypothesized that the opening of siloxane bridges via fluorine substitution to form O_3SiF relieves strain, meaning that this configuration is energetically favorable.[94,95,99,100] Second, the DFT-computed ^{29}Si chemical shifts for O_3SiF groups overlap with peak ***iii*** as illustrated in **Figure 2.2**b, further supporting this assignment. Therefore, it seems that O_3SiF forms by two modes, namely, by replacing a silanol during HF etching[78] (**Scheme 2.1**a) and by fluorine-mediated opening of siloxane bridges to relieve strain.

Peak ***iv*** (−110 ppm) corresponds to silica, SiO_2.[37,92,93,96,97] However, this peak is not observed in the ^{29}Si MAS or $^{29}Si\{^1H\}$ CPMAS spectra (**Figure 2.1**c) which is consistent with the IR (**Figure 2.1**a) and XPS data (**Figure A4**) of these particles that show they are largely unoxidized. The dominant presence of peak ***iv*** in the $^{29}Si\{^{19}F\}$ CPMAS spectra indicates that fluorine and silicon oxides are in close proximity. This, along with the evidence for O_3SiF, suggests that fluorine is directly incorporated into local oxidation domains on the surface of H-SiNPs. This finding is consistent with previous studies demonstrating that fluorine can be incorporated into the oxide and at the Si/SiO_2 interface in thermally oxidized silicon wafers.[101–103] However, it must be emphasized that for the H-SiNPs studied here, the incorporation of fluorine into the oxide results from HF etching and is not thermally driven as can be the case for oxidized wafers. Given that silicon surface sites bonded to oxygen are electrophilic, they will be more susceptible to attack by nucleophilic fluorine species during HF etching. Thus, fluorine clusters near SiO_2.

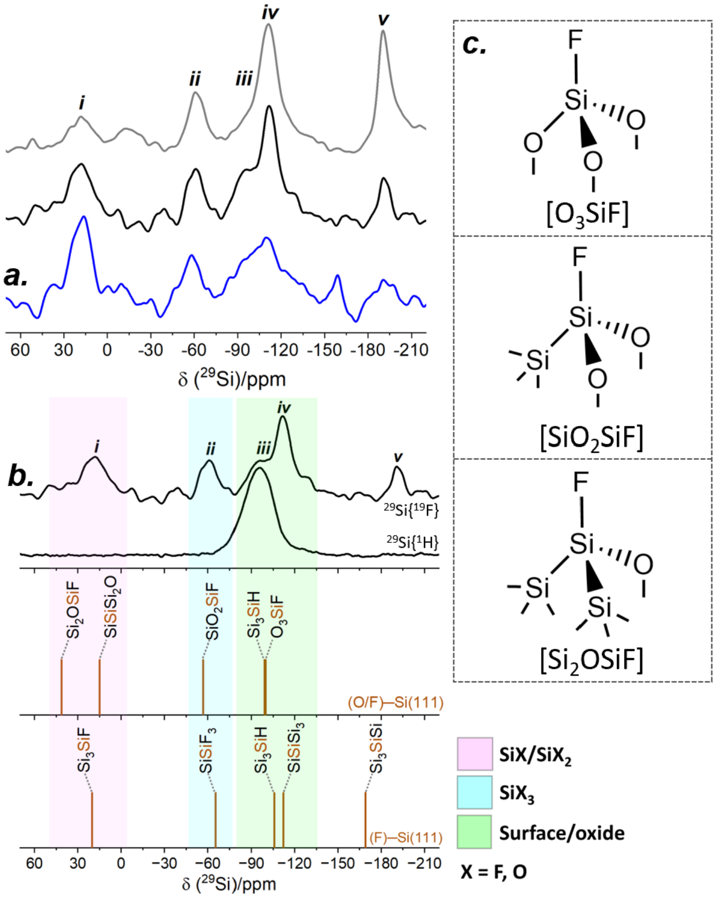

Figure 2.2. (a) $^{29}Si\{^{19}F\}$ CPMAS NMR spectra of 6 nm H-SiNPs showing five distinct sites labelled i-v (ν_{rot} = 10 kHz). (b) Comparison of the calculated ^{29}Si chemical shifts to an experimental $^{29}Si\{^{19}F\}$ (top trace) and $^{29}Si\{^1H\}$ CPMAS (bottom trace) spectra. The theoretical

^{29}Si chemical shifts are separated into models containing groups with both oxygen and fluorine (O/F)−Si(111) or fluorine alone (F)−Si(111). (c) Examples of (O/F)−Si groups.

The incorporation of fluorine into the oxide suggests that surface groups containing both fluorine and oxygen are possible (denoted as (O/F)−Si groups). Therefore, a series of computed ^{29}Si chemical shifts for groups of this nature are shown for Si(111) in **Figure 2.2**b, and experimental values reported in the literature for various (O/F)−Si groups are listed in **Table 2.1**. Using the theoretical results herein and previous experimental shifts, peak ***i*** is assigned to silicon atoms chemically bonded to one or two electronegative groups (i.e., some combination of fluorine and oxygen) such as Si_2OSiF (**Figure 2.2**c). Chemically similar groups are also possible for models based on other faces. For example, surface species such as Si_2SiF_2 and SiOSiFH are potential on Si(100) and have theoretical chemical shifts overlapping with peak ***i***. Silicon species bonded to one or two oxygen atoms (e.g., $SiSiSi_2O$) that are close to fluorinated sites can also contribute to peak ***i***. Indeed, this observation is consistent with fluorine not only being incorporated into the oxide but also clustering at the silicon/silicon oxide interface. In fact, the most probable location for a group such as Si_2OSiF is at the interface, since there are silicon atoms bridging the gap between the oxide network and hydride-terminated surface. As mentioned above, the clustering of fluorine in the oxide and at the interface has been observed in wafers.[101–103] The final groups that contribute to peak ***i*** are surface silicon species terminated by a single fluorine. This is supported by the overlap of the theoretical chemical shifts for groups such as Si_3SiF with peak ***i*** and the probable formation of terminal Si−F during HF etching as outlined in **Scheme 2.1**.

Table 2.1. Comparison of the ^{29}Si Chemical Shifts of Groups Observed in Fluorine-Doped and Fluorinated Silicas to the DFT-Computed Chemical Shifts for Analogous Groups.

Group	**Literature reported δ (^{29}Si)/ppm**			**Calculated δ (^{29}Si)/ppm**
	Ref. 97	**Ref. 93**	**Refs. 94,95**	
O_2SiF_2	−95	-	-	−106
O_3SiOH	−102	−102	-	-
O_3SiF	−106	−105	−103	−100, −101, −102[a]
O_4Si	−112	−112	−112	−105
O_4SiF	−119	−119	−125	−142
O_3SiF_2	−125	-	-	-
O_2SiF_3	−132	-	-	-

[a] The three calculated ^{29}Si chemical shift values for an O_3SiF group correspond (in order) to those computed for the models based on Si(111), Si(110), and the oxidized model.

Since peaks ***i*** (SiX; SiX_2 where X = F or O), ***iii*** (surface; O_3SiF), and ***iv*** (silicon oxides) have been assigned, only peaks ***ii*** and ***v*** remain unidentified. Peak ***ii*** is assigned to silicon species bonded to three electronegative atoms (SiX_3; X = F or O) such as SiO_2SiF (**Figure 2.2**c). This assignment is made based on the overlap of the theoretical ^{29}Si chemical shifts for these groups with peak ***ii***. In principle, peak ***ii*** could also correspond to $SiSiF_3$. However, $SiSiF_3$ is unlikely to exist due to the extreme polarization of the central silicon and steric accessibility of a terminal SiF_3. This means that SiF_3 will further undergo a rapid reaction and be lost as SiF_4 during HF etching, as it is a highly volatile species.

Finally, peak ***v*** is assigned to the $[SiF_6]^{2-}$ octahedra of Na_2SiF_6. As mentioned above, $[SiF_6]^{2-}$ is formed during the etching of SiO_2 with HF.[79] A comparison of the $^{29}Si\{^{19}F\}$ CPMAS NMR spectra for 6 nm H-SiNPs and Na_2SiF_6 (**Figure A5**) shows that both spectra contain peak ***v***. Furthermore, ^{23}Na NMR spectroscopy shows that both samples have two peaks at −5 and −16 ppm corresponding to the two crystallographic sodium sites in Na_2SiF_6 (**Figure A6**).[104] The presence of sodium is attributed to the etching of Pyrex stir bars and test tubes by HF during the synthesis procedure. Pyrex is etched by HF[105] and nominally contains approximately 4.2 mol% Na_2O.[106] Therefore, hexafluorosilicic acid formed by etching SiO_2 precipitates with sodium as Na_2SiF_6, which has low solubility in water and dilute solutions of aqueous HF.[107] It is noted that the amount of Na_2SiF_6 contamination is low since sodium could not be detected by EDX or XPS (**Table A1** and **Figure A3**), and no evidence for this compound is found in the XRD (**Figure A1**).

2.2.3 Solid-state ^{19}F NMR of HF-Etched SiNPs

Owing to the large gyromagnetic ratio of ^{19}F (~94% that of ^{1}H),[72] ^{19}F NMR spectroscopy is ideal for fingerprinting trace fluorinated species,[108] precisely the scenario faced here. The ^{19}F MAS NMR spectra for 6 and 21 nm H-SiNPs are shown in **Figure 2.3**a. The spectra contain an intense peak at −152 ppm, which corresponds to $[SiF_6]^{2-}$ from Na_2SiF_6,[93,109] confirming the ^{29}Si assignment of ***v*** above. The assignment of this peak is supported by a comparison of the ^{19}F MAS NMR spectra for 6 nm H-SiNPs and Na_2SiF_6 (**Figure A5**). Concerning other possible $[SiF_6]^{2-}$ species, there may be evidence for $(NH_4^+)_2SiF_6$ in the spectra since the ^{19}F chemical shift of this compound is around −127 ppm.[93] **Figure 2.3**a shows that a relatively intense signal is observed in this region for all samples, although it is sharper and more pronounced in the blue trace. However, there are no apparent sources of NH_4^+ during the synthesis, and no nitrogen was detected by EDX or XPS (**Table A1** and **Figure A3**).

Figure 2.3b compares the experimental ^{19}F NMR spectra to the DFT-computed ^{19}F chemical shifts for models containing various fluorine-terminated and (O/F)−Si groups. The lower frequency region of the ^{19}F MAS NMR spectra has a single broad feature spanning between −180 and −200 ppm. This feature is assigned to groups such as Si_3SiF capped by a single fluorine. Although adsorbed HF could appear in this range,[110] this is where the DFT-predicted ^{19}F chemical shifts of silicon species terminated by a single fluorine occur. Furthermore, the broad nature of this feature is consistent with Si−F in a distribution of environments as is expected for the disordered surface of H-SiNPs.[37,38] Thus, evidence for terminal Si−F groups is found in the ^{19}F and ^{29}Si NMR and is consistent with predictions based on the mechanism of HF etching.

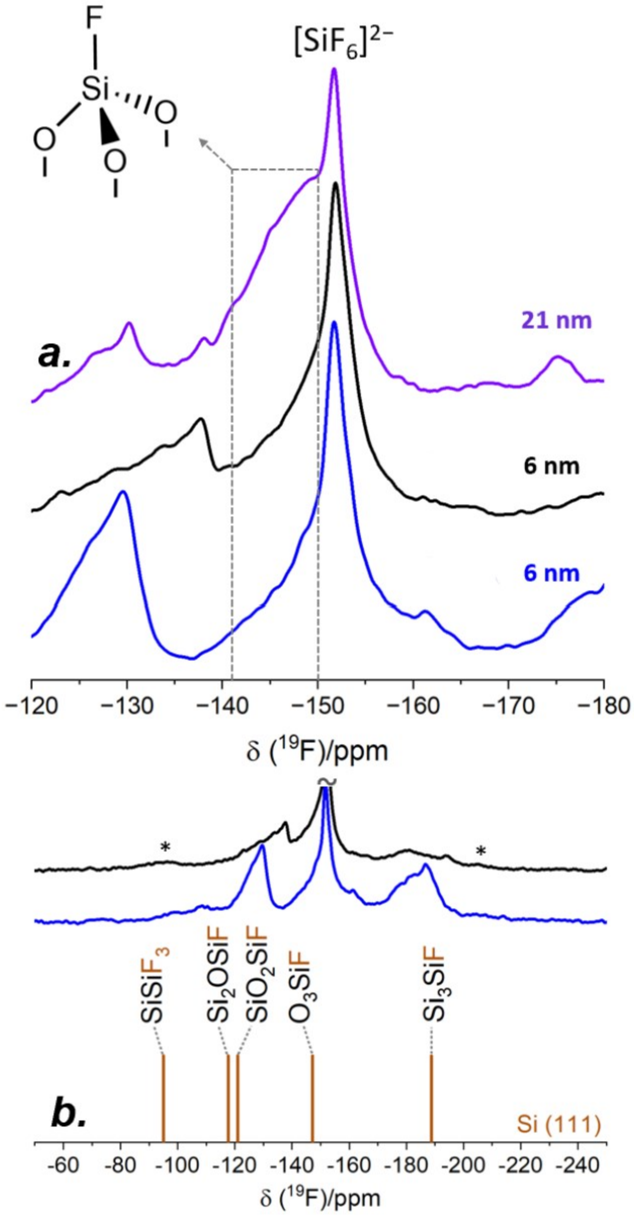

Figure 2.3. (a) Enlarged view of ^{19}F MAS NMR spectra of 21 nm and 6 nm H-SiNPs ($\nu_{rot} = 20$ kHz). (b) Comparison of the calculated ^{19}F chemical shifts to the experimental ^{19}F MAS spectra of 6 nm H-SiNPs. Asterisks (*) indicate spinning sidebands and the tilde (~) in (b) indicates that the peak corresponding to $[SiF_6]^{2-}$ has been truncated.

The ^{19}F MAS NMR spectra in **Figures 2.3**a and **2.3**b also contain a broad shoulder on the high-frequency side of the $[SiF_6]^{2-}$ peak at −152 ppm. This shoulder is tentatively assigned to O_3SiF in a distribution of chemical environments. As shown in **Figure 2.3**b, the computed ^{19}F chemical shift for O_3SiF for the Si(111) model overlaps with this shoulder (δ_{calc} /(^{19}F) = −147 ppm) and is consistent with previously reported values in the literature that range between −146 and −156 ppm (**Table 2.2**). The ^{19}F chemical shifts of O_3SiF groups in several different chemical environments have also been computed; the theoretical value for this group in an environment of extended oxidation is −149 ppm (**Figure A7**), which is close to the reported chemical shift of O_3SiF in fluorine-doped *a*-SiO_2 (−146 ppm).[94,95] Interestingly, when this group is placed on the Si(110) face (**Figure A8**), the theoretical ^{19}F chemical shift is −136 ppm, which is significantly different from that for O_3SiF on Si(111) or in the oxidized model. Nonetheless, this variability in computed ^{19}F chemical shifts for O_3SiF is consistent with the range of values reported in the literature, supporting the broad nature of the shoulder and the high sensitivity of ^{19}F chemical shift to changes in its chemical environment.

Table 2.2. Comparison of the ^{19}F Chemical Shifts of Groups Observed in Fluorine-Doped and Fluorinated Silicas to the DFT-Computed Chemical Shifts for Analogous Groups.

Group	Literature reported δ (^{19}F)/ppm			Calculated δ (^{19}F)/ppm
	Ref. 97	Ref. 93	Refs. 94,95	
O_2SiF_2	−160	-	-	−145
O_3SiF[a]	−156	−156	−146[c]	−147, −136, −149[d]
O_4SiF	−153	−153	−136/−137	−135
O_3SiF[b]	−149	−147	−146[c]	-
O_3SiF_2	−144	-	-	-
O_2SiF_3	−137	-	-	-

[a] Isolated O_3SiF groups.

[b] O_3SiF groups close to other groups of the same kind.

[c] Refs. 94 and 95 are earlier studies and do not determine whether the O_3SiF groups are isolated or close to other groups of the same kind.

[d] The three calculated ^{19}F chemical shift values for an O_3SiF group correspond (in order) to those computed for the models based on Si(111), Si(110), and the oxidized model.

It is challenging to make further assignments in the ^{19}F MAS NMR spectra due to the similar chemical shifts of several (O/F)−Si species. However, based on the theoretical ^{19}F values (**Figures 2.3**b, **A9**, **A10**), the region between *ca.* −100 and −150 ppm generally corresponds to (O/F)−Si species and Si_2SiF_2 groups. Given the strong evidence for (O/F)−Si groups in the ^{29}Si NMR data, the probability that these groups are on the surface of H-SiNPs is high. However, assigning peaks to specific (O/F)−Si species is not feasible given their similar ^{19}F magnetic shielding values and the resolution of the ^{19}F NMR spectra herein.

2.3 Discussion

2.3.1 Electronic Effects of Fluorine Termination

Above, a structural model has been proposed with various fluorinated moieties on the surface of H-SiNPs using experimental and theoretical NMR results. However, there has yet to be an exploration of how fluorine influences the local electronic environment of silicon. This information can be obtained by studying the origin of the deshielding of silicon species capped with a single fluorine (Si_3SiF; deshielded relative hydride-terminated silicon sites). This warrants further exploration because similar changes in ^{29}Si shielding have been observed in silicon nanosheets terminated with chlorine and hydroxyl ligands.[89,90] Given the importance of halogenation in silicon surface chemistry,[45,98,111] an understanding of the influence of fluorine termination on the electronic structure is needed.

To gain insight into the electronic influence of fluorine substitution, the relationship between a nucleus' magnetic shielding (MS) and its electronic structure is now considered. It is often only the isotropic chemical shift (δ_{iso}) that is reported, which is the isotropic shielding of a nucleus relative to a reference compound. However, MS is an anisotropic parameter described by a second-rank tensor. In the non-relativistic domain, the total MS tensor can be arbitrarily decomposed into a sum of the diamagnetic and paramagnetic terms.[20]

$$\boldsymbol{\sigma} = \boldsymbol{\sigma}^{\boldsymbol{d}} + \boldsymbol{\sigma}^{\boldsymbol{p}} \tag{2.1}$$

Diamagnetic shielding depends only on the ground electronic state. In contrast, paramagnetic shielding involves a sum over excited states and is quite responsive to changes in the local environment of a given nucleus. Detailed descriptions of the shielding tensor can be found elsewhere;[22,112,113] however, a brief theoretical overview of paramagnetic shielding will be given for the subsequent examination. When the gauge origin is at the nucleus of interest, the uv component of the paramagnetic shielding tensor (σ_{uv}^{para}) is given by[20]

$$\sigma_{uv}^{p} = -\frac{e^2\mu_0}{8\pi m_e^2}\sum_{n\neq 0}\left[\frac{\langle\psi_0|\sum_i r_{iN}^{-3}\hat{L}_{Ni,u}\,|\psi_n\rangle\langle\psi_n|\sum_i \hat{L}_{i,v}\,|\psi_0\rangle + \langle\psi_0|\sum_i \hat{L}_{i,v}\,|\psi_n\rangle\langle\psi_n|\sum_i r_{iN}^{-3}\hat{L}_{Ni,u}\,|\psi_0\rangle}{E_n - E_0}\right] \tag{2.2}$$

where ψ_0 and ψ_n are the ground and n^{th} excited state wavefunctions, respectively, with eigenvalues (energies) E_0 and E_n. r_{iN} is the distance of electron i from the nucleus N, while $\hat{L}_{Ni,u}$ and $\hat{L}_{i,v}$ are the angular momentum operators with respect to the nuclear and gauge origins, respectively (which are the same in the above expression). This equation states that paramagnetic shielding arises from the mixing of excited singlet state character into the ground state through the interaction of the electrons with the external magnetic field ($\hat{L}_{i,v}$) and the magnetic moment of the nucleus of interest ($r_{iN}^{-3}\hat{L}_{Ni,u}$). However, this formulation is only suitable for simple molecules and is not implemented in modern computational software. Within the gauge-including atomic orbital formalism used by ADF, paramagnetic shielding is decomposed into contributions from the coupling of occupied molecular orbitals (MOs) with both virtual MOs and other occupied MOs.[21,114,115] It is the former kind of coupling that is largely of importance for below. The occupied-virtual MO couplings can be subject to pairwise analysis[21] by considering integrals of the type

$$\langle \varphi_b | \hat{L}_k | \varphi_a \rangle \tag{2.3}$$

where $k = x, y, z$ and φ_a and φ_b are occupied and virtual MOs, respectively. If the new state generated by the action of the angular momentum operator on the occupied MO ($\hat{L}_k | \varphi_a \rangle$) overlaps with the unaltered virtual MO ($\langle \varphi_b |$) then a pair of MOs can contribute to MS.[21] Therefore, group theory can be used to determine selection rules for MO couplings.

Analysis of $\boldsymbol{\sigma}^{\mathbf{p}}$ can be extremely useful for understanding the electronic environment of a nucleus. Due to the r^{-3} factor in the operator $r_{iN}^{-3}\hat{L}_{Ni,u}$, paramagnetic shielding is relatively "short-sighted" and effectively samples the local environment about the nucleus of interest. Furthermore, the energy difference in the denominator ($E_n - E_0$) means that the largest contributions come from the frontier MOs since they bring the smallest difference in energy. Therefore, analyzing the contributions from frontier MOs around a fluorine-terminated silicon model can also be informative for understanding the electronic environments around fluorinated sites in microcrystalline and nanoscale silicon systems.

To perform the MO analysis, Si_3SiH and Si_3SiF have been modeled in Si(111)-like configurations contained within clusters of C_{3v} symmetry (**Figure A11**; the chemical formulae for the clusters are $Si_{10}H_{16}$ and $Si_{10}H_{15}F$, respectively) and the MS has been computed. The pairwise contributions of the canonical MOs to $\boldsymbol{\sigma}^{\mathbf{p}}$ can be computed using ADF. However, three methodological points should be noted. First, the calculation must be performed with the cluster already in its principal axis system (PAS). Second, the analysis can only be performed at the scalar- or spin-orbit-ZORA levels of theory. Lastly, symmetry must be disabled because the analysis uses the spin-orbit branch of the NMR code, which requires that symmetry be disabled.

The clusters were optimized at the PBE0/TZ2P level of theory. The MO symmetries were then obtained from single point calculations on the optimized clusters at the scalar-

ZORA/PBE0(50)/TZ2P level of theory. NMR calculations were then carried out at the same level as the single point calculations to obtain the shielding tensors for the central silicon atoms in Si_3**Si**H and Si_3**Si**F (boldface will now be used to indicate the atoms for which the shielding tensors were computed). Consistent with the C_{3v} symmetry, both computed shielding tensors (**Table 2.3**) are axially symmetric with σ_{33} being the unique component for each. These initial NMR calculations also showed that the clusters were already in their PAS; for both clusters, σ_{11}, σ_{22}, and σ_{33} coincide with the molecular $x, y,$ and z axes, respectively, with z corresponding to the C_3 axis of each model. Finally, a second NMR calculation was performed for each at the same level of theory to obtain the canonical MO contributions.

For Si_3**Si**H, the principal components of the total shielding tensor are σ_{11} = 490.22 ppm, σ_{22} = 490.24 ppm, and σ_{33} = 517.25 ppm. Upon substitution of fluorine for hydrogen, the total shielding tensor is σ_{11} = 277.10 ppm, σ_{22} = 277.11 ppm, and σ_{33} = 510.59 ppm. The deshielding of Si_3**Si**F is clearly driven by the magnitudes of σ_{11} and σ_{22}. $\boldsymbol{\sigma^d}$ is similar for both Si_3**Si**H and Si_3**Si**F, meaning that the deshielding of Si_3**Si**F is driven by $\boldsymbol{\sigma^p}$ as expected. Relative to Si_3**Si**H, σ_{11}^p and σ_{22}^p are more negative by about 204 ppm for Si_3**Si**F, while σ_{33}^p is similar for both.

Table 2.3. ^{29}Si Magnetic Shielding Tensors for Si_3**Si**H and Si_3**Si**F Groups in Models With C_{3v} Symmetry.

Contribution	σ_{11}	σ_{22}	σ_{33}	$^a\sigma_{iso}$
$Si_{10}H_{16}$				
σ^d (total)	878.57	878.58	880.70	879.28
σ^p (gauge)	3.26	3.27	2.25	2.93
σ^p (occ-occ)	−17.43	−17.39	93.67	19.62
σ^p (occ-vir)	−374.18	−374.22	−459.37	−402.59
σ^p (total)	−388.35	−388.35	−363.45	−380.05
σ (total)	490.22	490.24	517.25	499.23
$Si_{10}H_{15}F$				
σ^d (total)	869.13	869.13	883.84	874.03
σ^p (gauge)	2.62	2.62	1.68	2.31
σ^p (occ-occ)	−104.12	−103.95	116.73	−30.44
σ^p (occ-vir)	−490.52	−490.70	−491.67	−490.96
σ^p (total)	−592.03	−592.03	−373.26	−519.10
σ (total)	277.10	277.11	510.59	354.93

[a] The isotropic shielding is the average of σ_{11}, σ_{22}, and σ_{33}.

The breakdown of the components of $\boldsymbol{\sigma}^{\mathbf{p}}$ into MO couplings is now considered. **Table 2.3** shows that the occupied-occupied MO couplings contribute −104 ppm to σ_{11}^{p} and σ_{22}^{p} for Si_3**Si**F and only −17 ppm to the corresponding components for Si_3**Si**H. The occupied-virtual MO couplings contribute approximately −490 ppm to σ_{11}^{p} and σ_{22}^{p} for Si_3**Si**F and −374 ppm for Si_3**Si**H. Therefore, larger deshielding contributions from both occupied-occupied and occupied-virtual MO couplings give rise to more negative σ_{11}^{p} and σ_{22}^{p} for Si_3**Si**F. The distinct effect on σ_{11}^{p} and σ_{22}^{p} can be partially understood by considering the symmetry properties of the angular momentum operators ($\hat{L}_k; k = x, y, z$) and the frontier MOs of the two cluster models. The angular momentum operators transform as the rotational operators, thus for the C_{3v} point group, $\hat{R}_x$ and $\hat{R}_y$ transform as *E*, while $\hat{R}_z$ transforms as A_2. Considering the frontier MOs, the HOMO for $Si_{10}H_{16}$ transforms as A_2, and the doubly degenerate HOMO-1 belongs to the *E* representation (**Figure 2.4**a). It should be noted that HOMO and HOMO-1 are effectively degenerate since their computed energies differ by only 0.004 eV (0.39 kJ/mol). In terms of unoccupied MOs, the LUMO is fully symmetric under all operations of the point group and therefore transforms as A_1.

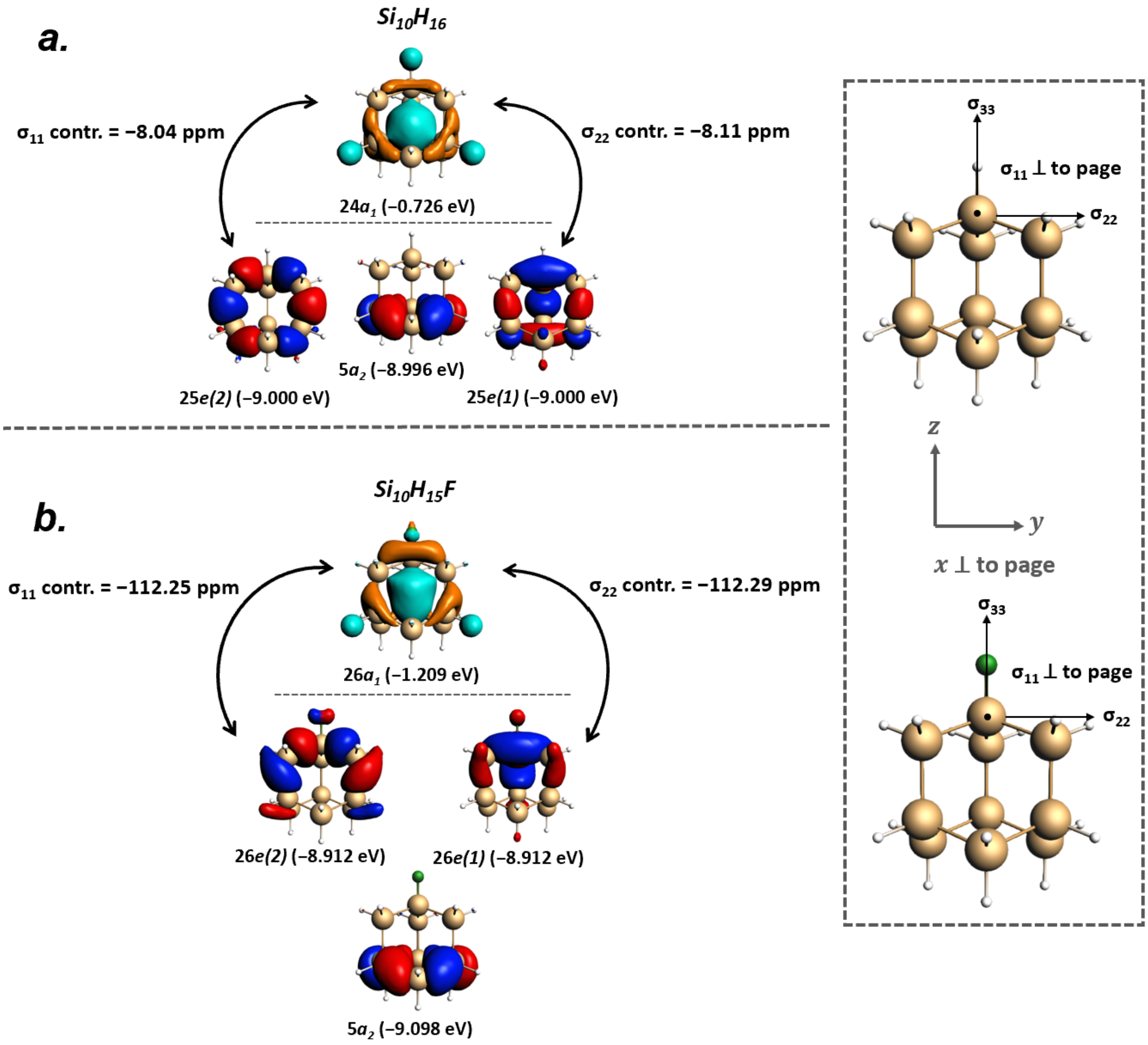

Figure 2.4. (a) Paramagnetic shielding contribution to $\mathrm{Si_3}$**Si**H arising from HOMO-1↔LUMO mixing. (b) Paramagnetic shielding contribution to $\mathrm{Si_3}$**Si**F arising from HOMO↔LUMO mixing. The spacing between MOs in both panels is not an exact representation of the energy difference between MOs.

As seen in the $\mathrm{Si_{10}H_{16}}$ cluster, the highest occupied MOs of the $\mathrm{Si_{10}H_{15}F}$ cluster (**Figure 2.4**b) also belong to the *E* and A_2 representations and the LUMO transforms as A_1. However, the pair of occupied *E* MOs now lie higher in energy than the A_2 MO (they are essentially degenerate in $\mathrm{Si_{10}H_{16}}$). In both clusters, the pair of *E* orbitals can influence $\boldsymbol{\sigma}^{\mathbf{p}}$ by coupling with the respective LUMOs (A_1). Recalling that the angular momentum operators have the same symmetry properties as the rotational operators, the following integral describes the coupling of these MOs induced by the applied magnetic field.

$$\langle a_1|\hat{L}_k|e\rangle \tag{2.4}$$

By taking the direct product of the three-center integrand, the fully symmetric representation is only contained for integrals involving $\hat{L}_x$ and $\hat{L}_y$.

$$A_1 \otimes \begin{bmatrix} E \\ A_2 \end{bmatrix} \otimes E = \begin{bmatrix} A_1 + A_2 + E \\ E \end{bmatrix} \tag{2.5}$$

Hence, the coupling of the occupied *E* orbitals in both clusters with the respective LUMOs can only contribute to σ_{11} and σ_{22} since these principal axes are collinear with the axes of the rotational operators $\hat{R}_x$ and $\hat{R}_y$, respectively. Although the coupling of these MOs can contribute to σ_{11} and σ_{22} for both clusters, the magnitudes of the deshielding contributions are significantly different. For Si_3**Si**H, the mixing of the occupied *E* orbitals with the LUMO only contributes approximately −8 ppm to σ_{11} and σ_{22}. For Si_3**Si**F, the mixing of the occupied *E* orbitals with the LUMO has a large contribution of −112 ppm. This is the largest contribution from any pair of MOs computed for either cluster. Two factors can explain the different contributions from these frontier MOs in each cluster. First, the coupling of the *E* MOs with the LUMO is stronger for Si_3**Si**F (**Table A2**). Second, the energy gap between the *E* MOs and the LUMO is smaller for $Si_{10}H_{15}F$ and leads to a larger magnitude contribution (8.27 eV gap for $Si_{10}H_{16}$ and 7.70 eV for $Si_{10}H_{15}F$). Hence, the coupling of the *E* MOs with the LUMO is one of the key factors driving the deshielding of Si_3**Si**F. While other MO pairs contribute, the leading contributions have been examined and some of the theoretical background underpinning the observed trends in MS has been provided. It is expected that the deshielding of chlorine-capped ^{29}Si sites recently observed in chlorine-terminated silicon nanosheets is also driven by the magnitudes of σ_{11} and σ_{22}.[53,54]

2.3.2 Challenges With Fluorine Surface Chemistry

During this study, Teflon contamination was a consistent challenge. This fluoropolymer is ubiquitous in chemistry labs and is chemically inert. However, ^{19}F signal from Teflon was observed in ^{19}F NMR spectra originating from two sources. First, Teflon signal arising from the caps of NMR rotors made the interpretation of early NMR spectra nearly impossible due to the low fluorine content in H-SiNPs (see above). This resulted in the ^{19}F background signal from the rotor caps overwhelming the signal from the H-SiNPs and reduced fluorine caps were necessary to limit the background interference. NMR probes can also have a strong ^{19}F background that can cause similar problems, meaning that F-free stator housing and probe components may be required. These hardware issues are, in principle, straightforward to correct, although not always readily accessible in many research facilities. However, addressing hardware challenges alone is not sufficient to solve the Teflon problem.

Teflon contamination during synthesis can originate from stir bars, beakers, and centrifuge tubes composed of Teflon. A comparison of the ^{19}F NMR spectra of Teflon tape (**Figure 2.5**a; green trace) and 6 nm H-SiNPs prepared using a Teflon-coated stir bar for HF etching (**Figure 2.5**a; black trace) shows minor Teflon contamination of the nanoparticles. The beaker used during the HF etching of this sample was composed of polypropylene, and the subsequent extraction was performed with polyethylene pipettes and Pyrex test tubes. Hence, the contamination originated from the stir bar, which was likely abraded away as it stirred the Si/SiO_2 composite. One solution that addresses this challenge is to use a Pyrex stir bar during etching, as indicated by the grey trace in **Figure 2.5**a. Aside from using a Pyrex stir bar, this sample was prepared under otherwise identical conditions, and no Teflon contamination is observed. Another sample prepared with a Pyrex stir bar (blue trace in **Figure 2.3**a) also does not show evidence of Teflon contamination. Furthermore, the purification of functionalized SiNPs using high-speed Teflon centrifuge tubes has also led to prominent Teflon contamination. Therefore, caution should be exercised during future studies of nanomaterials prepared with Teflon lab equipment, especially if fluorine quantification is a desired part of the analysis. As a final note, the reader is reminded that glass is etched by HF, and therefore, the use of Pyrex stir bars must be carried out with caution since they may be slowly etched with time.

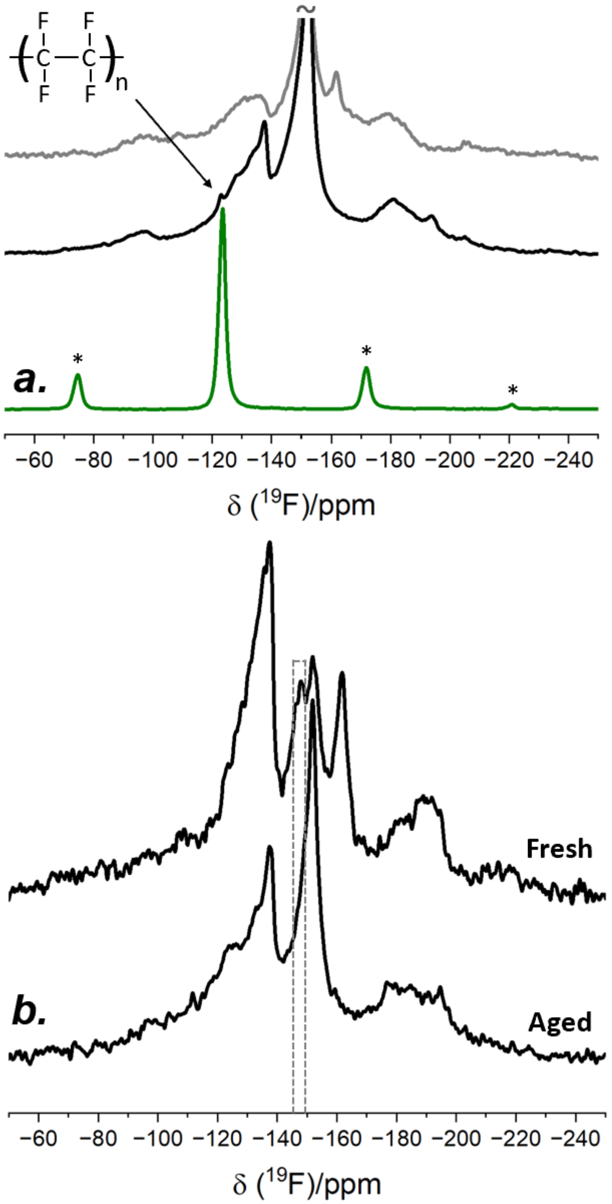

Figure 2.5. (a) ^{19}F MAS NMR spectra of Teflon (green) and 6 nm H-SiNPs prepared using a Teflon (black) or Pyrex (grey) stir bar (ν_{rot} = 18-20 kHz). (b) Variation of ^{19}F spectra including the disappearance of the peak at −161 ppm (ν_{rot} = 10 kHz). The tilde (~) in panel (a) indicates that the upper half of the peak corresponding to $[SiF_6]^{2-}$ has been truncated.

Two final matters to consider. First, while the ^{29}Si NMR signatures for H-SiNPs do not change significantly with time, the ^{19}F NMR signatures for some samples exhibit changes. **Figure 5**b shows the ^{19}F MAS NMR spectra of a sample of 6 nm H-SiNPs collected immediately after synthesis and approximately six weeks later. Initially, a prominent peak at −161 ppm is observed;

however, it is essentially gone after six weeks. While this peak is near the reported liquids ^{19}F chemical shift of SiF_4,[116] this species is too volatile to be present. Therefore, this peak is attributed to a surface-adsorbed fluorine species (e.g., a trace fluorine salt) that reacts further to form more $[SiF_6]^{2-}$. This has been observed for silicon, germanium, and gallium arsenide surfaces treated with HF solutions buffered with ammonium fluoride.[117] Frictional heating induced by magic angle spinning ($\Delta T > 20$ K) may also drive this reaction toward the formation of $[SiF_6]^{2-}$ by assisting surface rearrangements.

Figure 2.5b illustrates that other changes also occur in the ^{19}F NMR fingerprints with time. Initially, a peak at −149 ppm is approximately equivalent in intensity to $[SiF_6]^{2-}$ at −152 ppm. After five weeks, this peak is partially masked and appears as a shoulder on the high-frequency side of the $[SiF_6]^{2-}$ peak (this shoulder has been assigned to O_3SiF). This is also consistent with forming more $[SiF_6]^{2-}$ as the sample ages. However, after these initial changes, no more variation in the ^{19}F NMR results is observed (i.e., the NMR signatures are stable). In this paper, all ^{19}F NMR spectra of 6 nm H-SiNPs have been shown in their stable form for reproducibility and clarity (aside from those in **Figure 2.5**). It is also noted that the ^{19}F NMR results for some samples exhibit no variation right from the start. For example, the ^{19}F NMR results for the sample shown in a blue trace in this work did not change with time. Collectively, this suggests that the surface of H-SiNPs and its associated adsorbed species are complex, whereby surface rearrangements may occur. While the fluorinated surface moieties are reproducible (see above), it may be that the adsorbed species can vary, leading to the intensity changes or disappearance of peaks for some samples.

2.4 Conclusions

This study combines experimental and theoretical analysis of fluorinated species on the surface of H-SiNPs prepared by thermal processing of HSQ. The ^{29}Si NMR data reveals that fluorine is incorporated into local oxidation domains on the surface of H-SiNPs. This conclusion is drawn from the dominant presence of Q^4 species in $^{29}Si\{^{19}F\}$ CPMAS NMR spectra despite the particles themselves being largely oxide-free. Evidence for fluorinated species residing at the interface between the hydride-terminated surface and the silicon oxide network is also found. This is implicated by distinct peaks in the $^{29}Si\{^{19}F\}$ CPMAS NMR spectra that quantum chemical computations suggest corresponds to silicon atoms chemically bonded to one, two, or three electronegative atoms (i.e., F, O, or a combination of both). The localization of fluorine in the oxide and at the silicon/silicon oxide interface is consistent with past studies of silicon wafers. Surface sites terminated by a single fluorine (e.g., $Si_3\mathbf{Si}F$) are also identified by the experimental and theoretical ^{19}F and ^{29}Si NMR data. Relative to hydride passivation, ^{29}Si sites terminated by fluorine are deshielded. Quantum chemical modeling reveals that this is driven by deshielding contributions to σ_{11} and σ_{22} that can be partially explained by the symmetry properties of some of the frontier MOs. The formation of terminal Si−F groups is also consistent with the proposed mechanism of HF etching.

Collectively, this work fills a long-standing knowledge gap about the surface structure of SiNPs after HF etching. With the information gained herein, future work can be undertaken to refine the proposed surface model of fluorinated SiNPs and exploit this knowledge for applications in biological and optoelectronic domains.

2.5 Materials & Methods

As an aide to the reader, the NMR, IR, and XPS data presented in the main text and **Appendix A** are color-coded such that spectra shown in the same color correspond to those collected for the same sample. To obtain sufficient sample volume, each NMR rotor was packed with H-SiNPs from one to three batches of particles prepared by HF etching of Si/SiO_2 composite. Hence, one "sample" in this paper refers to those H-SiNPs that were packed into a rotor and analyzed using NMR spectroscopy. Other spectroscopic data for each sample was acquired as outlined later in this section.

2.5.1 Starting Materials

Hydrofluoric (Electronic grade, 48−50%) and sulfuric (reagent grade, 95−98%) acids were purchased from Fisher Scientific and Caledon Laboratory Chemicals, respectively. Fuming sulfuric acid (reagent grade, 20% free SO_3 bases), trichlorosilane (99%), toluene (HPLC grade), ethanol (reagent grade), 1-dodecene (95.0%), and benzene (anhydrous, 99.8%) were purchased from Sigma-Aldrich.

2.5.2 Synthesis of Hydrogen Silsesquioxane (HSQ)

HSQ was synthesized using a modified literature procedure.[118] Briefly, 210 mL of dry toluene was added dropwise to a mixture of concentrated (70 mL) and fuming (32.5 mL) sulfuric acid under an argon atmosphere with continuous stirring using a Teflon-coated stir bar. A second solution of dry toluene (510 mL) and trichlorosilane (75 mL) was subsequently added dropwise to the reaction mixture with continuous stirring and under a constant argon flow. After the second addition, the toluene layer was isolated and washed twice with 900 mL solutions of concentrated H_2SO_4:H_2O (volumetric ratio of 1:2). $MgSO_4$ and $CaCO_3$ were then added to the toluene layer and the mixture was continuously stirred overnight for drying purposes. The mixture was then centrifuged for 20 min at 12,000 rpm to collect the supernatant, which was subsequently filtered with a Buchner funnel. After removing toluene on a rotary evaporator, HSQ was obtained as a white solid.

2.5.3 Preparation of 6 and 21 nm H-SiNPs

H-SiNPs were prepared using a procedure developed by Veinot *et al.*[39,53] HSQ was thermally processed in a zirconia boat (Almath Crucibles Ltd.) using a horizontal tube furnace (Sentro Tech) under a flowing 100% Ar or 5% H_2/95% Ar atmosphere with the temperature set to 1200 °C or 1400 °C (ramp rate of 5°C/min) for 6 and 21 nm particles, respectively. A 1 h dwell time was used in the syntheses of both particle sizes. The resulting dark brown composite was mechanically ground in 100% ethanol using an agate mortar and pestle to form a light brown suspension. The suspension was then transferred using a glass Pasteur pipette to a thick-walled, pear-shaped 500 mL glass flask containing high-purity glass beads and shaken overnight with a wrist action shaker. To obtain freestanding H-SiNPs, approximately 1 g of the composite in question was treated with an etching solution comprised of ethanol, distilled water, and aqueous 49% HF (1:1:1). In a typical etch, 1 g of the composite was dispersed in 10 mL of 100% ethanol and sonicated for 30 s in a polypropylene beaker. Subsequently, distilled water (10 mL) was added to the composite/ethanol mixture and sonicated for another 30 s. Finally, the etch was commenced upon adding aqueous 49% HF (10 mL) with continuous stirring using a Pyrex or a Teflon-coated stir bar. (Note: Using a Teflon-coated stir bar can lead to trace Teflon contamination as explained in ***Section 2.3.2***). Completion of the etching was indicated by a change in color of the initial brown suspension to a light-yellow orange, which typically occurred after 60 to 70 min. The etching process was quenched upon adding toluene and the hydrophobic H-SiNPs were extracted into Pyrex test tubes using a polyethylene pipette. After extraction, the H-SiNP/toluene suspension was centrifuged for 5 min, and the supernatant was removed and discarded. This process was repeated in triplicate. After the third round of centrifugation, the supernatant was removed, and the H-SiNPs were dispersed in benzene, transferred into a vial, and freeze-dried using the vacuum on a standard Schlenk line.

2.5.4 Air-Sensitive X-ray Photoelectron Spectroscopy (XPS)

After the H-SiNPs were dispersed in benzene (immediately before freeze drying) a Pasteur pipette was used to drop cast benzene suspensions of H-SiNPs onto pieces of copper foil which were then transferred into a glove box for storage. An inert atmosphere vessel was used to transport the prepared XPS samples from the glove box to the XPS instrument for measurements. Air-sensitive XPS was carried out on a PHI VP3 Scanning Probe XPS system equipped with a monochromatic Al K_α radiation source (1486.6 eV) operating at 49.18 W. High-resolution spectra were measured using an analyzer pass energy of 55 eV and steps of 0.09 eV. Survey spectra were measured using a pass energy of 224 eV and steps of 0.8 eV. All spectra were calibrated to the aliphatic component of the C 1s of adventitious carbon (284.8 eV) and fit using the CasaXPS (VAMAS) software with a Shirley-type background. When fitting the Si 2p region, the area ratio for the spin-orbit couple doublet was fixed to 2:1 with the splitting fixed to 0.62 eV.

2.5.5 Transmission Electron Microscopy (TEM)

H-SiNPs were first rendered solution processable with 1-dodecene using a well-established procedure.[39] A dilute toluene suspension of the resulting dodecyl-terminated SiNPs was deposited onto an ultrathin carbon-coated copper grid (Electron Microscopy Inc.) Bright-field TEM images were acquired using a JEOL JEM-ARM200CF S/TEM electron microscope at an accelerating voltage of 200 kV. Images were analyzed using the ImageJ software.

2.5.6 Energy Dispersive X-ray Spectroscopy (EDX)

EDX was performed on a Zeiss Sigma 300 VP-FESEM equipped with a Bruker EDX spectroscopy system. The EDX system contains dual silicon drift detectors, each with an area of 60 mm^2 and a resolution of 123 eV.

2.5.7 Powder X-ray Diffraction (XRD)

Powder XRD patterns were collected on a Bruker D8 Advance diffractometer after NMR analysis. 6 nm H-SiNPs were removed from the zirconia NMR rotor, dispersed in toluene, and drop cast onto a zero background Si crystal plate. Diffraction patterns were collected in the 2θ range of 5-90° in 0.0197° increments. The crystallite sizes were estimated using the Scherrer equation:

$$d_{XRD} = \frac{K\lambda}{\beta cos\theta}$$

where d is the mean crystallite size, K is the shape factor which is equal to 0.94 for spherical crystallites of a cubic system,[119] λ is the X-ray wavelength ($\lambda_{CuK\alpha}$ = 0.15406 nm), β is the full-width-at-half-maximum (FWHM) of the reflections (rad), and θ is the Bragg angle (rad).

2.5.8 Fourier Transformed Infrared Spectroscopy (FTIR)

FTIR was performed on a Thermo Nicolet 8700 FTIR spectrometer with a Continuum FTIR microscope by drop-casting a toluene suspension of H-SiNPs onto a silicon wafer. A background spectrum was acquired for the silicon wafer alone.

2.5.9 Solid-state Nuclear Magnetic Resonance (NMR) Spectroscopy

All NMR spectra were collected at a field strength of 9.39 T on a Bruker Avance III HD 400 MHz NMR spectrometer using a Phoenix NMR NB 400 MHz H/FXY 3.2 mm MAS probe with an F-free stator housing for a reduced ^{19}F background. Samples were packed under an inert atmosphere into 3.2 mm zirconia rotors with reduced ^{19}F top and bottom caps (Phoenix NMR, Colorado, USA). One to three batches of H-SiNPs obtained from separate 1 g etches (1 g of Si/SiO_2 composite) were combined in a rotor at a time such that the total sample volume was *ca.* 30 mg. All spectra were acquired under magic-angle spinning conditions with a spinning frequency ranging between 10 and 20 kHz.

^{19}F MAS NMR spectra were collected using a Hahn-echo pulse sequence with a π/2 pulse length ranging from 2.5 to 5.5 μs, a recycle delay set between 6 and 10 s, and 2,048 coadded transients. ^{29}Si MAS NMR spectra were collected using a 3.5 μs π/2 pulse ($\gamma B_1/2\pi$ = 71 kHz), a recycle delay set to 500 s, and the number of co-added transients set to 128 or 256. ^{29}Si{^{1}H} cross polarization[35] MAS (CPMAS) NMR spectra were collected using a 3.1 μs π/2 pulse on ^{1}H, ramped Hartman-Hahn match on ^{29}Si, a 3 ms contact time, a 4 s recycle delay, TPPM[120] ^{1}H decoupling, and between 600 and 2,048 co-added transients. ^{29}Si{^{19}F} CPMAS NMR spectra were collected using a 2.5 μs π/2 pulse on ^{19}F, ramped Hartman-Hahn match on ^{29}Si, a 3 ms contact time, a recycle delay of 4.5 or 5 s, TPPM ^{19}F decoupling, and between 130,000 and 205,000 co-added transients. Na_2SiF_6 was used as a secondary reference with δ (^{19}F)/ppm = −152 ppm and δ (^{29}Si)/ppm = −189 ppm with respect to $CFCl_3$ (^{19}F, 0 ppm) and TMS (^{29}Si, 0 ppm).[121]

^{23}Na MAS NMR spectra were acquired using Bloch-decay and Hahn-echo pulse sequences for Na_2SiF_6 and 6 nm H-SiNPs, respectively. A 2.5 μs π/2 excitation pulse ($\gamma B_1/2\pi$ = 100 kHz) and a recycle delay of 5 s were used for each experiment, with the number of co-added transients ranging from 16 to 20,000. Solid NaCl was used as a secondary reference with δ (^{23}Na)/ppm = 7.9 ppm [122] with respect to 1M NaCl *(aq)* at δ (^{23}Na) = 0 ppm.

2.5.10 Quantum Chemical Computations

Computations were performed using the Amsterdam Density Functional (ADF) program (version 2019.305).[123–125] To model the surface of H-SiNPs, cluster models were constructed from crystalline silicon (space group = $Fd\bar{3}m$). First, a large cluster of crystalline silicon was generated using the VESTA software.[126] Then, either the Si(100), (111) or (110) lattice planes were visualized depending on the desired surface orientation. After visualization of the desired plane, selected Si atoms were removed to leave the desired face exposed, and the entire model was terminated with hydrogen atoms. The geometry was then optimized using density functional theory (DFT) with the hybrid PBE0 functional[127] and the TZP basis set.[128] All other models were generated by grafting the desired chemical groups (e.g., -F or -SiH_3) onto the exposed face of a hydride-terminated model followed by optimization of the geometry at the same level of theory. To model oxidation, oxygen atoms were first inserted between Si−Si backbonds of an optimized hydride-terminated model. Hydrogen atoms were then added where required and the geometry was optimized at the PBE0/TZP level of theory. Images of all cluster models can be found in **Appendix A**.

Theoretical ^{19}F and ^{29}Si magnetic shielding values were computed with DFT using the hybrid PBE0 functional with a 50% admixture of Hartree-Fock exchange (HFX) and the TZ2P basis set (ZORA/PBE0(50)/TZ2P).[128] It is important to note that the standard PBE0 functional has a 25% admixture of HFX.[127] A 50% admixture of HFX has previously been shown to give the best agreement with experimental ^{19}F shielding values.[129] The zeroth-order regular approximation (ZORA)[130–132] was used to account for scalar relativistic effects. Test calculations including spin-orbit coupling (SOC)[133] were also performed. Although SOC can lead to a small increase in ^{19}F and ^{29}Si shielding relative to the inclusion of scalar relativistic effects alone (**Table A3**), any differences cancel out when shielding is converted to chemical shift. To further assess the chosen level of theory, ^{19}F, and ^{29}Si shielding values were computed for SiF_4 and compared to the experimental values.[134–136] **Table A4** shows that the computed shielding constants with 50% HFX agree very well with the experimental values. The theoretical ^{29}Si shielding is nearly identical to the experimental value.

Theoretical shielding values (σ) were converted to chemical shifts (δ) using the cubic K_2SiF_6 compound (space group = $Fm\overline{3}m$) as a reference by the relationships

$$\boldsymbol{\delta}_{calc}^{model}(^{19}F)/ppm = \left(\boldsymbol{\sigma}_{calc}^{K_2SiF_6} - \mathbf{135}\ ppm\right) - \boldsymbol{\sigma}_{calc}^{model}$$

$$\boldsymbol{\delta}_{calc}^{model}(^{29}Si)/ppm = \left(\boldsymbol{\sigma}_{calc}^{K_2SiF_6} - \mathbf{184}\ ppm\right) - \boldsymbol{\sigma}_{calc}^{model}$$

where −135 and −184 ppm are the experimental ^{19}F and ^{29}Si chemical shifts of K_2SiF_6, respectively (**Figure A12**). The values of $\boldsymbol{\sigma}_{calc}^{K_2SiF_6}$ for ^{19}F and ^{29}Si are 328 and 553 ppm, respectively, and were obtained from NMR calculations for a $[K_8SiF_6]$ cluster performed at the ZORA/PBE0(50)/TZ2P level of theory.

Chapter 3. Future Work

3.1 Heteronuclear Correlation (HETCOR) Spectroscopy and ^{19}F-Detected Methods

This thesis has provided a structural model for fluorinated species on the surface of H-SiNPs. However, future work exploiting more advanced NMR methods could enable this model to be improved. For example, initial attempts of ^{29}Si{^{19}F} HETCOR were unsuccessful in this study due to the poor sensitivity imparted by the low fluorine content (<0.5%) and relatively low natural abundance of ^{29}Si (4.7%). This area may benefit from high-sensitivity techniques such as high-field dynamic nuclear polarization (DNP) or fast MAS ^{19}F-detected NMR methods. High-field DNP and fast MAS would provide improved sensitivity and resolution that could enable particular (O/F)−Si species to be distinguished.[137–140] Similarly, ^{19}F-detection may provide additional filtering of the ^{19}F dimension in a fashion analogous to ^{1}H-detection in biomolecular solids.[141–145]

Finally, sensitivity enhancements could be obtained by direct fluorination of H-SiNPs with XeF_2. Alkyl functionality can be attached to SiNPs using XeF_2;[116] however, direct treatment of H-SiNPs with this compound could increase the fluorine content on the surface and provide the required sensitivity boost for successful ^{29}Si{^{19}F} HETCOR experiments.

3.2 SiNPs as Multimodal Medical Imaging Agents

An extension of the work in this thesis is to selectively label SiNPs with a fluorinated ligand for ^{19}F MRI applications. There is no ^{19}F background signal in biological systems, which makes the development of ^{19}F MRI contrast agents an area of substantial interest.[74,146,147] The tailorable surface chemistry and biocompatibility of SiNPs means that they are excellent candidates for this application; a fluorinated tag can be attached to the surface of SiNPs using well-established hydrosilylation methods.[39] Furthermore, tissue-specific targeting of the nanoparticles may be possible via size exclusion and careful design of the fluorinated tag.

Multimodal medical imaging is also a possibility. For example, partial exchange of ^{19}F for ^{18}F on a fluorinated ligand may enable ^{19}F MRI to be used in conjunction with positron emission tomography (PET). This could provide unprecedented insight into diseases that include concurrent structural and metabolic changes (e.g., many cancers). Due to the world-class NMR, MRI, and cyclotron facilities at the University of Alberta, these research directions are uniquely addressable at this institution.

References

(1) Rabi, I. I.; Zacharias, J. R.; Millman, S.; Kusch, P. A New Method of Measuring Nuclear Magnetic Moment. *Phys. Rev.* **1938**, *53*, 318.

(2) Reif, B.; Ashbrook, S. E.; Emsley, L.; Hong, M. Solid-state NMR spectroscopy. *Nat. Rev. Methods Primers* **2021**, *1*, 2.

(3) Levitt, M. *Spin Dynamics*, 2nd ed.; Wiley: New York, 2008.

(4) Kuprov, I. *Spin: From Basic Symmetries to Quantum Optimal Control*; Springer International Publishing, 2023.

(5) Born, M.; Oppenheimer, R. Zur Quantentheorie Der Molekeln. *Ann. Phys.* **1927**, *389*, 457–484.

(6) Van Den Heuvel, W.; Soncini, A. NMR Chemical Shift as Analytical Derivative of the Helmholtz Free Energy. *J. Chem. Phys.* **2013**, *138* (5).

(7) Helgaker, T.; Jaszuński, M.; Ruud, K. Ab Initio Methods for the Calculation of NMR Shielding and Indirect Spin-Spin Coupling Constants. *Chem. Rev.* **1999**, *99* (1), 293–352.

(8) Kaupp, M.; Buhl, M.; Malkin, V. G. *Calculation of NMR and EPR Parameters: Theory and Applications*; Wiley, 2004.

(9) Autschbach, J.; Ziegler, T. Relativistic Computation of NMR Shieldings and Spin-Spin Coupling Constants. In *Encyclopedia of Nuclear Magnetic Resonance: Advances in NMR*, 1st ed.; Wiley, 2002.

(10) Autschbach, J.; Ziegler, T. Double Perturbation Theory: A Powerful Tool in Computational Coordination Chemistry. *Coord. Chem. Rev*. **2003**, *238–239*,83–126.

(11) Rusakova, I.L. Quantum Chemical Approaches to the Calculation of NMR Parameters: From Fundamentals to Recent Advances. *Magnetochemistry* **2022**, *8*, 50.

(12) Ditchfield, R. Self-Consistent Perturbation Theory of Diamagnetism I. A Gauge-Invariant LCAO Method for N.M.R. Chemical Shifts. *Mol. Phys.* **1974**, *27* (4), 789–807.

(13) Pople, J. A.; McIver, J. W.; Ostlund, N. S. Self-Consistent Perturbation Theory. I. Finite Perturbation Methods. *J. Chem. Phys.* **1968**, *49* (7), 2960–2964.

(14) Guttinger, P. Das Verhalten von Atomen Im Magnetischen Drehfeld. *Z. Phys.* **1931**, *73*, 169–184.

(15) Farrar, T. C. Density Matrices in NMR Spectroscopy: Part I. *Concepts Magn. Reson.* **1990**, *2* (1), 1–12.

(16) Chen, B. The Density Matrix and Its Basic Applications in NMR. In *Fundamentals of Recoupling and Decoupling Techniques in Solid State NMR*; AIP Publishing, 2021.

(17) Anet, F. A. L.; O'leary, D. J. The Shielding Tensor Part I: Understanding Its Symmetry Properties. *Concepts Magn. Reson.* **1991**, *3* (1), 193–214.

(18) Smith, S. A.; Palke, W. E.; Gerig, J. T. The Hamiltonians of NMR. Part I. *Concepts Magn. Reson.* **1992**, *4* (2), 107–144.

(19) Facelli, J. C. Chemical Shift Tensors: Theory and Application to Molecular Structural Problems. *Prog. Nucl. Magn. Reson. Spectrosc.* **2011**, *3–4*, 176–201.

(20) Ramsey, N. F. Magnetic Shielding of Nuclei in Molecules. *Phys. Rev.* **1950**, *78* (6), 699–703.

(21) Widdifield, C. M.; Schurko, R. W. Understanding Chemical Shielding Tensors Using Group Theory, MO Analysis, and Modern Density-Functional Theory. *Concepts Magn. Reson. Part A Bridg. Educ. Res.* **2009**, *34* (2), 91–123.

(22) Kaupp, M. Relativistic Effects on NMR Chemical Shifts. In *Theoretical and Computational Chemistry*; Schwerdtfeger, P., Ed.; Elsevier: Amsterdam, 2004; Vol. 14, pp 552−597.

(23) Kaupp, M.; Malkina, O. L.; Malkin, V. G.; Pyykkö, P. How Do Spin-Orbit-Induced Heavy-Atom Effects on Nmr Chemical Shifts Function? Validation of a Simple Analogy to Spin-Spin Coupling by Density Functional Theory (DFT) Calculations on Some Iodo Compounds. *Chem. Eur. J.* **1998**, *4* (1), 118–126.

(24) Vĺcha, J.; Novotný, J.; Komorovsky, S.; Straka, M.; Kaupp, M.; Marek, R. Relativistic Heavy-Neighbor-Atom Effects on NMR Shifts: Concepts and Trends across the Periodic Table. *Chem. Rev*. **2020**, *120*, 7065–7103.

(25) Mason, J. Conventions for the Reporting of Nuclear Magnetic Shielding (or Shift) Tensors Suggested by Participants in the NATO ARW on NMR Shielding Constants at the University of Maryland, College Park, July 1992. *Solid State Nucl. Magn. Reson.* **1993**, *2*, 285–288.

(26) Le Guennic, B.; Autschbach, J. Analyzing and Interpreting NMR Spin-Spin Coupling Constants Using Molecular Orbital Calculations. *J. Chem. Educ.* **2007**, *84*, 156–171.

(27) Wasylishen, R. E. Dipolar and Indirect Coupling Tensors in Solids. In *Encyclopedia of Nuclear Magnetic Resonance*; Wiley, 2007.

(28) Wasylishen, R. E. Dipolar and Indirect Coupling: Basics. In *Encyclopedia of Nuclear Magnetic Resonance*; Wiley, 2007.

(29) Hohenberg, P.; Kohn, W. Inhomogeneous Electron Gas. *Phys. Rev.* **1964**, *136*, 864–871.

(30) Kohn, W.; Sham, L. J. Self-Consistent Equations Including Exchange and Correlation Effects. *Phys. Rev.* **1965**, *140*, 1133–1138.

(31) Schreckenbach, G.; Ziegler, T. Calculation of NMR Shielding Tensors Using Gauge-Including Atomic Orbitals and Modern Density Functional Theory. *J. Phys. Chem.* **1995**, *99* (2), 606– 611.

(32) Schreckenbach, G.; Ziegler, T. Density Functional Calculations of NMR Chemical shifts and ESR G-Tensor. *Theor. Chem. Acc.* **1998**, *99*, 71–82.

(33) Wolff, S. K.; Ziegler, T.; Van Lenthe, E.; Baerends, E. J. Density Functional Calculations of Nuclear Magnetic Shieldings Using the Zeroth-Order Regular Approximation (ZORA) for Relativistic Effects: ZORA Nuclear Magnetic Resonance. *J. Chem. Phys.* **1999**, *110* (16), 7689–7698.

(34) Wolff, S. K.; Ziegler, T. Calculation of DFT-GIAO NMR Shifts with the Inclusion of Spin-Orbit Coupling. *J. Chem. Phys.* **1998**, *109* (3), 895–905.

(35) Pines, A.; Gibby, M. G.; Waugh, J. S. Proton-Enhanced Nuclear Induction Spectroscopy: a Method for High Resolution NMR of Dilute Spins in Solids. *J. Chem. Phys*. **1972**, 1776–1777.

(36) Harris, R. K.; Becker, E. D.; de Menrzes, S. M. C.; Goodfellow, R.; Granger, P. NMR Nomenclature. Nuclear Spin Properties and Conventions for Chemical Shifts. *Pure Appl. Chem*. **2001**, *73*, 1795–1818.

(37) Thiessen, A. N.; Ha, M.; Hooper, R. W.; Yu, H.; Oliynyk, A. O.; Veinot, J. G. C.; Michaelis, V. K. Silicon Nanoparticles: Are They Crystalline from the Core to the Surface? *Chem. Mater.* **2019**, *31* (3), 678–688.

(38) Ha, M.; Thiessen, A. N.; Sergeyev, I. V.; Veinot, J. G. C.; Michaelis, V. K. Endogenous Dynamic Nuclear Polarization NMR of Hydride-Terminated Silicon Nanoparticles. *Solid State Nucl. Magn. Reson.* **2019**, *100*, 77–84.

(39) Clark, R. J.; Aghajamali, M.; Gonzalez, C. M.; Hadidi, L.; Islam, M. A.; Javadi, M.; Mobarok, M. H.; Purkait, T. K.; Robidillo, C. J. T.; Sinelnikov, R.; Thiessen, A. N.;

Washington, J.; Yu, H.; Veinot, J. G. C. From Hydrogen Silsesquioxane to Functionalized Silicon Nanocrystals. *Chem. Mater.* **2017**, *29* (1), 80–89.

(40) Dasog, M.; Yang, Z.; Regli, S.; Atkins, T. M.; Faramus, A.; Singh, M. P.; Muthuswamy, E.; Kauzlarich, S. M.; Tilley, R. D.; Veinot, J. G. C. Chemical Insight into the Origin of Red and Blue Photoluminescence Arising from Freestanding Silicon Nanocrystals. *ACS Nano* **2013**, *7* (3), 2676–2685.

(41) Cheong, I. T.; Yang Szepesvari, L. Y.; Ni, C.; Butler, C.; O'Connor, K. M.; Hooper, R.; Meldrum, A.; Veinot, J. G. C. Not All Silicon Quantum Dots Are Equal: Photostability of Silicon Quantum Dots with and without a Thick Amorphous Shell. *Nanoscale* **2024**, *16*, 592–603.

(42) Thiessen, A. N.; Zhang, L.; Oliynyk, A. O.; Yu, H.; O'Connor, K. M.; Meldrum, A.; Veinot, J. G. C. A Tale of Seemingly "Identical" Silicon Quantum Dot Families: Structural Insight into Silicon Quantum Dot Photoluminescence. *Chem. Mater.* **2020**, *32* (16), 6838–6846.

(43) Dasog, M.; De Los Reyes, G. B.; Titova, L. V.; Hegmann, F. A.; Veinot, J. G. C. Size vs Surface: Tuning the Photoluminescence of Freestanding Silicon Nanocrystals Across the Visible Spectrum via Surface Groups. *ACS Nano* **2014**, *8* (9), 9636–9648.

(44) Sinelnikov, R.; Dasog, M.; Beamish, J.; Meldrum, A.; Veinot, J. G. C. Revisiting an Ongoing Debate: What Role Do Surface Groups Play in Silicon Nanocrystal Photoluminescence? *ACS Photonics* **2017**, *4* (8), 1920–1929.

(45) Dasog, M.; Bader, K.; Veinot, J. G. C. Influence of Halides on the Optical Properties of Silicon Quantum Dots. *Chem. Mater.* **2015**, *27* (4), 1153–1156.

(46) Anthony, R.; Kortshagen, U. Photoluminescence Quantum Yields of Amorphous and Crystalline Silicon Nanoparticles. *Phys. Rev. B* **2009**, *80* (11).

(47) Jurbergs, D.; Rogojina, E.; Mangolini, L.; Kortshagen, U. Silicon Nanocrystals with Ensemble Quantum Yields Exceeding 60%. *Appl. Phys. Lett.* **2006**, *88* (23).

(48) Kortshagen, U. R.; Sankaran, R. M.; Pereira, R. N.; Girshick, S. L.; Wu, J. J.; Aydil, E. S. Nonthermal Plasma Synthesis of Nanocrystals: Fundamental Principles, Materials, and Applications. *Chem. Rev*. **2016**, *116*,11061–11127.

(49) Bhattacharjee, S.; Rietjens, I. M. C. M.; Singh, M. P.; Atkins, T. M.; Purkait, T. K.; Xu, Z.; Regli, S.; Shukaliak, A.; Clark, R. J.; Mitchell, B. S.; Alink, G. M.; Marcelis, A. T. M.; Fink, M. J.; Veinot, J. G. C.; Kauzlarich, S. M.; Zuilhof, H. Cytotoxicity of Surface-

Functionalized Silicon and Germanium Nanoparticles: The Dominant Role of Surface Charges. *Nanoscale* **2013**, *5* (11), 4870–4883.

(50) Islam, M. A.; Sinelnikov, R.; Howlader, M. A.; Faramus, A.; Veinot, J. G. C. Mixed Surface Chemistry: An Approach to Highly Luminescent Biocompatible Amphiphilic Silicon Nanocrystals. *Chem. Mater.* **2018**, *30* (24), 8925–8931.

(51) Erogbogbo, F.; Yong, K. T.; Roy, I.; Hu, R.; Law, W. C.; Zhao, W.; Ding, H.; Wu, F.; Kumar, R.; Swihart, M. T.; Prasad, P. N. In Vivo Targeted Cancer Imaging, Sentinel Lymph Node Mapping and Multi-Channel Imaging with Biocompatible Silicon Nanocrystals. *ACS Nano* **2011**, *5* (1), 413–423.

(52) O'Connor, K. M.; Rubletz, A.; Trach, J.; Butler, C.; Veinot, J. G. C. Understanding Silicon Monoxide Gas Evolution from Mixed Silicon and Silica Powders. *Nanoscale Horiz.* **2023**, *8* (7), 892–899.

(53) Hessel, C. M.; Henderson, E. J.; Veinot, J. G. C. Hydrogen Silsesquioxane: A Molecular Precursor for Nanocrystalline Si-SiO_2 Composites and Freestanding Hydride-Surface-Terminated Silicon Nanoparticles. *Chem. Mater.* **2006**, *18* (26), 6139–6146.

(54) O'Connor, K. M.; Rubletz, A.; Ni, C.; He, Y.; Butler, C.; Veinot, J. G. C. High-Temperature Anomaly in the Synthesis of Large (d > 100 nm) Silicon Nanoparticles from Hydrogen Silsesquioxane. *Chem. Mater.* **2023**, *35*, 7967–7973.

(55) Islam, M. A.; Purkait, T. K.; Veinot, J. G. C. Chloride Surface Terminated Silicon Nanocrystal Mediated Synthesis of Poly(3-Hexylthiophene). *J. Am. Chem. Soc.* **2014**, *136* (43), 15130–15133.

(56) Yang, Z.; Iqbal, M.; Dobbie, A. R.; Veinot, J. G. C. Surface-Induced Alkene Oligomerization: Does Thermal Hydrosilylation Really Lead to Monolayer Protected Silicon Nanocrystals? *J. Am. Chem. Soc.* **2013**, *135* (46), 17595–17601.

(57) Hanrahan, M. P.; Fought, E. L.; Windus, T. L.; Wheeler, L. M.; Anderson, N. C.; Neale, N. R.; Rossini, A. J. Characterization of Silicon Nanocrystal Surfaces by Multidimensional Solid-State NMR Spectroscopy. *Chem. Mater.* **2017**, *29* (24), 10339–10351.

(58) Wheeler, L. M.; Neale, N. R.; Chen, T.; Kortshagen, U. R. Hypervalent Surface Interactions for Colloidal Stability and Doping of Silicon Nanocrystals. *Nat. Commun.* **2013**, *4*.

(59) Cheong, I. T.; Mock, J.; Kallergi, M.; Groß, E.; Meldrum, A.; Rieger, B.; Becherer, M.; Veinot, J. G. C. Colloidal Silicon Quantum Dot-Based Cavity Light-Emitting Diodes with Narrowed and Tunable Electroluminescence. *Adv. Opt. Mater.* **2023**, *11* (1).

(60) Ono, T.; Xu, Y.; Sakata, T.; Saitow, K. I. Designing Efficient Si Quantum Dots and LEDs by Quantifying Ligand Effects. *ACS Appl. Mater. Interfaces* **2022**, *14* (1), 1373–1388.

(61) Dutta, M.; Thirugnanam, L.; Trinh, P. Van; Fukata, N. High Efficiency Hybrid Solar Cells Using Nanocrystalline Si Quantum Dots and Si Nanowires. *ACS Nano* **2015**, *9* (7), 6891–6899.

(62) Švrček, V.; McDonald, C.; Lozac'h, M.; Tayagaki, T.; Koganezawa, T.; Miyadera, T.; Mariotti, D.; Matsubara, K. Stable Ultrathin Surfactant-Free Surface-Engineered Silicon Nanocrystal Solar Cells Deposited at Room Temperature. *Energy Sci. Eng.* **2017**, *5* (4), 184–193.

(63) Gonzalez, C. M.; Veinot, J. G. C. Silicon Nanocrystals for the Development of Sensing Platforms. *J. Mater. Chem. C.* **2016**, *4*, 4836–4846.

(64) Tu, C.; Ma, X.; House, A.; Kauzlarich, S. M.; Louie, A. Y. PET Imaging and Biodistribution of Silicon Quantum Dots in Mice. *ACS Med. Chem. Lett.* **2011**, *2* (4), 285–288.

(65) Kim, J.; Jo, D.; Yang, S. H.; Joo, C. G.; Whiting, N.; Pudakalakatti, S.; Seo, H.; Son, H. Y.; Min, S. J.; Bhattacharya, P.; Huh, Y. M.; Shim, J. H.; Lee, Y. ^{29}Si Isotope-Enriched Silicon Nanoparticles for an Efficient Hyperpolarized Magnetic Resonance Imaging Probe. *ACS Appl. Mater. Interfaces* **2021**, *13* (48), 56923–56930.

(66) Liu, J.; Erogbogbo, F.; Yong, K. T.; Ye, L.; Liu, J.; Hu, R.; Chen, H.; Hu, Y.; Yang, Y.; Yang, J.; Roy, I.; Karker, N. A.; Swihart, M. T.; Prasad, P. N. Assessing Clinical Prospects of Silicon Quantum Dots: Studies in Mice and Monkeys. *ACS Nano* **2013**, *7* (8), 7303–7310.

(67) Kovalev, D.; Heckler, H.; Ben-Chorin, M.; Polisski, G.; Schwartzkopff, M.; Koch, F. Breakdown of the K-Conservation Rule in Si Nanocrystals. *Phys. Rev. Lett.* **1998**, *81*, 2803–2806.

(68) Guan, M.; Wang, W.; Henderson, E. J.; Dag, Ö.; Kübel, C.; Chakravadhanula, V. S. K.; Rinck, J.; Moudrakovski, I. L.; Thomson, J.; McDowell, J.; Powell, A. K.; Zhang, H.; Ozin, G. A. Assembling Photoluminescent Silicon Nanocrystals into Periodic Mesoporous Organosilica. *J. Am. Chem. Soc.* **2012**, *134* (20), 8439–8446.

(69) Stacy, B. J.; Shah, S. V.; De Gorostiza, A.; Ngo, L.; Korgel, B. A. Size-Dependent Room-Temperature Hydrosilylation of Silicon Nanocrystals without UV Light Excitation. *ACS Mater. Lett.* **2023**, 73–80.

(70) Zhukhovitskiy, A. V.; Mavros, M. G.; Queeney, K. T.; Wu, T.; Voorhis, T. Van; Johnson, J. A. Reactions of Persistent Carbenes with Hydrogen-Terminated Silicon Surfaces. *J. Am. Chem. Soc.* **2016**, *138* (27), 8639–8652.

(71) Sangghaleh, F.; Sychugov, I.; Yang, Z.; Veinot, J. G. C.; Linnros, J. Near-Unity Internal Quantum Efficiency of Luminescent Silicon Nanocrystals with Ligand Passivation. *ACS Nano* **2015**, *9* (7), 7097–7104.

(72) Shirahata, N.; Nakamura, J.; Inoue, J. I.; Ghosh, B.; Nemoto, K.; Nemoto, Y.; Takeguchi, M.; Masuda, Y.; Tanaka, M.; Ozin, G. A. Emerging Atomic Energy Levels in Zero-Dimensional Silicon Quantum Dots. *Nano Lett.* **2020**, *20* (3), 1491–1498.

(73) Han, X.; Xu, K.; Taratula, O.; Farsad, K. Applications of Nanoparticles in Biomedical Imaging. *Nanoscale*. **2019**, *11*, 799–819.

(74) Joseph, J. M.; Gigliobianco, M. R.; Firouzabadi, B. M.; Censi, R.; Di Martino, P. Nanotechnology as a Versatile Tool For^{19}F-MRI Agent's Formulation: A Glimpse into the Use of Perfluorinated and Fluorinated Compounds in Nanoparticles. *Pharmaceutics* **2022**, *14* (2), 382.

(75) Arango, J. M.; Padro, D.; Blanco, J.; Lopez-Fernandez, S.; Castellnou, P.; Villa-Valverde, P.; Ruiz-Cabello, J.; Martin, A.; Carril, M. Fluorine Labeling of Nanoparticles and in vivo ^{19}F Magnetic Resonance Imaging. *ACS Appl. Mater. Interfaces* **2021**, *13* (11), 12941–12949.

(76) Nijiati, S.; Zeng, F.; Zuo, C.; Zhang, Q.; Du, C.; Shi, C.; Gao, J.; Zhou, Z. Fe(II)-Targeted PET/^{19}F MRI Dual-Modal Molecular Imaging Probe for Early Evaluation of Anticancer Drug-Induced Acute Kidney Injury. *Mol. Pharm.* **2023**, *20* (10), 5185–5194.

(77) Rupich, S. M.; Chabal, Y. J. Surface Chemical Composition and Morphology. In *Handbook of Silicon Wafer Cleaning Technology*; Elsevier Inc., 2018; pp 505–577.

(78) Knotter, D. M. Etching Mechanism of Vitreous Silicon Dioxide in HF-Based Solutions. *J. Am. Chem. Soc.* **2000**, *122* (18), 4345–4351.

(79) Verhaverbeke, S.; Teerlinck, I.; Vinckier, C.; Stevens, R.; Cartuyvels, R.; Heyns, M. M. The Etching Mechanisms of SiO_2 in Hydrofluoric Acid. *J. Electrochem. Soc.* **1994**, *141*, 2852–2856.

(80) Trucks, G. W.; Raghavachari, K.; Higashi, G. S.; Chabal, Y. J. Mechanism of HF Etching of Silicon Surfaces: A Theoretical Understanding of Hydrogen Passivation. *Phys. Rev. Lett.* **1990**, *65*, 504– 507.

(81) H. Ubara, T. Imura, A. Hiraki, Formation of SiH Bonds on the Surface of Microcrystalline Silicon Covered with SiO_x by HF treatment. *Solid State Commun.* **1984**, *50*, 673–675.

(82) Yablonovitch, E.; Allara, D. L.; Chang, C. C.; Gmitter, T.; Bright, T. B. Unusually Low Surface-Recombination Velocity on Silicon and Germanium Surfaces. *Phys. Rev. Lett.* **1986**, *57*, 249– 252.

(83) Michalak, D. J.; Amy, S. R.; Aureau, D.; Dai, M.; Estève, A.; Chabal, Y. J. Nanopatterning Si(111) Surfaces as a Selective Surface-Chemistry Route. *Nat. Mater.* **2010**, *9* (3), 266–271.

(84) Skibinski, E. S.; Debenedetti, W. J. I.; Rupich, S. M.; Chabal, Y. J.; Hines, M. A. Frustrated Etching During H/Si(111) Methoxylation Produces Fissured Fluorinated Surfaces, Whereas Direct Fluorination Preserves the Atomically Flat Morphology. *J. Phys. Chem. C* **2015**, *119* (46), 26029–26037.

(85) Glockzin, B.; Oakley, M. S.; Karmakar, A.; Pominov, A.; Mitchell, A. A.; Ma, X.; Klobukowski, M.; Michaelis, V. K. Alkali Tin Halides: Exploring the Local Structure of A_2SnX_6 (A = K, Rb; X = Cl, Br, I) Compounds Using Solid-State NMR and DFT Computations. *J. Phys. Chem. C* **2023**, *127* (15), 7284–7298.

(86) Hooper, R. W.; Sarkar, D.; Michaelis, V. K. Bulk and Nanoscale Semiconducting Materials: Structural Advances Using Solid-State NMR Spectroscopy. *Curr. Opin. Colloid Interface Sci.* **2022**, *62*, 101631.

(87) Lee, D.; Kaushik, M.; Coustel, R.; Chenavier, Y.; Chanal, M.; Bardet, M.; Dubois, L.; Okuno, H.; Rochat, N.; Duclairoir, F.; Mouesca, J. M.; De Paëpe, G. Solid-State NMR and DFT Combined for the Surface Study of Functionalized Silicon Nanoparticles. *Chem. Eur. Jour.* **2015**, *21* (45), 16047–16058.

(88) Faulkner, R. A.; DiVerdi, J. A.; Yang, Y.; Kobayashi, T.; Maciel, G. E. The Surface of Nanoparticle Silicon as Studied by Solid-State NMR. *Materials* **2013**, *6* (1), 18–46.

(89) Dorn, R. W.; Ryan, B. J.; Lamahewage, S. N. S.; Dodson, M. V.; Essner, J. B.; Biswas, R.; Panthani, M. G.; Rossini, A. J. Chlorination of Hydrogenated Silicon Nanosheets Revealed by Solid-State Nuclear Magnetic Resonance Spectroscopy. *Chem. Mater.* **2022**, *2*, 539–548.

(90) Ryan, B. J.; Hanrahan, M. P.; Wang, Y.; Ramesh, U.; Nyamekye, C. K. A.; Nelson, R. D.; Liu, Z.; Huang, C.; Whitehead, B.; Wang, J.; Roling, L. T.; Smith, E. A.; Rossini, A. J.; Panthani, M. G. Silicene, Siloxene, or Silicane? Revealing the Structure and Optical Properties of Silicon Nanosheets Derived from Calcium Disilicide. *Chem. Mater.* **2020**, *32* (2), 795–804.

(91) McDonald, R. S. Surface Functionality of Amorphous Silica by Infrared Spectroscopy. *J. Phys. Chem.* **1958**, *62* (10), 1168– 1178.

(92) Luhmer, M.; d'Espinose, J. B.; Hommel, H.; Legrand, A. P. High-Resolution ^{29}Si Solid-state NMR Study of Silicon Functionality Distribution on the Surface of Silicas. *Magn. Reson. Imaging* **1996**, *14* (7–8), 911– 913.

(93) Hartmeyer, G.; Marichal, C.; Lebeau, B.; Caullet, P.; Hernandez, J. Fluorination of Silica Nanoparticles by Aqueous NH_4F Solutions. *J. Phys. Chem. C* **2007**, *111* (18), 6634–6644.

(94) Youngman, R. E.; Sen, S. The Nature of Fluorine in Amorphous Silica. *J. Non. Cryst. Solids* **2004**, *337* (2), 182–186.

(95) Youngman, R. E.; Sen, S. Structural Role of Fluorine in Amorphous Silica. *J. Non. Cryst. Solids*; **2004**, *349*, 10–15.

(96) Ashbrook, S. E.; Berry, A. J.; Frost, D. J.; Gregorovic, A.; Pickard, C. J.; Readman, J. E.; Wimperis, S. ^{17}O and ^{29}Si NMR Parameters of $MgSiO_3$ Phases from High-Resolution Solid-State NMR Spectroscopy and First-Principles Calculations. *J. Am. Chem. Soc.* **2007**, *129* (43), 13213–13224.

(97) Lataste, E.; Legein, C.; Body, M.; Buzaré, J. Y.; Tressaud, A.; Demourgues, A. Highly Fluorinated Silica Obtained by Direct F_2-Gas Fluorination: Stability and Unprecedented Fluorosilicate Species Revealed by Solid State NMR Investigation. *J. Phys. Chem. C* **2009**, *113* (43), 18652–18660.

(98) Buriak, J. M. Organometallic Chemistry on Silicon and Germanium Surfaces. *Chem. Rev.* **2002**, *102* (5), 1271–1308.

(99) Duncan, T. M.; Douglass, D. C.; Csencsits, R.; Walker, K. L. Study of Fluorine in Silicate Glass with ^{19}F Nuclear Magnetic Resonance Spectroscopy. *J. Appl. Phys.* **1986**, *60* (1), 130–136.

(100) Hosono, H.; Mizuguchi, M.; Skuja, L. Fluorine-Doped SiO_2 Glasses for F_2 Excimer Laser Optics: Fluorine Content and Color-Center Formation. *Opt. Lett.* **1999**, *24*, 1549–1551.

(101) Kasi, S. R.; Liehr, M.; Cohen, S. Chemistry of Fluorine in the Oxidation of Silicon. *Appl. Phys. Lett.* **1991**, *58* (25), 2975–2977.

(102) Nishioka, Y.; Ohji, Y.; Mukai, K.; Sugano, T.; Wang, Y.; Ma, T. P. Dielectric Characteristics of Fluorinated Ultradry SiO_2. *Appl. Phys. Lett.* **1989**, *54* (12), 1127–1129.

(103) Ting, W.; Lo, G. Q.; Hsieh, T. Y.; Kwong, D. L.; Kuehne, J.; Magee, C. W. Fluorinated Thin SiO_2 Grown by Rapid Thermal Processing. *Appl. Phys. Lett.* **1990**, *56* (22), 2255–2257.

(104) Zhang, W.; Jing, Q.; Fang, Y.; Chen, Z. Synthesis, Structure, and Properties of Nonlinear Optical Crystal Na_2SiF_6. *Z. Anorg. Allg. Chem.* **2017**, *643* (22), 1739–1743.

(105) Iliescu, C.; Tay, F. E. H.; Miao, J. Strategies in Deep Wet Etching of Pyrex Glass. *Sens. Actuators A Phys.* **2007**, *133*, 395–400.

(106) Smedskjaer, M. M.; Youngman, R. E.; Mauro, J. C. Principles of Pyrex® Glass Chemistry: Structure-Property Relationships. *Appl. Phys. A Mater. Sci. Process* **2014**, *116* (2), 491–504.

(107) Frayret, J.; Castetbon, A.; Trouve, G.; Potin-Gautier, M. Solubility of $(NH_4)_2SiF_6$, K_2SiF_6 and Na_2SiF_6 in Acidic Solutions. *Chem. Phys. Lett.* **2006**, *427*, 356–364.

(108) Dahanayake, J. N.; Kasireddy, C.; Karnes, J. P.; Verma, R.; Steinert, R. M.; Hildebrandt, D.; Hull, O. A.; Ellis J. M.; Mitchell-Koch, K. R. Progress in our Understanding of ^{19}F Chemical Shifts. *Annu. Reports NMR Spectrosc.*, 2018, **93**, 281–365.

(109) Kiczenski, T. J.; Stebbins, J. F. Fluorine Sites in Calcium and Barium Oxyfluorides: F-19 NMR on Crystalline Model Compounds and Glasses. *J. Non. Cryst. Solids* **2002**, *306*, 160–168.

(110) Martell, S. A.; Werner-Zwanziger, U.; Dasog, M. The Influence of Hydrofluoric Acid Etching Processes on the Photocatalytic Hydrogen Evolution Reaction Using Mesoporous Silicon Nanoparticles. *Faraday Discuss.* **2020**, *222*, 176–189.

(111) Bansal, A.; Li, X.; Lauermann, I.; Lewis, N. S.; Yi, S. I.; Weinberg, W. H. Alkylation of Si Surfaces Using a Two-Step/Grignard Route. *J. Am. Chem. Soc.* **1996**, *35* (4), 7225–7226.

(112) Duer, M. J. Shielding and Chemical Shift. In *Solid-State NMR Spectroscopy Principles and Applications*; Wiley, 2001; pp 216–236.

(113) Kaupp, M. Interpretation of NMR Chemical Shifts. In *Calculation of NMR and EPR Parameters*; 2004.

(114) Schreckenbach, G.; Ziegler, T. Calculation of NMR Shielding Tensors Using Gauge-Including Atomic Orbitals and Modern Density Functional Theory. *J. Phys. Chem.* **1995**, *99*, 606–611.

(115) Ruiz-Morales, Y.; Schreckenbach, G.; Ziegler, T. Theoretical Study of ^{13}C and ^{17}O NMR Shielding Tensors in Transition Metal Carbonyls Based on Density Functional Theory and Gauge-Including Atomic Orbitals. *J. Phys. Chem. A* **1996**, *100*, 3359– 3367.

(116) Mobarok, M. H.; Purkait, T. K.; Islam, M. A.; Miskolzie, M.; Veinot, J. G. C. Instantaneous Functionalization of Chemically Etched Silicon Nanocrystal Surfaces. *Angew. Chem. Int. Ed.* **2017**, *56* (22), 6073–6077.

(117) Burrows, V. A.; Yota, J. A Surface IR Study of Inorganic Film Formation GaAs, Silicon and Germanium by Aqueous NH_4F, and HF. *Thin Solid Films* **1990**, *193−194*, 371.

(118) Frye, C. L.; Collins, W. T. The Oligomeric Silsesquioxanes, $(HSiO_{3/2})_n$. *J. Am. Chem. Soc.* **1970**, *92*, 5586–5588.

(119) Langford, J. I.; Wilson, A. J. C. Scherrer After Sixty Years: A Survey and Some New Results in the Determination of Crystallite Size. *J. Appl. Crystallogr.* **1978**, *11* (2), 102–113.

(120) Bennett, A. E.; Rienstra, C. M.; Auger, M.; Lakshmi, K. V.; Griffin, R. G. Heteronuclear Decoupling in Rotating Solids. *J. Chem. Phys.* **1995**, *103* (16), 6951–6958.

(121) Hoffner, F. M.; Delmotte, L.; Kessler, H. A $^{19}F/^{29}Si$ CP MAS n.m.r, Study of Microporous Solids Synthesized in Fluoride Medium. *Zeolites* **1993**, *13*, 60–63.

(122) Tabeta, R.; Saito, H. ^{23}Na Chemical Shifts of Some Inorganic and Organic Compounds in the Solid State as Determined by the Magic Angle Spinning and High Power NMR Methods. *Chem. Lett.* **1984**, *13*, 293–296.

(123) te Velde, G.; Bickelhaupt, F. M.; Baerends, E. J.; Fonseca Guerra, C.; van Gisbergen, S. J. A.; Snijders, J. G.; Ziegler, T. Chemistry with ADF. *J. Comput. Chem.* **2001**, *22* (9), 931–967.

(124) Fonseca Guerra, C.; Snijders, J. G.; Te Velde, G.; Baerends, E. J. Towards an Order-N DFT Method. *Theor. Chem. Acc.* **1998**, *99* (6), 391–403.

(125) Baerends, E. J.; Ziegler, T.; Atkins, A. J.; Autschbach, J.; Baseggio, O.; Bashford, D.; Bérces, A.; Bickelhaupt, F. M.; Bo, C.; Boerrigter, P. M.; et al. *ADF2018, SCM, Theoretical Chemistry*; Vrije Universiteit: Amsterdam, The Netherlands.

(126) Momma, K.; Izumi, F. VESTA 3 for Three-Dimensional Visualization of Crystal, Volumetric and Morphology Data. *J. Appl. Crystallogr.* **2011**, *44* (6), 1272–1276.

(127) Adamo, C.; Barone, V. Toward Reliable Density Functional Methods without Adjustable Parameters: The PBE0 Model. *J. Chem. Phys.* **1999**, *110* (13), 6158–6170.

(128) Van Lenthe, E.; Baerends, E. J. Optimized Slater-Type Basis Sets for the Elements 1-118. *J. Comput. Chem.* **2003**, *24* (9), 1142–1156.

(129) Alkan, F.; Holmes, S. T.; Dybowski, C. Role of Exact Exchange and Relativistic Approximations in Calculating ^{19}F Magnetic Shielding in Solids Using a Cluster Ansatz. *J. Chem. Theory Comput.* **2017**, *13* (10), 4741–4752.

(130) Van Lenthe, E.; Baerends, E. J.; Snijders, J. G. Relativistic Regular Two-Component Hamiltonians. *J. Chem. Phys.* **1993**, *99* (6), 4597–4610.

(131) Philipsen, P.; van Lenthe, E.; Snijders, J.; Baerends, E. Relativistic Calculations on the Adsorption of CO on the (111) Surfaces of Ni, Pd, and Pt within the Zeroth-Order Regular Approximation. *Phys. Rev. B* **1997**, *56* (20), 13556–13562.

(132) Van Lenthe, E.; Baerends, E. J.; Snijders, J. G. Relativistic Total Energy Using Regular Approximations. *J. Chem. Phys.* **1994**, *101* (11), 9783–9792.

(133) Wolff, S. K.; Ziegler, T. Calculation of DFT-GIAO NMR Shifts with the Inclusion of Spin-Orbit Coupling. *J. Chem. Phys.* **1998**, *109* (3), 895–905.

(134) Hindermann, D. K.; Cornwell, C. D. Vibrational Corrections to the Nuclear-Magnetic Shielding and Spin-Rotation Constants for Hydrogen Fluoride. Shielding Scale for ^{19}F. *J. Chem. Phys.* **1968**, *48* (9), 4154–4161.

(135) Jameson, C. J.; Jameson, A. K.; Burrell, P. M. ^{19}F Nuclear Magnetic Shielding Scale from Gas Phase Studies. *J. Chem. Phys.* **1980**, *73* (12), 6013–6020.

(136) Jameson, C. J.; Jameson, A. K. Absolute Shielding Scale For ^{29}Si. *Chem. Phys. Lett.* **1988**, *149*, 300–305.

(137) Hooper, R. W.; Klein, B. A.; Michaelis, V. K. Dynamic Nuclear Polarization (DNP) 101: A New Era for Materials. *Chem. Mater.* **2020**, *32* (11), 4425–4430.

(138) Quinn, C. M.; Zadorozhnyi, R.; Struppe, J.; Sergeyev, I. V.; Gronenborn, A. M.; Polenova, T. Fast ^{19}F Magic-Angle Spinning Nuclear Magnetic Resonance for the Structural Characterization of Active Pharmaceutical Ingredients in Blockbuster Drugs. *Anal. Chem.* **2021**, *93* (38), 13029–13037.

(139) Lu, M.; Wang, M.; Sergeyev, I. V.; Quinn, C. M.; Struppe, J.; Rosay, M.; Maas, W.; Gronenborn, A. M.; Polenova, T. ^{19}F Dynamic Nuclear Polarization at Fast Magic Angle Spinning for NMR of HIV-1 Capsid Protein Assemblies. *J. Am. Chem. Soc.* **2019**, *141* (14), 5681–5691.

(140) Guo, C.; Fritz, M. P.; Struppe, J.; Wegner, S.; Stringer, J.; Sergeyev, I. V.; Quinn, C. M.; Gronenborn, A. M.; Polenova, T. Fast ^{19}F Magic Angle Spinning NMR Crystallography for Structural Characterization of Fluorine-Containing Pharmaceutical Compounds. *Anal. Chem.* **2021**, *93* (23), 8210–8218.

(141) Barbet-Massin, E.; Pell, A. J.; Retel, J. S.; Andreas, L. B.; Jaudzems, K.; Franks, W. T.; Nieuwkoop, A. J.; Hiller, M.; Higman, V.; Guerry, P.; Bertarello, A.; Knight, M. J.; Felletti, M.; Le Marchand, T.; Kotelovica, S.; Akopjana, I.; Tars, K.; Stoppini, M.; Bellotti, V.; Bolognesi, M.; Ricagno, S.; Chou, J. J.; Griffin, R. G.; Oschkinat, H.; Lesage, A.; Emsley, L.; Herrmann, T.; Pintacuda, G. Rapid Proton-Detected NMR Assignment for Proteins with Fast Magic Angle Spinning. *J. Am. Chem. Soc.* **2014**, *136* (35), 12489–12497.

(142) White, J.; Beck, L.; Haw, J. Characterization of Hydrogen Bonding in Zeolites by Proton-State NMR Spectroscopy. *J. Am. Chem. Soc.* **1992**, *114*, 6182–6189.

(143) Potnuru, L. R.; Yarava, J. R.; Pahari, B.; Ramanathan, K. V. Use of Reverse Cross-Polarization for Editing Solid–State Proton NMR Spectra. *J. Mol. Struct.* **2018**, *1168*, 49–55.

(144) Crosby, R.; Reese, R.; Haw, J. Cross Polarization Magic Angle Spinning Proton NMR of Solids. *J. Am. Chem. Soc.* **1988**, *110*, 8550–8551.

(145) Lewandowski, J. R.; Dumez, J. N.; Akbey, Ü.; Lange, S.; Emsley, L.; Oschkinat, H. Enhanced Resolution and Coherence Lifetimes in the Solid-State NMR Spectroscopy of

Perdeuterated Proteins under Ultrafast Magic-Angle Spinning. *J. Phys. Chem. Lett.* **2011**, *2* (17), 2205–2211.

(146) Tirotta, I.; Dichiarante, V.; Pigliacelli, C.; Cavallo, G.; Terraneo, G.; Bombelli, F. B.; Metrangolo, P.; Resnati, G. ^{19}F Magnetic Resonance Imaging (MRI): From Design of Materials to Clinical Applications. *Chem. Rev*. **2015**, *115*, 1106–1129.

(147) Tang, X.; Li, A.; Zuo, C.; Liu, X.; Luo, X.; Chen, L.; Li, L.; Lin, H.; Gao, J. Water-Soluble Chemically Precise Fluorinated Molecular Clusters for Interference-Free Multiplex ^{19}F MRI in Living Mice. *ACS Nano* **2023**, *17* (5), 5014–5024.

Appendix A: Supplementary Data for Chapter 2

Unmasking Fluorinated Moieties on the Surface of Hydride-Terminated Silicon Nanoparticles Using Solid-state NMR Spectroscopy

Table A1. Elemental Composition of 6 nm H-SiNPs as Determined by EDX.

Element	At%
C	89.46
O	1.37
F	0.05
Si	8.36
[a]Cu	0.76

[a]Copper signal arises from the ultrathin carbon-coated copper grid (Electron Microscopy Inc.)

Table A2. Magnetic Coupling of the Highest-Lying Occupied MOs that Transform as *E* with the Respective LUMOs in $Si_{10}H_{16}$ and $Si_{10}H_{15}F$ Clusters.

Field component	Real (R) or imaginary (I)	[a]Unoccupied spinorbital	[a]Occupied spinorbital	Magnitude of MO coupling	ΔE (eV)
$Si_{10}H_{16}$					
1	I	157	151	0.958187×10^{-1}	8.273
2	I	157	153	0.973642×10^{-1}	8.272
$Si_{10}H_{15}F$					
1	I	165	161	0.154370	7.701
2	I	165	163	0.155129	7.700

[a]See supplementary note 1.

Supplementary note 1: ADF uses the spin-orbit branch of the NMR code to compute pairwise contributions of MO couplings to the paramagnetic shielding tensor (even if spin-orbit effects are not included). For scalar relativistic calculations, the contributions are listed for **equivalent** pairs of spinorbitals. For example, the sum of the contributions from occupied spinorbitals 1 (α) and 2 (β) would correspond to the total contribution for occupied MO 1. The spinorbitals from the NMR calculations are related to the canonical MOs from the single point calculation as follows:

$Si_{10}H_{16}$: Spinorbital 157 → "α" components of 24*a_1* ; Spinorbital 151→"α" components of 25*e(2)* ; Spinorbital 153→"α" components of 25*e(1)*

$Si_{10}H_{15}F$: Spinorbital 165 → "α" components of 26*a_1* ; Spinorbital 161→"α" components of 26*e(2)* ; Spinorbital 163→"α" components of 26*e(1)*

Table A3. Influence of Spin-Orbit Coupling on the ^{19}F and ^{29}Si Magnetic Shielding of K_2SiF_6 Computed at the ZORA/PBE0(50)/TZ2P Level of Theory.

Model	**Scalar ZORA**		**Spin-Orbit ZORA**	
	σ_{iso} (^{19}F)/ppm	**σ_{iso} (^{29}Si)/ppm**	**σ_{iso} (^{19}F)/ppm**	**σ_{iso} (^{29}Si)/ppm**
$[K_8SiF_6]^{6+}$	328.402	553.619	331.444	566.370

Table A4. Comparison of the Experimental ^{19}F and ^{29}Si Isotropic Magnetic Shielding for SiF_4 (gas phase) to the Theoretical Values Computed with a 25% or 50% Admixture of HFX.

Level of Theory	**σ_{iso} (^{19}F)/ppm**	**σ_{iso} (^{29}Si)/ppm**
Scalar ZORA/PBE0/TZ2P	345.139	464.153
Scalar ZORA/PBE0(50% HFX)/TZ2P	[a]354.159	481.198
Experiment	**363 ± 6**[1,2]	**482 ± 10**[3]

[a]Corresponds to a computed ^{19}F chemical shift of −160.757 ppm

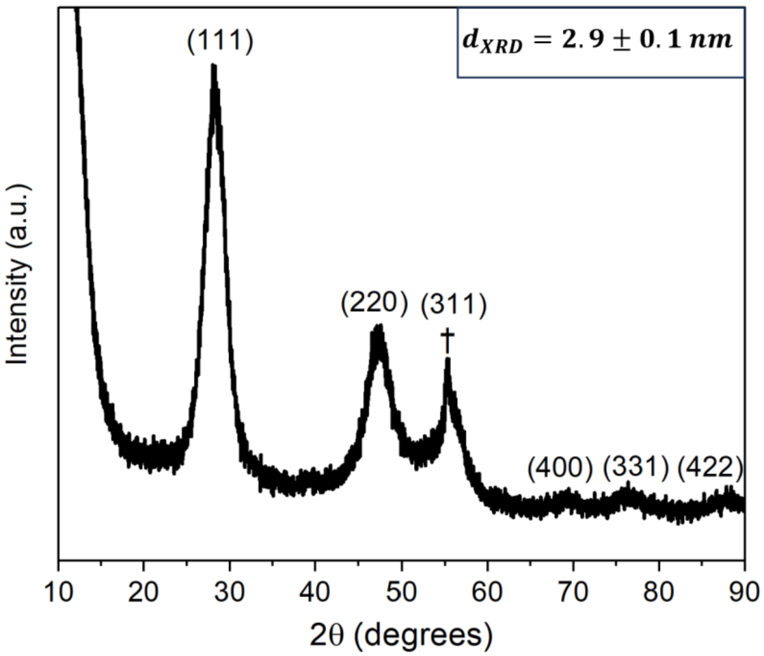

Figure A1. Powder XRD pattern for the 6 nm H-SiNPs sample. The cross indicates an instrumental artifact.

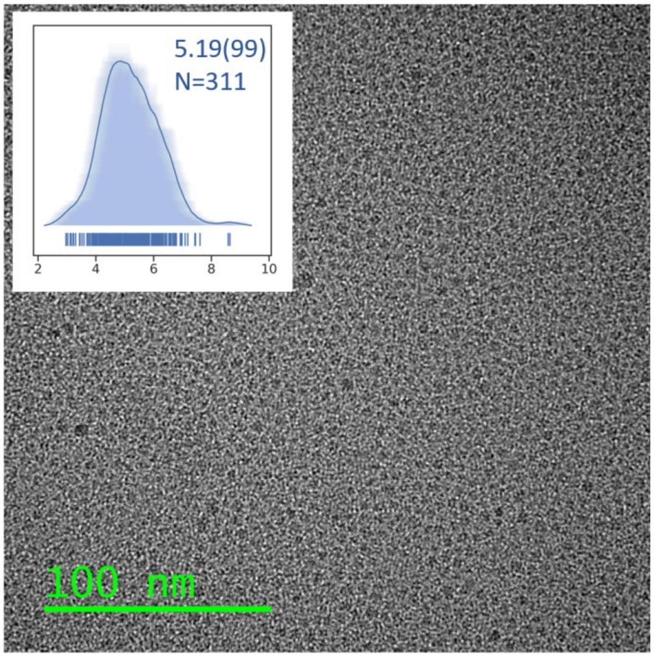

Figure A2. Bright-field TEM images of dodecyl terminated silicon nanoparticles. The inset shows the average shifted histogram.[4]

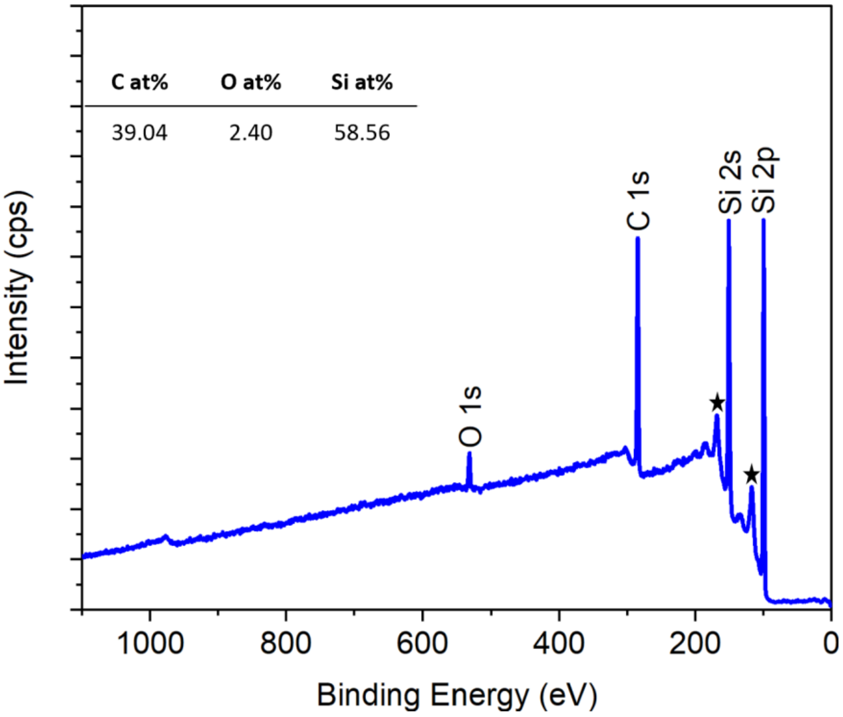

C at%	O at%	Si at%
39.04	2.40	58.56

Figure A3. XPS survey spectrum for 6 nm H-SiNPs before NMR analysis. Stars (★) indicate Si plasmon loss peaks.

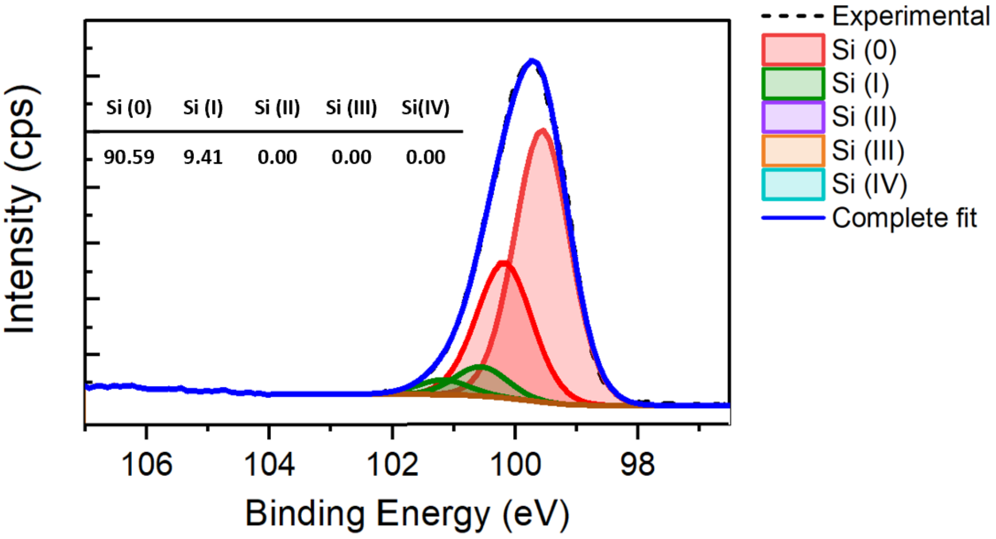

Si (0)	Si (I)	Si (II)	Si (III)	Si(IV)
90.59	9.41	0.00	0.00	0.00

Figure A4. High-resolution Si 2p XPS spectrum for 6 nm H-SiNPs before NMR analysis. The table in the inset indicates the Si 2p peak composition.

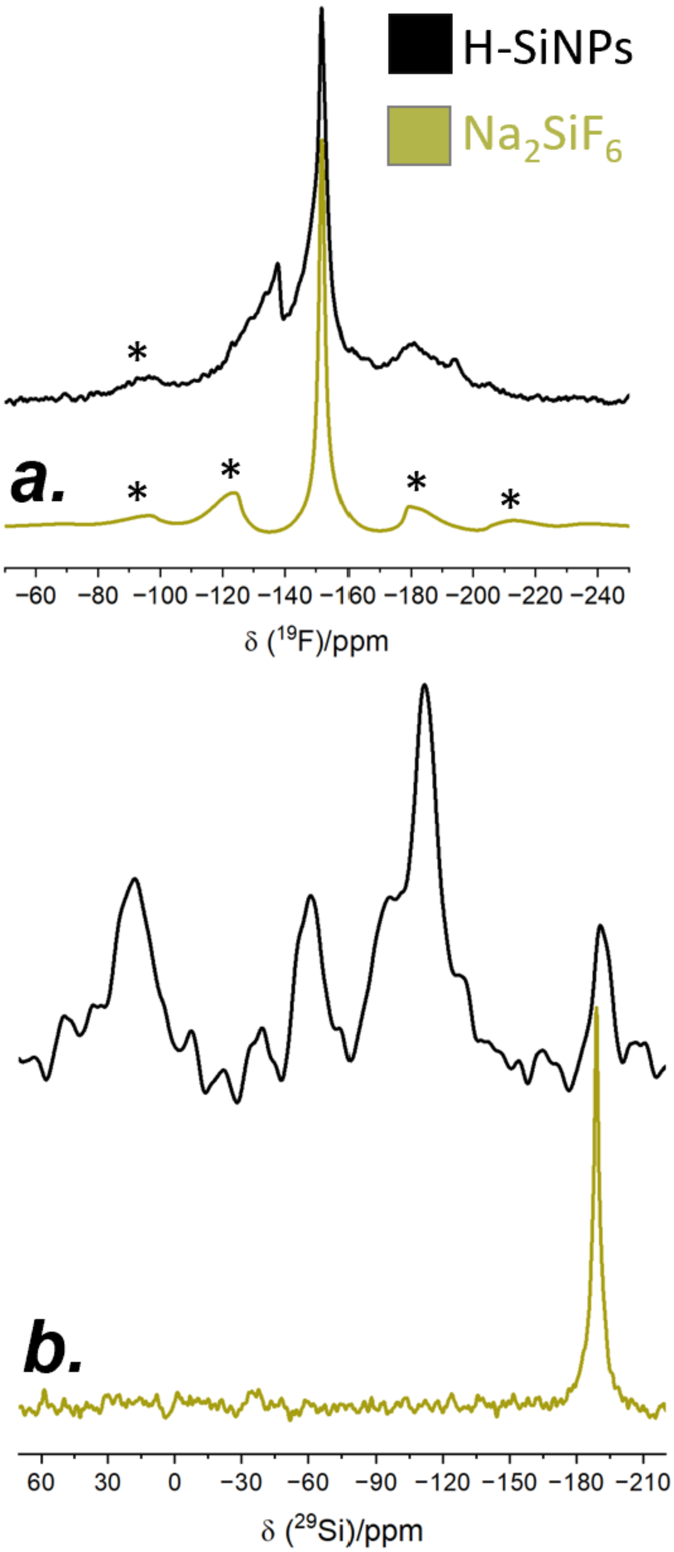

Figure A5. (a) ^{19}F MAS NMR and (b) ^{29}Si{^{19}F} CPMAS NMR spectra of 6 nm H-SiNPs and Na_2SiF_6. The spectra were collected with ν_{rot} = 10-20 kHz. Asterisks (*) indicate spinning sidebands.

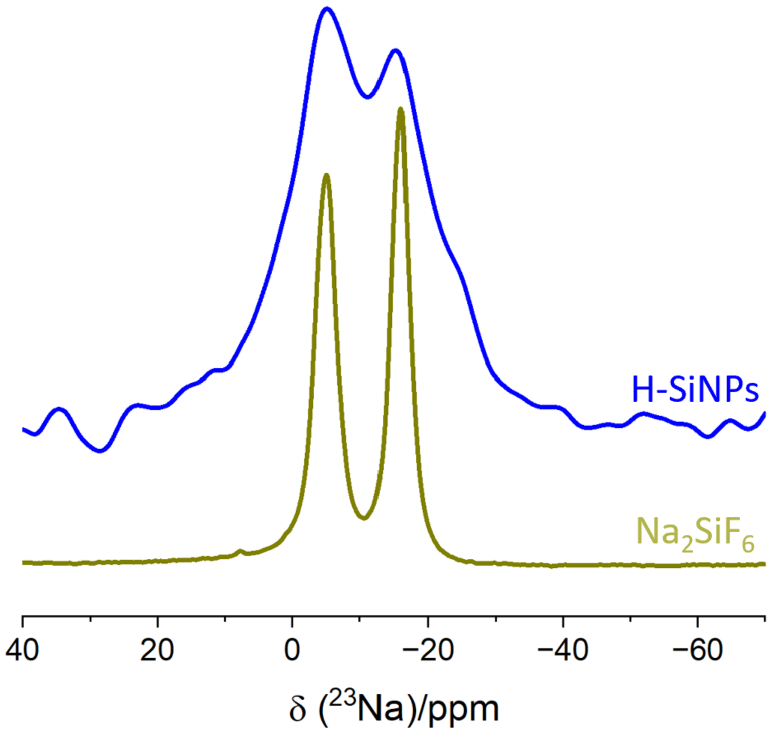

Figure A6. ^{23}Na MAS NMR spectra of 6 nm H-SiNPs and Na_2SiF_6. Both spectra were collected with ν_{rot} = 10 kHz.

Supplementary note 2: In the following images of the clusters used to model the surface of H-SiNPs, spheres colored white, beige, red, and green represent hydrogen, silicon, oxygen, and fluorine, respectively.

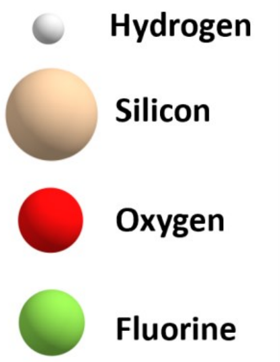

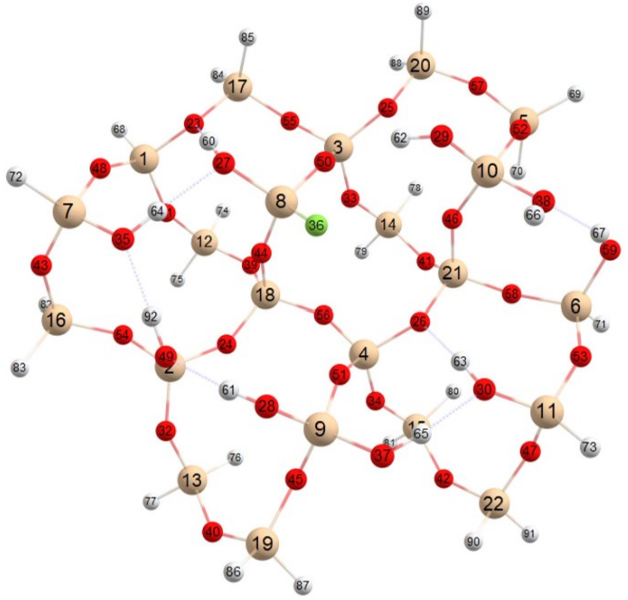

Si4: δ (^{29}Si)/ppm = -104.927
Si8: δ (^{29}Si)/ppm = -102.107
Si18: δ (^{29}Si)/ppm = -105.734
F36: δ (^{19}F)/ppm = -148.689

Figure A7. Oxidized model containing an O_3SiF.

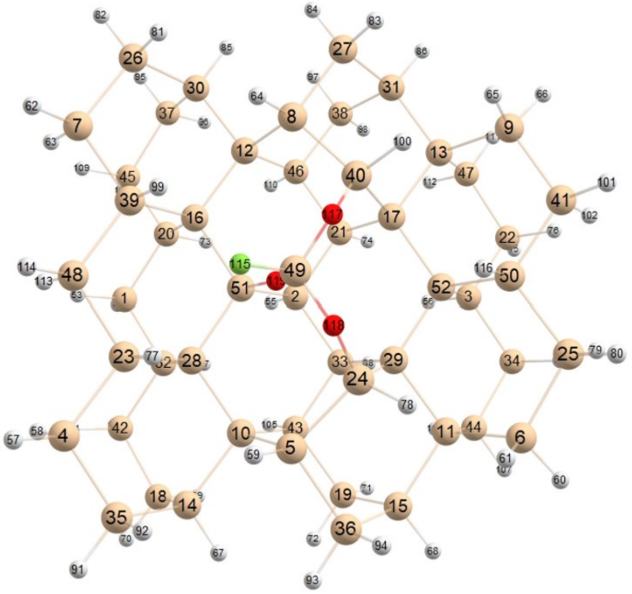

Si24: δ (^{29}Si)/ppm = -18.411
Si39: δ (^{29}Si)/ppm = -105.785
Si49: δ (^{29}Si)/ppm = -100.627
Si51: δ (^{29}Si)/ppm = -6.108
F115: δ (^{19}F)/ppm = -135.585

Figure A8. Si(110) model containing an O_3SiF.

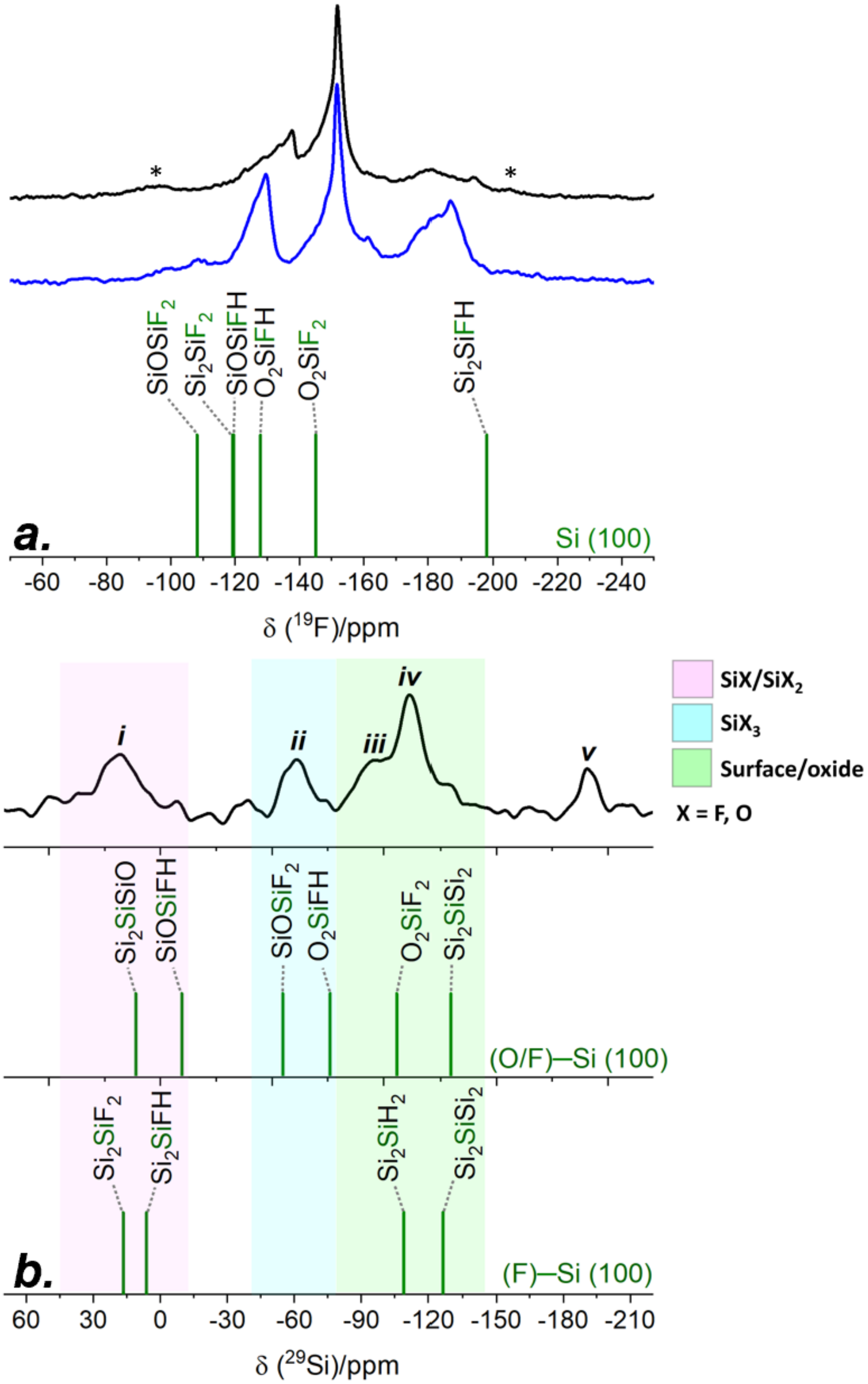

Figure A9. (a) Comparison of the calculated ^{19}F chemical shifts to the experimental ^{19}F MAS NMR spectra of 6 nm H-SiNPs. (b) Comparison of the calculated ^{29}Si chemical shifts to the experimental ^{29}Si{^{19}F} CPMAS spectra. For clarity, the ^{29}Si chemical shifts in panel (b) are separated into models containing groups with both oxygen and fluorine (O/F)−Si(100) or fluorine alone (F)−Si(100).

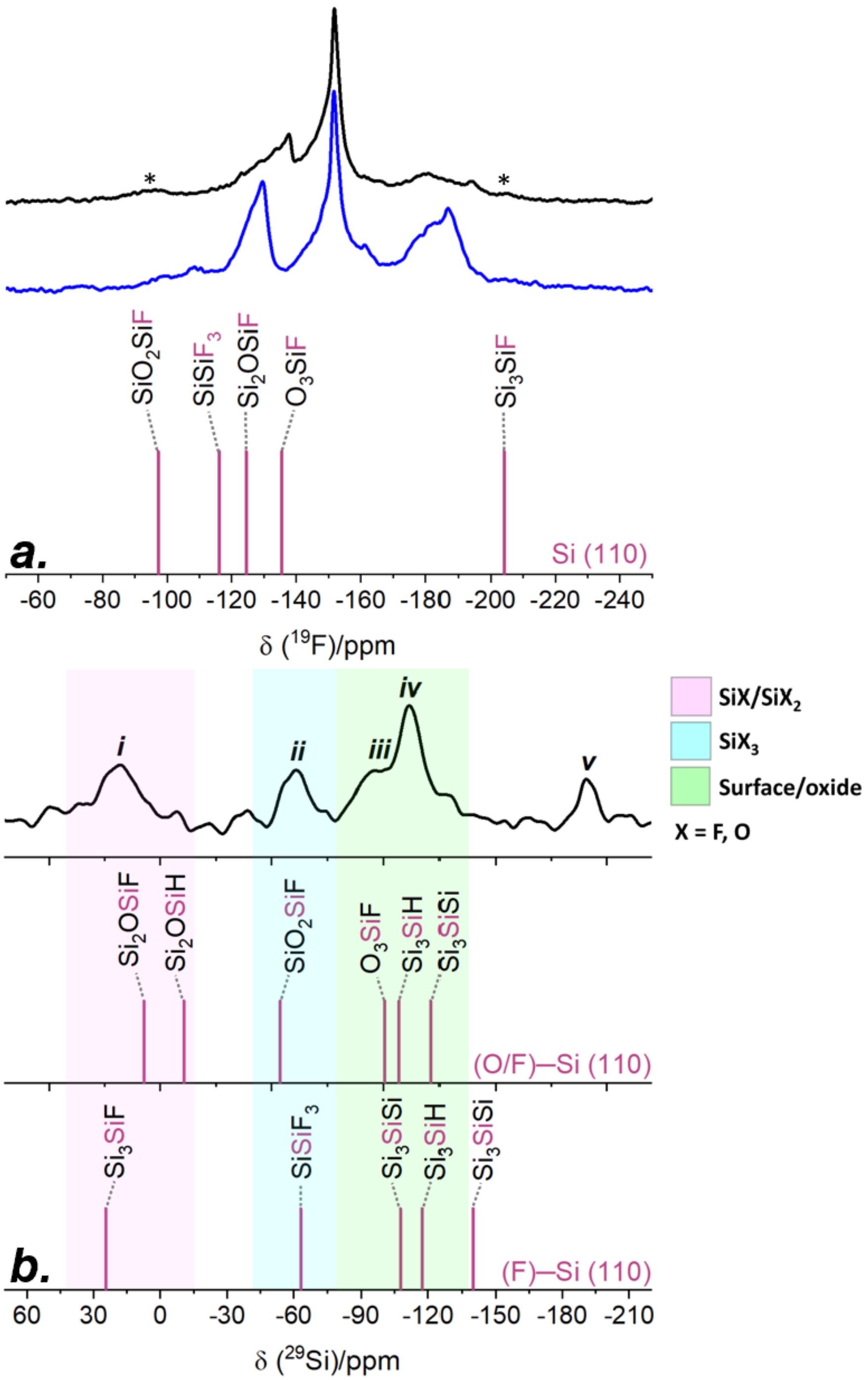

Figure A10. (a) Comparison of the calculated ^{19}F chemical shifts to the experimental ^{19}F MAS NMR spectra of 6 nm H-SiNPs. (b) Comparison of the calculated ^{29}Si chemical shifts to the experimental ^{29}Si{^{19}F} CPMAS spectra. For clarity, the ^{29}Si chemical shifts in panel (b) are separated into models containing groups with both oxygen and fluorine (O/F)−Si(110) or fluorine alone (F)−Si(110).

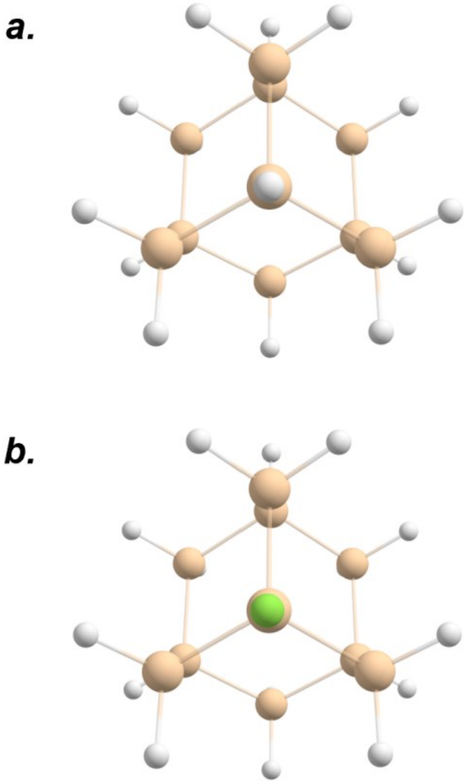

Figure A11. (a) $Si_{10}H_{16}$ and (b) $Si_{10}H_{15}F$ models with C_{3v} symmetry as viewed from down the C_3 axis which corresponds to the molecular z-axis.

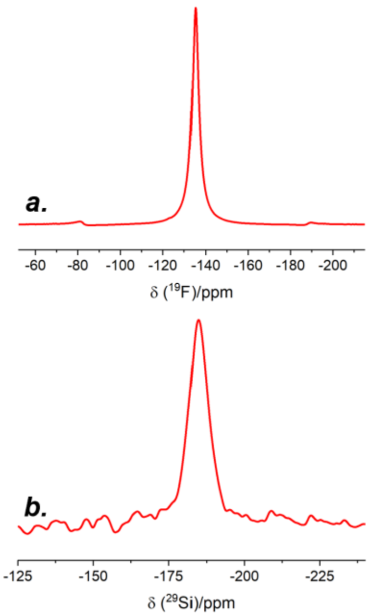

Figure A12. (a) ^{19}F and (b) ^{29}Si MAS NMR spectra of K_2SiF_6 collected with a spinning frequency of 20 kHz. The recycle delays were set to 310 and 500 s for ^{19}F and ^{29}Si, respectively.

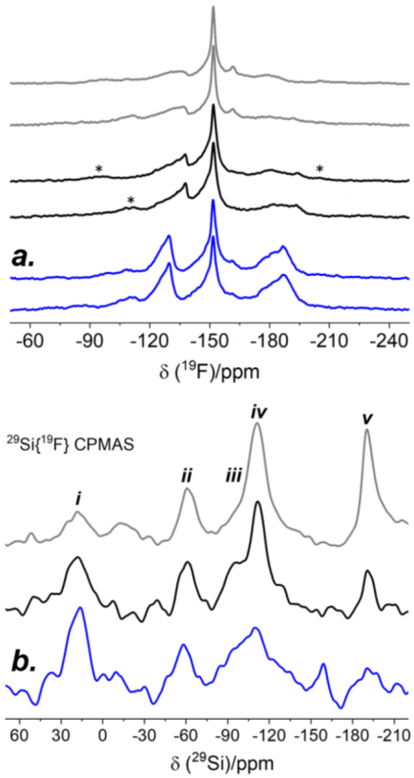

Figure A13. (a) ^{19}F MAS NMR and (b) ^{29}Si{^{19}F} CPMAS NMR spectra of 6 nm H-SiNPs. Each color trace corresponds to a different sample of 6 nm H-SiNPs. For the colored pairs in (a), the top (bottom) trace was collected with $\nu_{rot} = 20$ kHz (15 kHz). All spectra in (b) were collected with $\nu_{rot} = 10$ kHz. Asterisk (*) indicates spinning sidebands.

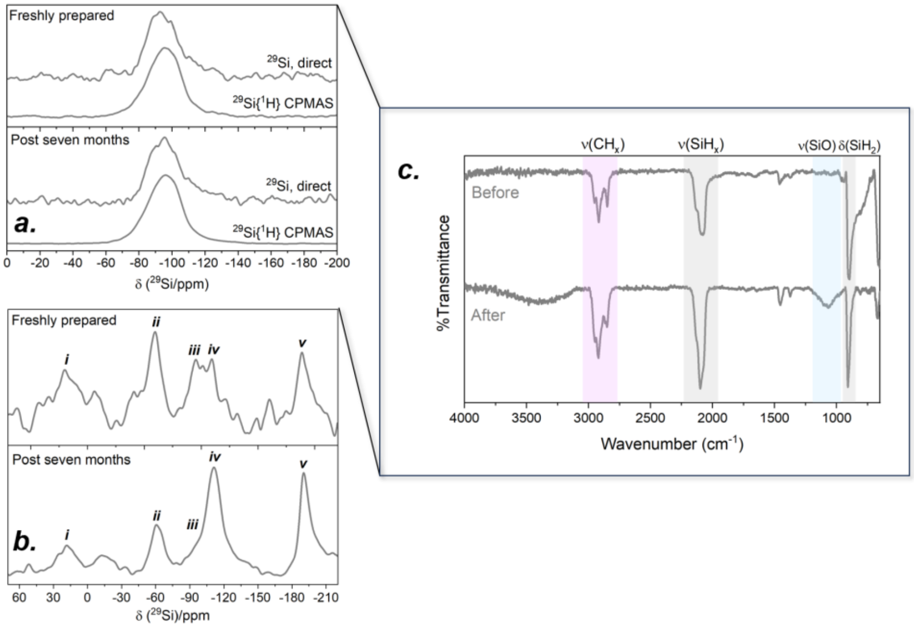

Figure A14. (a) ^{29}Si MAS, ^{29}Si{^{1}H} CPMAS, and (b) ^{29}Si{^{19}F} CPMAS NMR spectra of a sample of H-SiNPs freshly prepared and after seven months stored in a sealed 3.2 mm rotor under ambient conditions. (c) IR spectra were collected before NMR analysis (freshly prepared) and after (post-seven months).

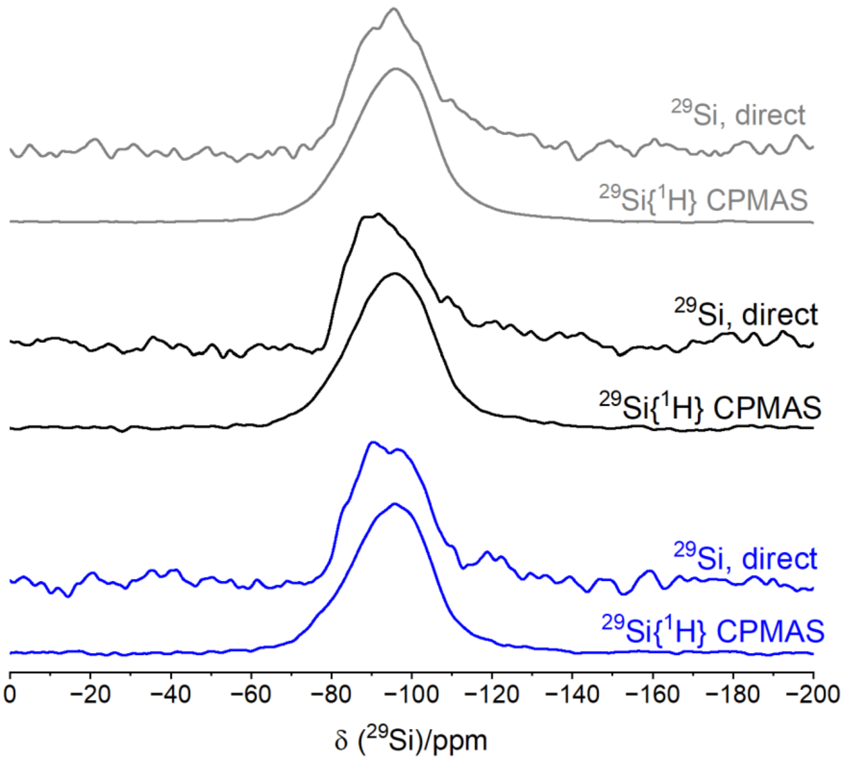

Figure A15. ^{29}Si MAS and ^{29}Si{^{1}H} CPMAS NMR spectra of three samples of H-SiNPs collected with $\nu_{\mathrm{rot}} = 10$ kHz.

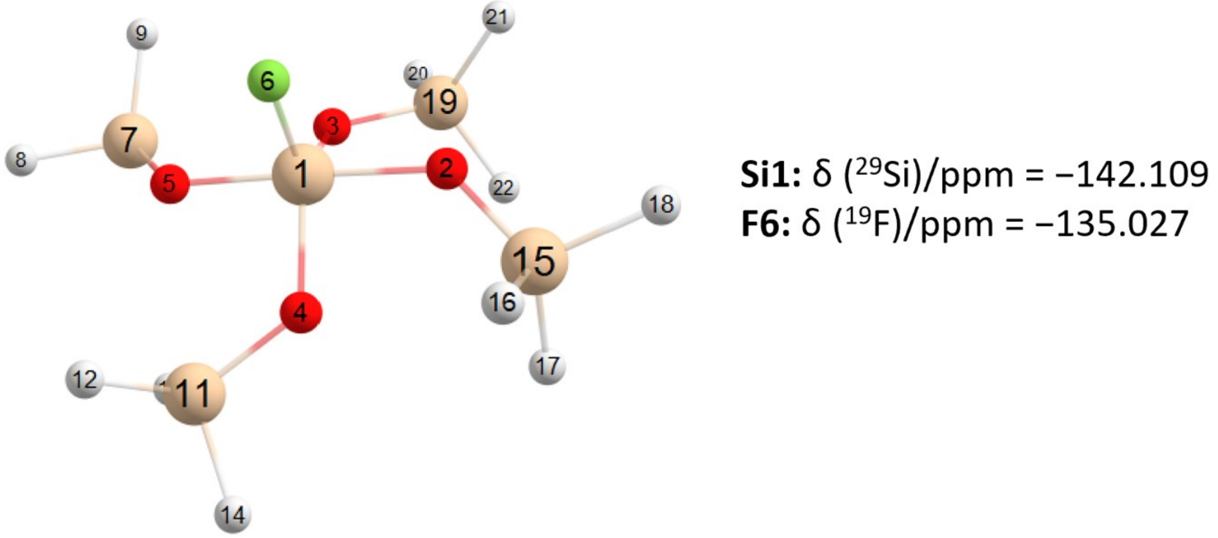

Figure A16. Quantum chemical model of an O_4SiF species and the ^{19}F and ^{29}Si chemical shifts computed at the scalar ZORA/PBE0(50)/TZ2P level of theory. This cluster has a formal charge of −1.

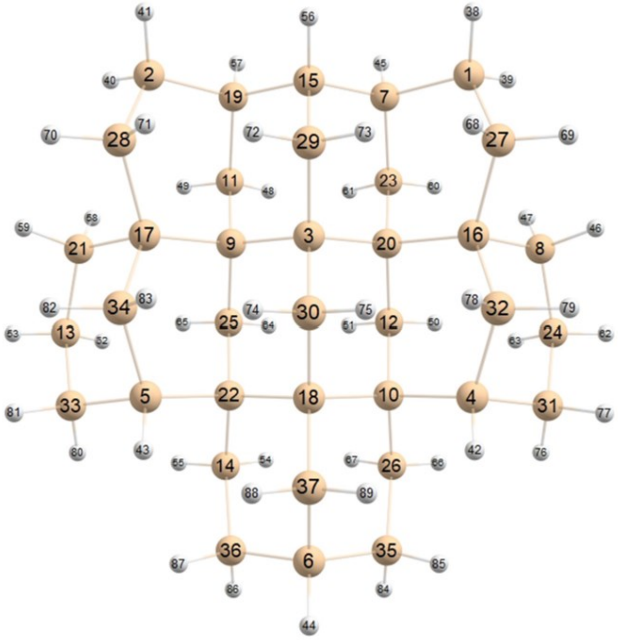

Si3: δ (^{29}Si)/ppm = -123.077
Si30: δ (^{29}Si)/ppm = -96.167
Si32: δ (^{29}Si)/ppm = -92.816

Figure A17. Hydride-terminated model based on Si(100).

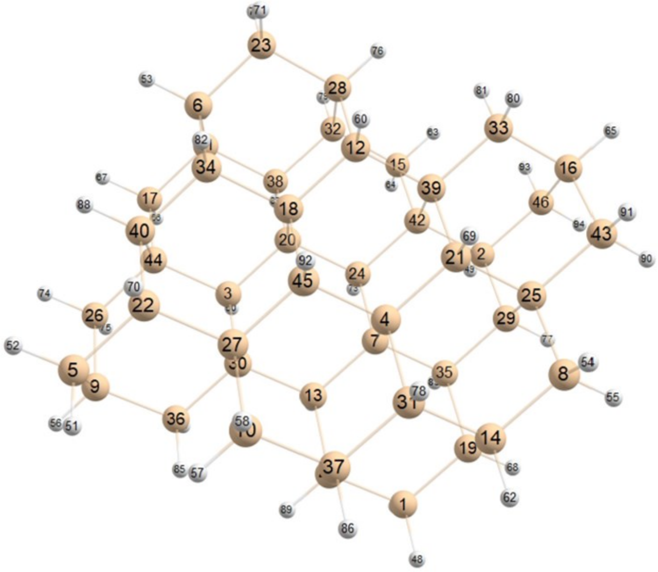

Si4: δ (^{29}Si)/ppm = -110.217
Si21: δ (^{29}Si)/ppm = -101.363
Si45: δ (^{29}Si)/ppm = -105.126

Figure A18. Hydride-terminated model based on Si(111).

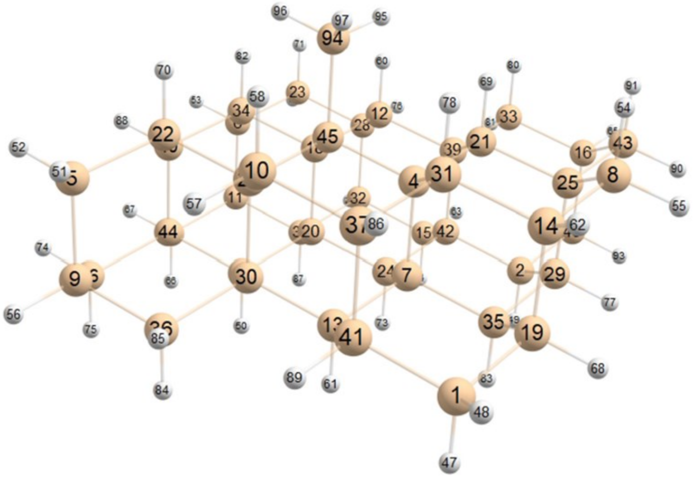

Si4: δ (^{29}Si)/ppm = -128.257

Si21: δ (^{29}Si)/ppm = -113.403

Si45: δ (^{29}Si)/ppm = -139.216

Si94: δ (^{29}Si)/ppm = -105.201

Figure A19. Hydride-terminated model with an SiH_3 grafted onto Si(111).

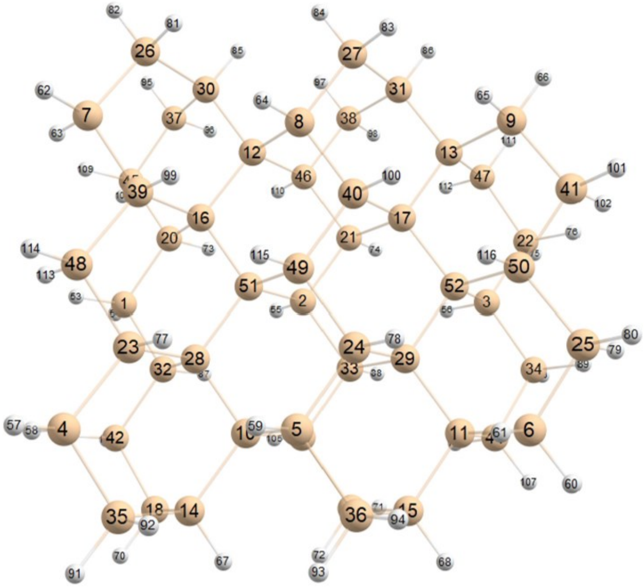

Si24: δ (^{29}Si)/ppm = -127.198

Si39: δ (^{29}Si)/ppm = -119.119

Si49: δ (^{29}Si)/ppm = -120.589

Si51: δ (^{29}Si)/ppm = -111.933

Figure A20. Hydride-terminated model based on Si(110).

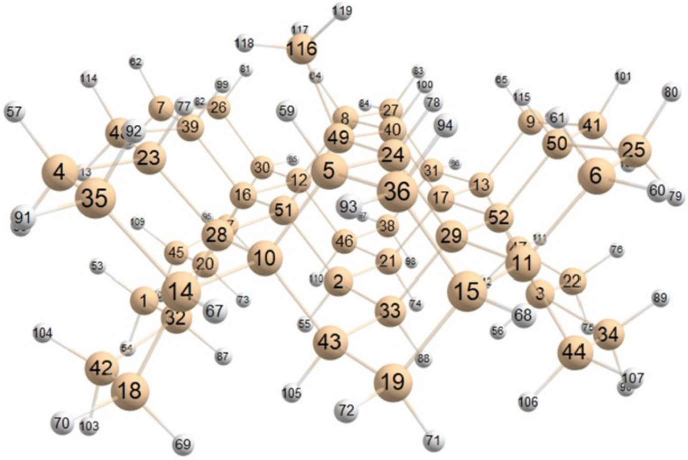

Si24: δ (^{29}Si)/ppm = -56.185
Si39: δ (^{29}Si)/ppm = -63.525
Si49: δ (^{29}Si)/ppm = -61.337
Si51: δ (^{29}Si)/ppm = -79.312
Si116: δ (^{29}Si)/ppm = -92.831

Figure A21. Hydride-terminated model with an SiH_3 grafted onto Si(110).

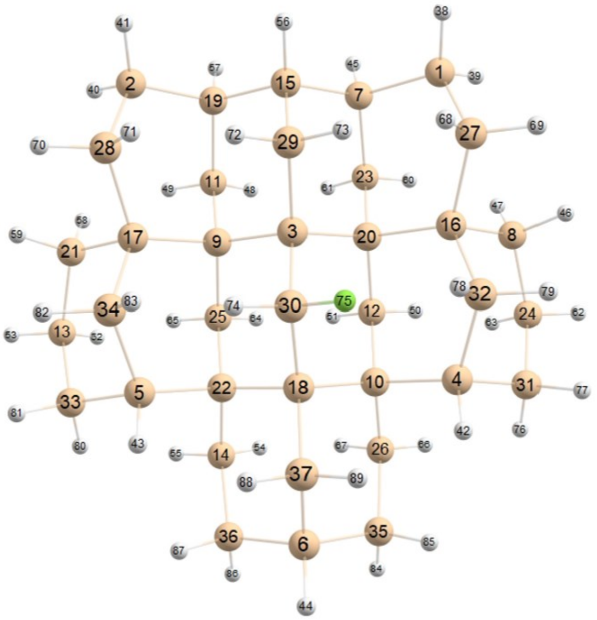

Si3: δ (^{29}Si)/ppm = -126.144
Si30: δ (^{29}Si)/ppm = 6.201
Si32: δ (^{29}Si)/ppm = -109.116
F75: δ (^{19}F)/ppm = -197.995

Figure A22. Si(100) model containing Si_2SiFH.

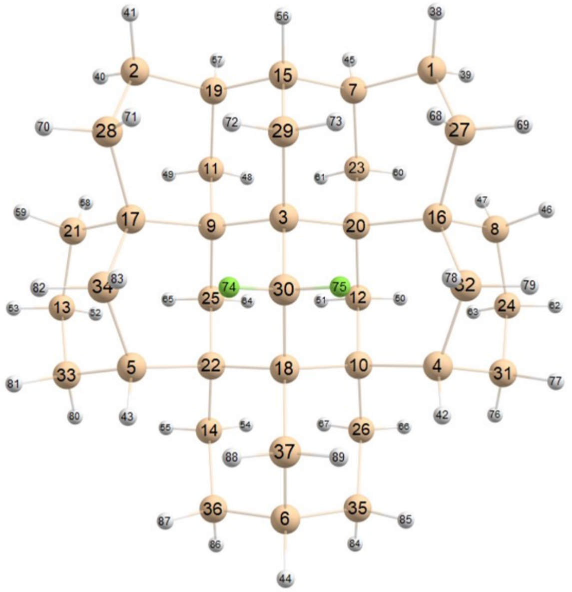

Si3: δ (^{29}Si)/ppm = -127.92
Si30: δ (^{29}Si)/ppm = 16.699
Si32: δ (^{29}Si)/ppm = -108.095
F74: δ (^{19}F)/ppm = -118.884
F75: δ (^{19}F)/ppm = -119.195

Figure A23. Si(100) model containing Si_2SiF_2.

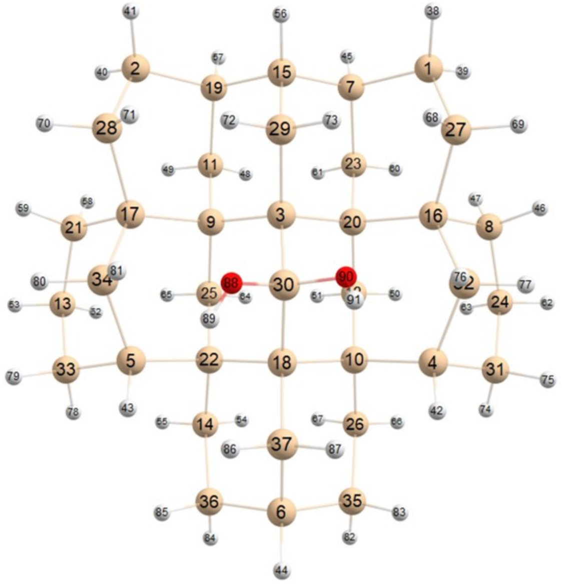

Si3: δ (^{29}Si)/ppm = -98.47
Si30: δ (^{29}Si)/ppm = 15.817
Si32: δ (^{29}Si)/ppm = -82.67

Figure A24. Si(100) model containing $Si_2Si(OH)_2$.

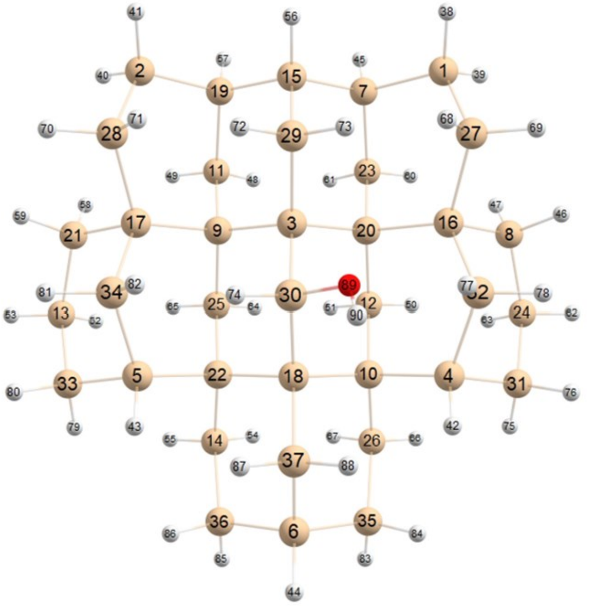

Si3: δ (^{29}Si)/ppm = -124.823
Si30: δ (^{29}Si)/ppm = -15.228
Si32: δ (^{29}Si)/ppm = -103.565

Figure A25. Si(100) model containing $Si_2SiH(OH)$.

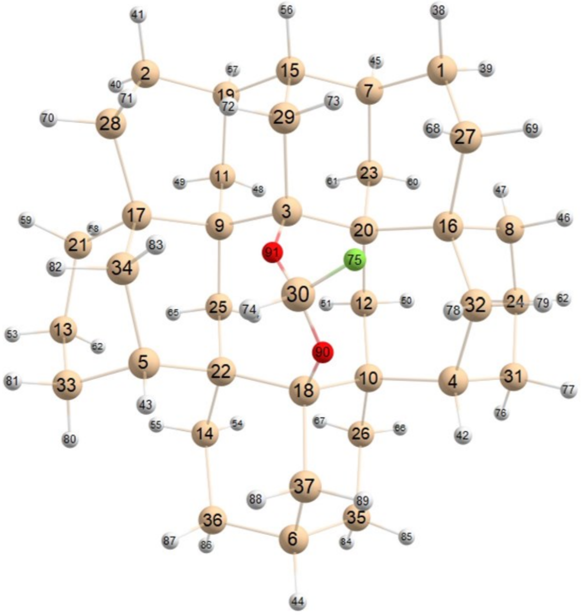

Si3: δ (^{29}Si)/ppm = 27.511
Si30: δ (^{29}Si)/ppm = -76.054
Si32: δ (^{29}Si)/ppm = -99.413
F75: δ (^{19}F)/ppm = -127.907

Figure A26. Si(100) model containing O_2SiFH.

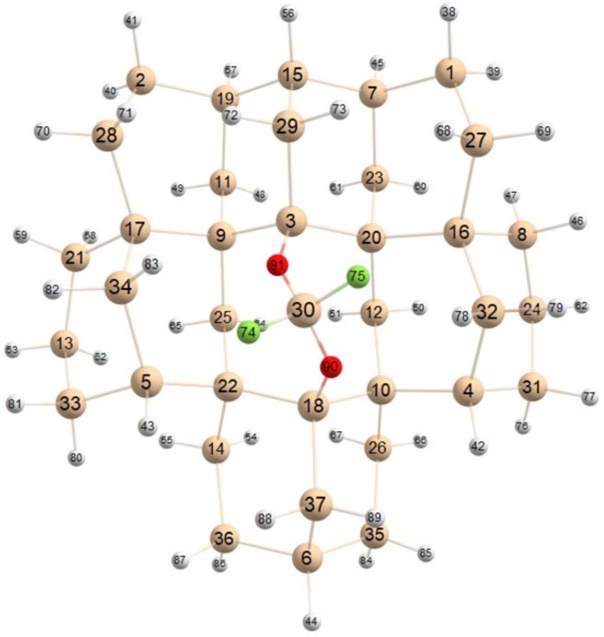

Si3: δ (^{29}Si)/ppm = 11.017
Si30: δ (^{29}Si)/ppm = -105.887
Si32: δ (^{29}Si)/ppm = -108.807
F74: δ (^{19}F)/ppm = -141.607
F75: δ (^{19}F)/ppm = -145.128

Figure A27. Si(100) model containing O_2SiF_2.

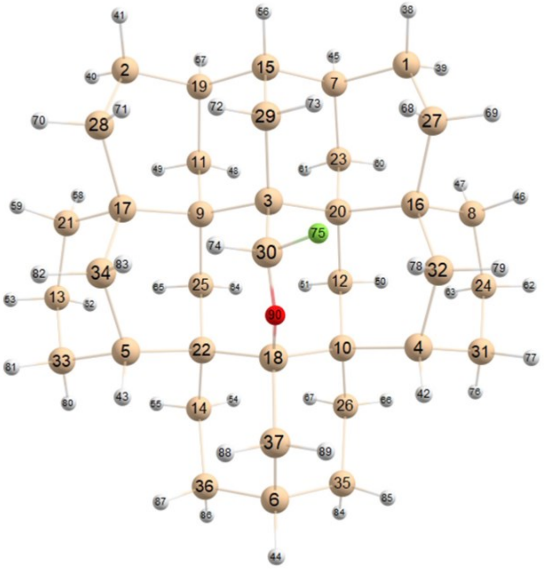

Si3: δ (^{29}Si)/ppm = -152.672
Si30: δ (^{29}Si)/ppm = -9.593
Si32: δ (^{29}Si)/ppm = -114.553
F75: δ (^{19}F)/ppm = -119.511

Figure A28. Si(100) model containing SiOSiFH.

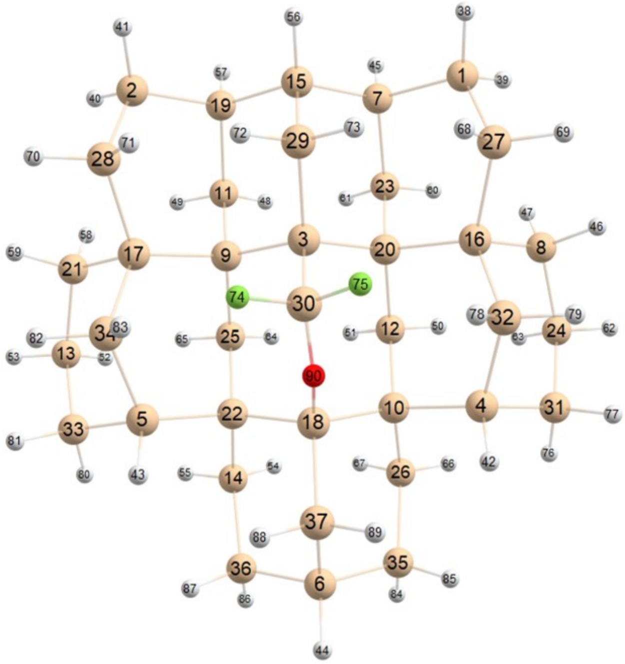

Si3: δ (^{29}Si)/ppm = -129.637
Si30: δ (^{29}Si)/ppm = -54.787
Si32: δ (^{29}Si)/ppm = -106.685
F74: δ (^{19}F)/ppm = -104.446
F75: δ (^{19}F)/ppm = -108.114

Figure A29. Si(100) model containing $SiOSiF_2$.

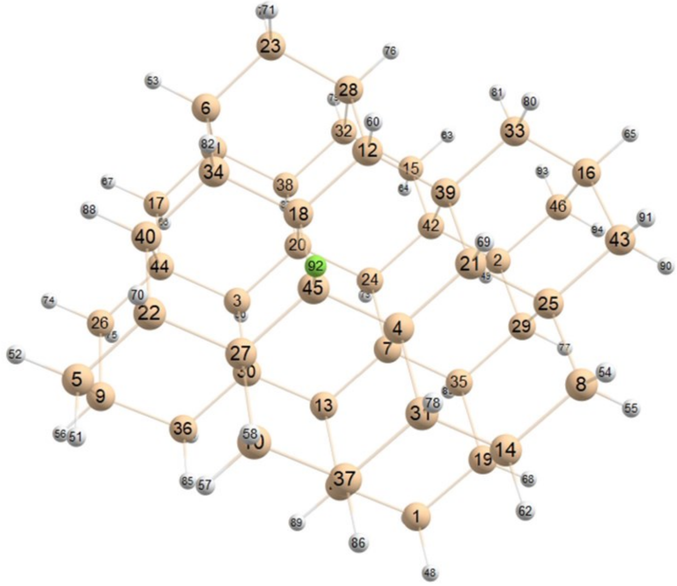

Si4: δ (^{29}Si)/ppm = -112.292
Si21: δ (^{29}Si)/ppm = -105.781
Si45: δ (^{29}Si)/ppm = 19.999
F92: δ (^{19}F)/ppm = -188.729

Figure A30. Si(111) model containing Si_3SiF.

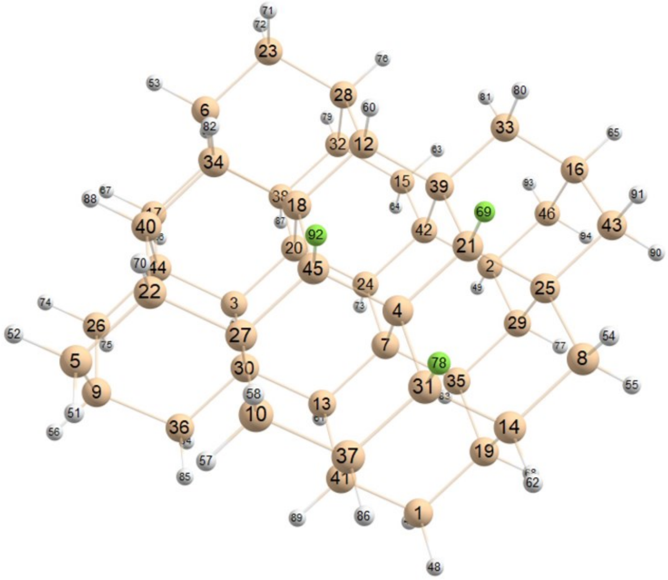

Si4: δ (^{29}Si)/ppm = -104.74
Si34: δ (^{29}Si)/ppm = -110.101
Si45: δ (^{29}Si)/ppm = 18.609
F92: δ (^{19}F)/ppm = -200.188

Figure A31. Si(111) model containing three adjacent Si_3SiF groups.

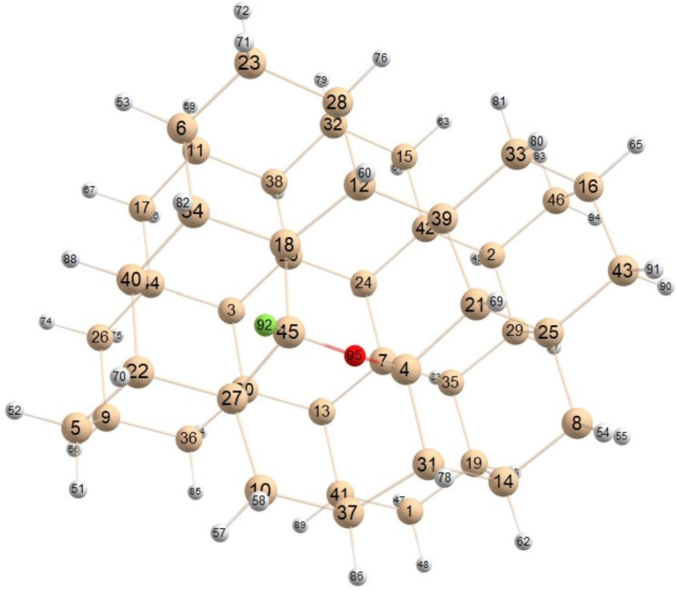

Si4: δ (^{29}Si)/ppm = 23.084
Si21: δ (^{29}Si)/ppm = -93.593
Si45: δ (^{29}Si)/ppm = 41.334
F92: δ (^{19}F)/ppm = -117.686

Figure A32. Si(111) model containing Si_2OSiF.

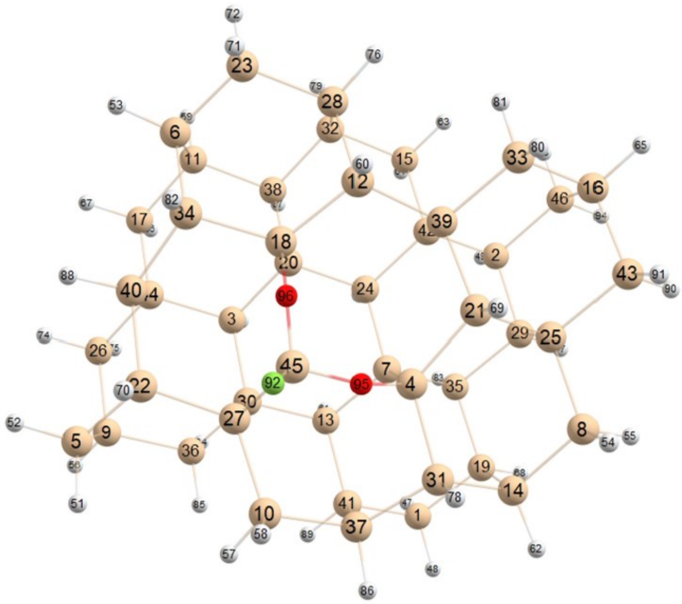

Si4: δ (^{29}Si)/ppm = -2.429
Si21: δ (^{29}Si)/ppm = -95.122
Si45: δ (^{29}Si)/ppm = -56.852
F92: δ (^{19}F)/ppm = -120.961

Figure A33. Si(111) model containing SiO_2SiF.

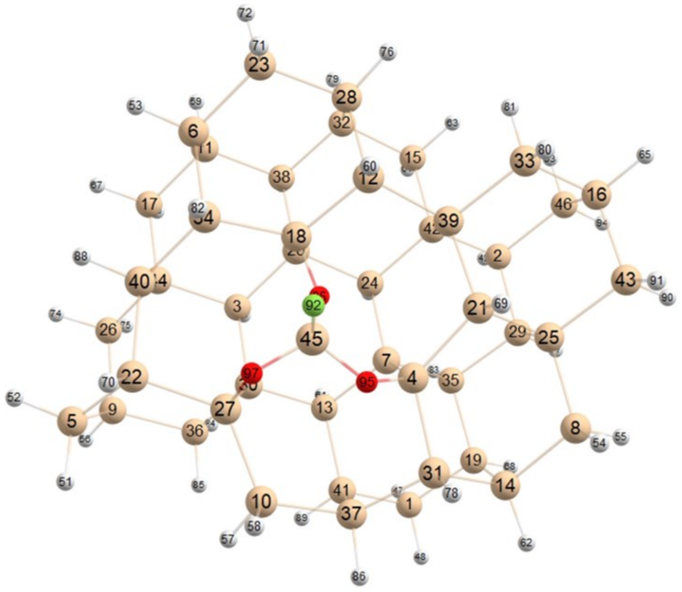

Si4: δ (^{29}Si)/ppm = 14.822
Si21: δ (^{29}Si)/ppm = -99.033
Si45: δ (^{29}Si)/ppm = -99.804
F92: δ (^{19}F)/ppm = -147.175

Figure A34. Si(111) model containing O_3SiF.

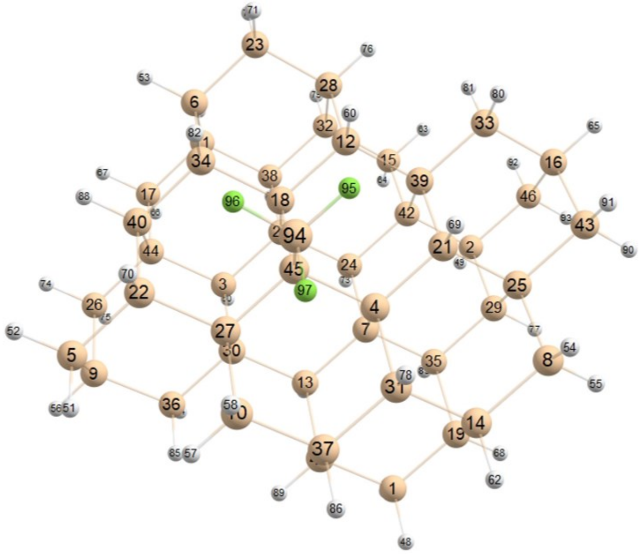

Si4: δ (^{29}Si)/ppm = -140.019
Si21: δ (^{29}Si)/ppm = -110.541
Si45: δ (^{29}Si)/ppm = -169.059
Si94: δ (^{29}Si)/ppm = -65.518
F95: δ (^{19}F)/ppm = -94.997

Figure A35. Si(111) model with an SiF_3 grafted on.

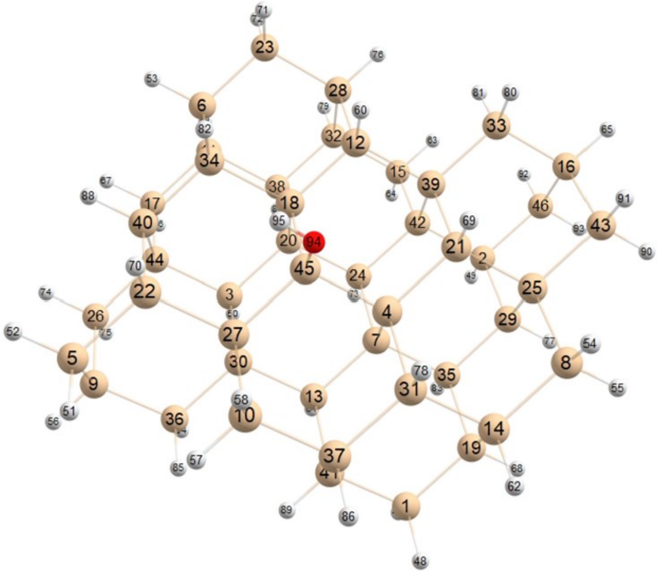

Si4: δ (^{29}Si)/ppm = -122.516
Si21: δ (^{29}Si)/ppm = -109.951
Si45: δ (^{29}Si)/ppm = -2.643

Figure A36. Si(111) model containing a $Si_3Si(OH)$.

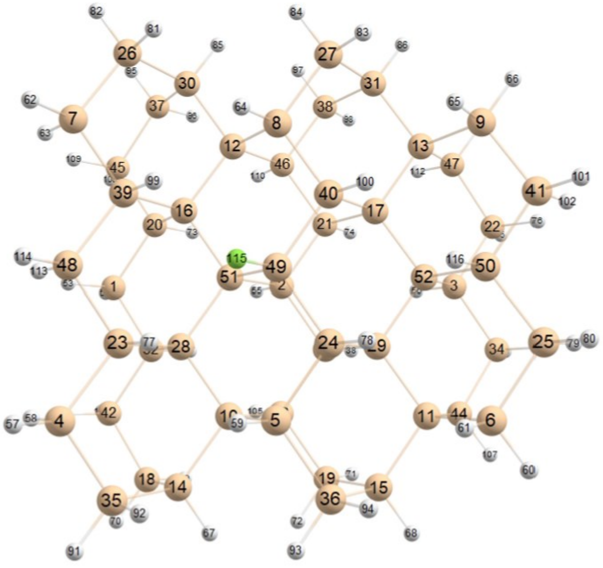

Si24: δ (^{29}Si)/ppm = -117.525
Si39: δ (^{29}Si)/ppm = -116.406
Si49: δ (^{29}Si)/ppm = 24.514
Si51: δ (^{29}Si)/ppm = -107.693
F115: δ (^{19}F)/ppm = -204.119

Figure A37. Si(110) model containing a Si_3SiF.

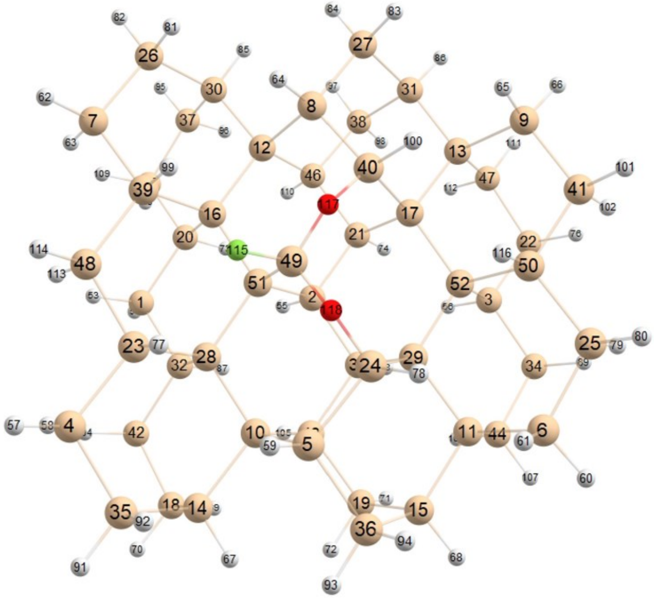

Si24: δ (^{29}Si)/ppm = -10.533
Si39: δ (^{29}Si)/ppm = -107.031
Si49: δ (^{29}Si)/ppm = -53.981
Si51: δ (^{29}Si)/ppm = -121.304
F115: δ (^{19}F)/ppm = -97.246

Figure A38. Si(110) model containing a SiO_2SiF.

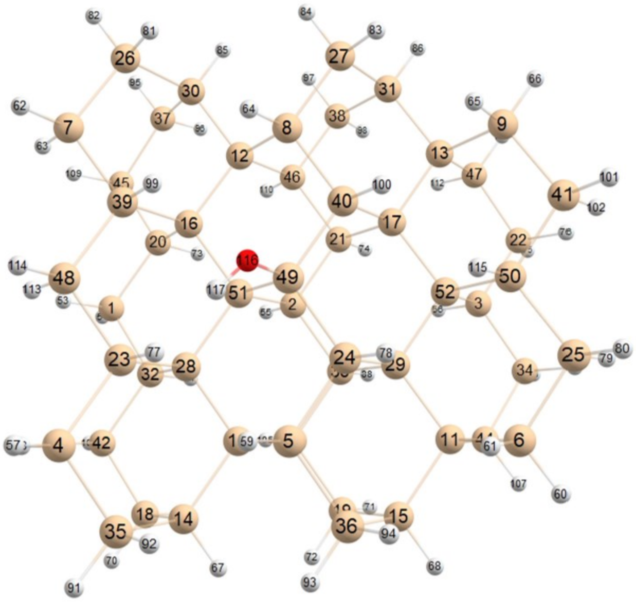

Si24: δ (^{29}Si)/ppm = -104.542
Si39: δ (^{29}Si)/ppm = -109.765
Si49: δ (^{29}Si)/ppm = -17.821
Si51: δ (^{29}Si)/ppm = -87.067

Figure A39. Si(110) model containing a Si$_3$Si(OH).

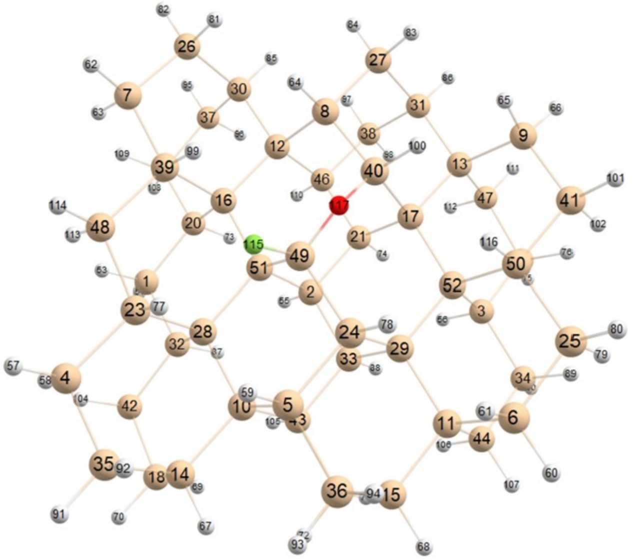

Si24: δ (^{29}Si)/ppm = -125.313
Si39: δ (^{29}Si)/ppm = -123.099
Si49: δ (^{29}Si)/ppm = 7.37
Si51: δ (^{29}Si)/ppm = -121.921
F115: δ (^{19}F)/ppm = -124.493

Figure A40. Si(110) model containing a Si$_2$OSiF.

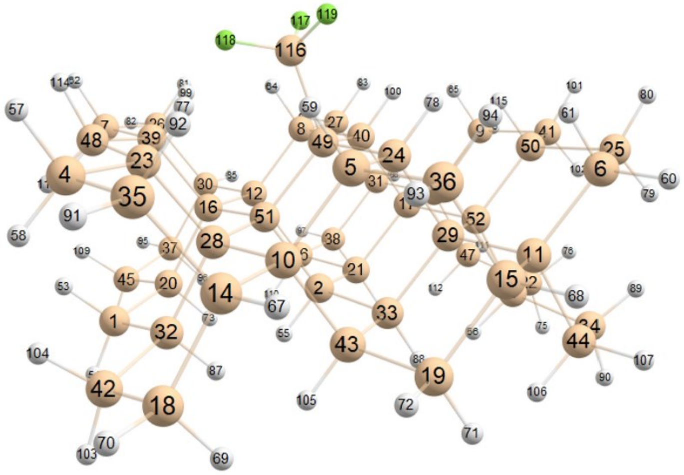

Si24: δ (^{29}Si)/ppm = -125.601
Si39: δ (^{29}Si)/ppm = -132.712
Si49: δ (^{29}Si)/ppm = -139.787
Si51: δ (^{29}Si)/ppm = -126.788
Si116: δ (^{29}Si)/ppm = -63.087
F117: δ (^{19}F)/ppm = -116.212

Figure A41. Si(110) model with an SiF_3 grafted on.

References

(1) Jameson, C. J.; Jameson, A. K.; Burrell, P. M. ^{19}F Nuclear Magnetic Shielding Scale from Gas Phase Studies. *J. Chem. Phys.* **1980**, *73* (12), 6013–6020.

(2) Hindermann, D. K.; Cornwell, C. D. Vibrational Corrections to the Nuclear-Magnetic Shielding and Spin-Rotation Constants for Hydrogen Fluoride. Shielding Scale for ^{19}F. *J. Chem. Phys.* **1968**, *48* (9), 4154–4161.

(3) Jameson, C. J.; Jameson, A. K. Absolute Shielding Scale For ^{29}Si. *Chem. Phys. Lett.* **1988**, *149*, 300–305.

(4) Anderson, S. L.; Luber, E. J.; Olsen, B. C.; Buriak, J. M. Substance over Subjectivity: Moving beyond the Histogram. *Chem. Mater.* **2016**, *28*, 5973– 5975.